Water solubility in diopside

Von der Fakultät für Biologie, Chemie and Geowissenschaften
der Universität Bayreuth

zur Erlangung der Würde eines
Doktors der Naturwissenschaften

- Dr. rer. nat. -

genehmigte Dissertation

vorgelegt von

Polina Gavrilenko

aus Petropawlowsk-Kamtschatsky (Russland)

Bayreuth, 2008

Vollständiger Abdruck der von der Fakultät für Chemie/Biologie/Geowissenschaften der Universität Bayreuth genehmigten Dissertation zur Erlangung des Grades eines Doktors der Naturwissenschaften (Dr. rer. nat.).

ACKNOWLEDGMENTS

TABLE OF CONTENTS

SUMMARY

(1) Water solubility in pure diopside

Water solubility in pure diopside was measured. Water-saturated diopside crystals were synthesized using piston-cylinder and multi-anvil presses at 20-30 and 100 kbar and 800-1100°C from an oxide and hydroxide starting mixture containing 10 % excess silica. The water concentration in diopside was determined from polarized infrared measurements on doubly polished single crystals. Water contents were calculated by integrating the absorption bands and using published extinction coefficients for water in diopside.

All measured infrared spectra of pure diopside fall into two groups. The first group of bands (Type I) occurs at higher wavenumber, at 3650 cm^{-1}, the second group (Type II) at lower wavenumber, at 3480-3280 cm^{-1}. The appearance of Type I or Type II spectra was neither correlated with pressure or temperature. The differences in the spectra point towards substitution mechanisms involving different vacancies, which in turn could be the result of different oxide activities in the starting material. Therefore, a separate series of experiments was carried out with starting materials with an excess or deficiency of MgO or SiO_2. These experiments yielded diopside with different absorption spectra. Starting materials with low silica activity yielded Type I bands, which are therefore likely to be related to Si vacancies. Type II bands form at high silica activity and may therefore be related to Mg or Ca vacancies. All spectra of both types show the same polarization behavior with the highest absorption in β direction, almost identical but slightly smaller absorption parallel to γ, and the lowest absorption along the α axis of the indicatrix.

Water solubility in pure diopside varies from 121 up to 568 ppm H_2O. Water solubility at 30 kbar increases from 700 to 1000°C and drops again above 1000°C. At 900°C, water solubility increases to a maximum at 25 kbar and then decreases rapidly to higher pressures. The water solubility in pure diopside may be described by the equation:

$$C_{H2O} = A f_{H2O} \ exp(-\Delta H^{1bar} / RT) \ exp(-P\Delta V^{solid} / RT)$$

with A = 0.0185 ppm/bar, f_{H2O} = water fugacity, ΔH^{1bar} = -11117 J/mol, R = gas constant, T = temperature in K, ΔV^{solid} = 14.62 cm^3/mol and P = pressure in bars.

Due to the low solubility of aluminum in clinopyroxene at high pressure, the data on pure diopside are probably a good guide for the water solubility in clinopyroxenes under the conditions of the deeper upper mantle. Since water solubility in diopside under those conditions is order of

magnitude below the water solubility in olivine, clinopyroxene is not expected to be a major storage site for water in the deeper upper mantle, even if its modal abundance is significant.

(2) Water solubility in aluminous diopside

Water-saturated Al-containing diopside was synthesized in an end-loaded piston-cylinder apparatus at 1.5-2.5 GPa and 900-1100$^{\mathrm{o}}$C. The compositions of the starting materials for Al-bearing diopside are along the join diopside ($CaMgSi_2O_6$) – Ca-Tschermak's component ($CaAl_2SiO_6$) with different ratios of these two end members. All infrared spectra of the Al-containing diopside show one main absorption band at 3650 cm^{-1}. This means that only one type of substitution mechanism takes place ($Al^{3+} + H^{+} = Si^{4+}$). All spectra show the same polarization behavior with the highest absorption in β direction, almost identical but slightly smaller absorption parallel to γ, and the lowest absorption along the α axis of the indicatrix ($A_\beta \geq A_\gamma > A_\alpha$). The water solubility strongly increases with the presence of Al up to 2500 ppm H_2O. The water solubility in aluminous diopside increasing with decreasing temperature. Estimated partition coefficients of water between clinopyroxene and orthopyroxene are close to unity, with $D_{cpx/opx}$ possibly increasing with temperature.

Together with previously published data on water in orthopyroxene, the results of this study clearly show that in the uppermost mantle, most of the water is dissolved in the pyroxenes. The relative importance of clinopyroxene and orthopyroxene is primarily a function of their modal abundance. This observation is consistent with the model of Mierdel et al (2007), which suggests that the Earth's asthenosphere is due to a minimum in water solubility in nominally anhydrous minerals.

During the subduction of oceanic lithosphere, clinopyroxene plays an important role in recycling water back into the mantle. Water in omphacite and garnet of eclogites causes the subduction of $4.67*10^{16}$ tones of water over one billion years, which equals 3.34 % of the total ocean mass. This may be converted to a reduction of sea level by ~130 m. Moreover, even higher recycling rates due to water in nominally anhydrous minerals may be obtained if the advective flow of mantle peridotite parallel to the subducting slab is considered. These data show that nominally anhydrous minerals are at least as important for recycling water into the mantle as serpentine. Models of the global water cycle that primarily rely on serpentine subduction therefore probably produce unrealistic results. The secular decrease of sea level since two billion years due to the cooling of the Earth, which favors serpentine subduction in such models is probably an artifact.

(3) Effect of water on the equation of state of diopside

In order to determine the effect of water on the equation of state of diopsides, high-pressure single crystal X-ray diffraction experiments with a diamond anvil cell were performed. The compressibility of diopside decreases with increasing water and Al content in the structure. The bulk modulus K_o and its first pressure derivative K' for the four diopside crystals are 106(1) GPa and 6.1(5) for pure anhydrous diopside (0 ppm H_2O); 107(1) GPa and 6.5(4) for pure diopside with 63 ppm of H_2O; 108(1) GPa and 6.3(4) for pure diopside with 600 ppm H_2O; and 113(1) GPa and 5.7(5) for Al-bearing hydrous (containing 0.374 Al a.p.f.u.) diopside with 2510 ppm H_2O. The compressibility anisotropy scheme for all four diopside crystals is $\beta_{oa} \approx \beta_{oc} < \beta_{ob}$, with the *b*-axis being most compressible for all four diopside crystals. The results on compressibility of diopside contrast with previous work, which showed that compressibility of most other main mantle phases increases with water content. This could be explained by different OH incorporation mechanisms. In olivine, there are protonated vacancies on the Mg position ($2H^+ = Mg^{2+}$), which make it more compressible, but in diopside Al cations and protons substitute for Si in the tetrahedral position ($Al^{3+} + H^+ = Si^{4+}$). This means that the dissolution of water in aluminous diopside actually does not create any vacancies, and accordingly, diopside gets harder in response to the coupled substitution of $Al^{3+} + H^+$ for Si^{4+}. In addition, from the refinement of the crystal structures of both hydrous and dry diopside and comparison with the structure of Ca-Tschermak's pyroxene it was possible to see the influence of protonation of the O2 and O3 oxygen atoms. This leads to a deviation from the linear correlation in bond distances in the *M1* and *T* polyhedra. Because of the contrasting effect of water on the equation of state of olivine and of pyroxenes in the upper mantle, detecting water from observations of seismic velocities alone is probably nearly impossible.

ZUSAMMENFASSUNG

(1) Löslichkeit von Wasser in reinem Diopsid

Die Löslichkeit von Wasser in reinem Diopsid wurde gemessen. Wasser-gesättigte Diopsid-Kristalle wurden in Piston-Cylinder- und Multi-Anvil-Pressen bei 20-30 und 100 kbar und 800-1100°C synthetisiert. Ausgangsmaterial war eine Oxid-Hydroxid-Mischung mit 10 % SiO_2-Überschuß. Wassergehalte wurden bestimmt aus polarisierten Infrarot-Messungen an doppelt-polierten Einkristallen. Hierzu wurden integrierte Bandenintensitäten bestimmt und publizierte Extinktionskoeffizienten für Wasser in Diopsid verwendet.

Zwei unterschiedliche Typen von Infrarotspektren von Diopsid wurden beobachtet. Typ I zeigt eine einzelne starke Bande bei at 3650 cm^{-1}. Typ II enthält mehrere Banden bei tieferen Wellenzahlen, bei 3480-3280 cm^{-1}. Das Auftreten der unterschiedlichen Typen von Spektren korreliert weder mit Druck noch mit Temperatur. Die unterschiedlichen Spektren deuten auf unterschiedliche Substitutionsmechanismen, an denen unterschiedliche Leerstellen beteiligt sind, die wiederum das Resultat unterschiedlicher Oxid-Aktivitäten sein könnten. Es wurde daher eine weitere Versuchsserie ausgeführt mit Ausgangsmaterialien, die entweder einen Überschuß oder ein Defizit von MgO oder SiO_2 enthielten. Ausgangsmaterialien mit niedriger SiO_2-Aktivität lieferten Diopsid-Kristalle mit Typ I-Banden, die daher wahrscheinlich mit Si-Leerstellen zusammenhängen. Typ II-Banden bilden sich bei hoher SiO_2-Aktivität. Die zugehörigen Protonen sind daher wahrscheinlich an Mg oder Ca-Leerstellen gebunden. Alle Spektren beider Typen zeigen ähnliches Polarisationsverhalten, mit der stärksten Absorption in β-Richtung, etwas geringerer Absorption parallel γ und der geringsten Absorption parallel der α-Achse der Indikatrix.

Die gemessene Wasserlöslichkeit in reinem Diopsid liegt zwischen 121 und 568 ppm H_2O. Bei 30 kbar steigt die Wasserlöslichkeit von 700 bis 1000°C und fällt dann oberhalb 1000°C etwas ab. Bei 900°C erreicht die Wasserlöslichkeit ein Maximum bei 25 kbar und fällt dann zu höheren Drücken hin schnell ab. Die Wasserlöslichkeit in reinem Diopsid kann beschrieben werden durch die folgende Gleichung:

$$C_{\text{H2O}} = A\, f_{\text{H2O}}\ exp(-\Delta H^{\text{1bar}} / RT)\ exp(-P\Delta V^{\text{solid}} / RT)$$

mit A = 0.0185 ppm/bar, f_{H2O} = Wasser-Fugazität, ΔH^{1bar} = -11117 J/mol, R = Gaskonstante, T = Temperatur in K, ΔV^{solid} = 14.62 cm^3/mol und P = Druck.

Aufgrund der geringen Löslichkeit von Aluminium in Klinopyroxen unter hohem Druck sind die Daten für reinen Diopsid wahrscheinlich ein gutes Modell für die Wasserlöslichkeit in Klinopyroxen im tieferen oberen Mantel. Die Wasserlöslichkeit in Diopsid liegt dort um Größenordnungen unter der Wasserlöslichkeit in Olivin. Klinopyroxen ist daher kein signifikanter Speicher für Wasser im tieferen oberen Mantel, selbst wenn seine modale Häufigkeit signifikant ist.

(2) Löslichkeit von Wasser in Aluminium-haltigem Diopsid

Al-haltiger Diopsid wurde unter Wasser-gesättigten Bedingungen in einer Piston-Cylinder-Apparatur bei 1.5-2.5 GPa und 900-1100°C synthetisiert. Die Zusammensetzung der Ausgangsmaterialien lag entlang der Verbindungslinie Diopside (CaMgSi$_2$O$_6$) – Ca-Tschermak's Komponente (CaAl$_2$SiO$_6$), mit unterschiedlichen Mengenverhältnissen. Alle Infrarotspektren von Al-haltigem Diopsid zeigen eine einzige Absorptionsbande bei 3650 cm^{-1}. Dies bedeutet, dass nur ein einziger Substitutionsmechanismus auftritt (Al^{3+} + H$^+$ = Si^{4+}). Alle Spektren zeigen prinzipiell die gleiche Polarisation, mit der stärksten Absorption in der β-Richtung, geringfügig schwächerer Absorption parallel γ, und der schwächsten Absorption parallel der α-Achse der Indikatrix (A$_\beta \geq$ A$_\gamma >$ A$_\alpha$). Die Wasserlöslichkeit steigt mit dem Gehalt an Aluminium bis auf 2500 ppm H$_2$O an. Die Wasserlöslichkeit steigt mit abfallender Temperatur. Geschätzte Verteilungskoeffizienten von Wasser zwischen Klinopyroxen und Orthopyroxen sind nahe 1, wobei D$_{cpx/opx}$ möglicherweise ansteigt mit der Temperatur.

Zusammen mit bereits bekannten Daten über Orthopyroxen zeigen diese Resultate, dass im obersten Mantel der größte Teil des Wassers in den Pyroxenen gelöst ist. Die relative Bedeutung von Orthopyroxen und Klinopyroxen als Wasserspeicher hängt hautsächlich von ihrer modalen Häufigkeit ab. Dies ist konsistent mit dem Modell von Mierdel et al (2007), wonach die Asthenosphäre der Erde verursacht wird durch ein Minimum in der Wasserlöslichkeit in nominal wasserfreien Mineralen.

Klinopyroxen spielt eine wichtige Rolle bei der Rückführung von Wasser in den Erdmantel durch Subduktion. Wasser in Omphacit und Granat kann während einer Milliarde Jahre 4.67*10^{16} Tonnen Wasser in den Mantel zurücktransportieren. Dies entspricht 3.34 % der gesamten Ozeanmasse oder einer Reduktion des Meeresspiegels um ~130 m. Noch weitaus höhere Transportgeschwindigkeiten durch nominal wasserfreie Minerale ergeben sich, wenn die Advektion von Mantelperidotit parallel zur subduzierten Platte berücksichtigt wird. Diese Daten zeigen, dass nominal wasserfreie Minerale mindestens ebenso wichtig sind für die Subduktion von

Wasser wie Serpentin. Modelle des globalen Wasserkreislaufs, die primär Transport durch Serpentin betrachten, liefern daher wahrscheinlich unrealistische Vorhersagen. Das säkulare Abfallen des Meeresspiegels in den letzten zwei Milliarden Jahren aufgrund der Abkühlung der Erde, die die Stabilität von Serpentin in Subduktionszonen begünstigt, entspricht wahrscheinlich nicht der Realität.

(3) Einfluß von Wasser auf die Zustandsgleichung von Diopsid

Um den Einfluß von Wasser auf die Zustandsgleichung von Diopsid zu bestimmen, wurden Einkristall-Röntgenbeugungsdaten unter hohem Druck in einer Diamantzelle gemessen. Die Kompressibilität von Diopsid nimmt mit zunehmendem Gehalt an Wasser und Aluminium ab. Der Kompressionsmodul K_o und seine erste Ableitung K' für die vier gemessenen Diopsidkristalle sind 106(1) GPa und 6.1(5) für reinen wasserfreien Diopsid (0 ppm H_2O); 107(1) GPa und 6.5(4) für reinen Diopsid mit 63 ppm H_2O; 108(1) GPa und 6.3(4) für reinen Diopsid mit 600 ppm H_2O; sowie 113(1) GPa und 5.7(5) für Al-haltigen (0.374 Al a.p.f.u.) Diopsid with 2510 ppm H_2O. Die Anisotropie der Kompressibilität ist ähnlich für alle vier Diopsid-Kristalle, $\beta_{ao} \approx \beta_{co} > \beta_{bo}$, wobei die b-Achse jeweils am stärksten kompressibel ist. Die Ergebnisse für Diopsid stehen im Gegensatz zu früheren Arbeiten, wonach die Kompressibilität der meisten anderen Mantelminerale mit dem Wassergehalt ansteigt. Dies beruht wahrscheinlich auf unterschiedlichen Lösungsmechanismen. In Olivin werden Mg-Leerstellen protoniert ($2H^+ = Mg^{2+}$), wodurch die Kompressibilität ansteigt, während in Diopsid Al^{3+} und ein Proton gemeinsam für Si^{4+} auf einem Tetraederplatz substituieren ($Al^{3+} + H^+ = Si^{4+}$). Dies bedeutet, dass der Einbau von Wasser in Al-haltigen Diopsid keine Leerstellen erzeugt; dementsprechend steigt die Festigkeit von Diopsid sogar aufgrund der gekoppelten Substitution von $Al^{3+} + H^+$ für Si^{4+}. Aus der Verfeinerung der Kristallstrukturen von wasserhaltigem und wasserfreiem Diopsid und Vergleich mit der Struktur des Ca-Tschermak-Endgliedes war es außerdem möglich, den Effekt der Protonierung der O2 and O3 Sauerstoff-Atome zu beobachten. Die Protonierung verursacht eine Abweichung von der linearen Korrelation der Bindungsabstände in den *M1* und *T*-Polyedern. Aufgrund des gegensätzlichen Effektes von Wasser auf die Zustandsgleichung von Olivin und Pyroxenen im oberen Mantel dürfte der Nachweis von Wasser aus Messungen seismischer Geschwindigkeiten allein unmöglich sein.

1. INTRODUCTION

1.1. Water in the mantle

Volatile components, such as H_2O, CO_2, Cl, F, S, played an important role in the formation of our planet. The origin of the water in our planet was debated for a long time. Drake (2005) described two end-members possibilities. The first one is that "wet" accretion took place with anhydrous and hydrous silicate phases among the material accreted to the growing planet. Another possibility is that temperatures were too high in the inner solar system for hydrous phases to exist in the accretion disk (Boss, 1998). Thus, an exogenous source of water may be needed, such as comets or asteroid material. Nutman (2006) proposed the existence of liquid water during the early history of the Earth and compiled evidence that oceans and continental crust already existed almost four billion years ago. Marty and Yokochi (2006) recently showed that the combined evidence from terrestrial hydrogen and nitrogen isotopic compositions strongly suggests that Earth´s volatiles came from a chondritic source. It therefore appears likely that most of the terrestrial water outgassed from Earth´s interior and that the contribution from comets to the bulk water budget is limited. There is increasing evidence that water is not only degassing from the mantle, today and in the geologic past, but that water is also currently recycled into the mantle, implying an internal water cycle of the Earth linking the oceans to the deep Earth´s interior (e.g. Rüpke et al., 2004; Bolfan-Casanova, 2005).

Water controls virtually all biological and geological processes on the Earth´s surface. Water also plays an important role in various processes in the mantle. The presence of water in mantle minerals, even at ppm level, strongly changes physical and chemical properties. These include transport properties such as electrical conductivity (Karato, 1990), diffusion, deformation mechanisms and viscosity (Chopra and Paterson, 1984; Karato et al., 1986) as well as seismic velocities (Karato and Jung, 1998). For example, experimental results by Hirth and Kohlstedt (1996) indicate that the viscosity of olivine aggregates is reduced by a factor of ~140 in the presence of water at a confining pressure of 300 MPa.

Water in the mantle may be present in different states. Water as a free fluid is certainly present in subduction zones and fluid inclusions may even be able to transport water deeper into the mantle (Peacock, 1990; Schmidt and Poli, 1998). Hydrous phases may be an important host of

water only in unusually cold or water-rich parts of the mantle (Rüpke et al., 2004). Most of the water probably occurs as hydroxyl point defects in nominally anhydrous phases (Bell and Rossman, 1992; Smyth et al. 1991).

Knowledge about water in the mantle comes both from field observations (or direct methods) and experimental data.

Analyses of nominally anhydrous minerals (NAMs) from mantle xenoliths show that they contain traces of water dissolved as hydroxyl point defects. Many studies of water in natural samples of NAMs (Bell and Rossman, 1992; Ingrin and Skogby, 2000) demonstrated that they could be the main reservoir of water in the mantle (Table 1.1-1).

Table 1.1-1. *Water content in nominally anhydrous minerals from mantle xenoliths*

Mineral	Water content (ppm H_2O by weigh)	References
Olivine	1-140 0-140 49-392 50 0-419 45-262	Bell, Rossman (1992) Ingrin, Skogby (2000) Koch-Müller et al. (2006) Mosenfelder et al. (2006) Matsyuk and Langer (2004) Bell et al. (2004)
Orthopyroxene	50-460 60-650 215-263	Bell, Rossman (1992) Ingrin, Skogby (2000) Bell et al. (2004)
Clinopyroxenes	150-1080 250-1840 100-1300 195-620 450-1650	Bell, Rossman (1992) Smyth et al. (1991) Ingrin, Skogby (2000) Bell et al. (2004) Katayama et al. (2006)
Garnet	4-200 200 15-74 2-163 50-150	Bell, Rossman (1992) Ingrin, Skogby (2000) Bell et al. (2004) Matsyuk et al. (1998) Katayama et al. (2006)

The water content measured on natural samples in the laboratory might be much lower than their original content in the mantle. A large part of the water in xenoliths could have been lost during ascent from the mantle. Mackwell and Kohlstedt (1990) measured H diffusivities in olivine high enough to allow H outgassing during ascent from the upper mantle. Therefore, it is important to analyze the diffusion kinetics of hydrogen in NAMs (Hercule and Ingrin, 1999; Carpenter Woods et al, 2000). The mechanisms and rates of diffusion are controlled by different types of defects associated with hydrogen incorporation in anhydrous minerals (Ingrin and Skogby, 2000). The dehydration rate of pyrope is around one order of magnitude lower (Wang et al., 1996;

Blanchard and Ingrin, 2004) than those observed for olivine (Mackwell and Kohlstedt, 1990) and diopside (Hercule and Ingrin, 1999). The rates of dehydration of diopside may be slower or comparable to those in olivine (Ingrin et al., 1995, Carpenter Woods et al., 2000). Therefore, the slower kinetics of hydrogen loss for pyroxenes and pyrope suggests that these minerals are more likely than olivine to preserve part of the water inherited from their upper-mantle source region. Based on experimental diffusion data for hydrogen, Demouchy et al. (2006) estimated the ascent rate of garnet-bearing lherzolite xenoliths at Pali-Aike, Chile to be in the order of 6 ± 3 m/s.

Experimental studies on water solubility in NAM's have been carried out under various conditions and for a range of bulk composition (Kohlstedt et al., 1996; Lu and Keppler, 1997; Rauch and Keppler, 2002; Bromiley and Keppler, 2004; and many others). These experiments can be done either by annealing of crystals or by crystallization of new phases during the experiment. However, such experiments do not show how much water is actually in the mantle. They only give an upper limit of the amount of water that could be stored in the mineral if the mantle were water-saturated.

The presence of water has an effect on the melting behavior of rocks. It lowers the solidus, increases the degree of partial melting and changes the composition of the melt produced (Green, 1973; Hirose and Kawamoto, 1995; Kushiro, 1972; Inoue, 1994). The water content of the mantle may therefore be inferred from analyses of the water content of mantle melts. The water content in the source region may be reconstructed if the partitioning of water between the melt and the source phases and the degree of melting is known.

Primitive melts trapped and isolated as melt inclusions have been used to infer the original water content in the source region. For example, Sobolev and Chaussidon (1996), based on analyses of water content of melt inclusions in olivine phenocrysts reported values for N-MORBs with an average value of ca. 1200 ppm H_2O. This yields values for the mantle source in the order of 130-240 ppm H_2O, for 10-20 % partial melting. Saal et al. (2002) analyzed olivine-hosted primary melt inclusions in submarine MORB from the Siqueiros transform fault (East Pasific Rise) which contain up to 1220 ppm H_2O which translates to ~142 ppm H_2O for the source of MORB.

Several geophysical observations can be used to detect hydrogen in the mantle:

- Hydrogen incorporation in mantle minerals changes the seismic wave velocities. The work by Jacobsen (2006) summarized the results of different authors on influence of water on bulk modulus of nominally anhydrous minerals. At ambient conditions, 0.2 wt% H_2O causes a measurable reduction of elastic moduli, on the order of 2 % (see Figure 1.1-

1). Karato (1995, 2006) suggested that the direct effect of water in reducing seismic wave velocities is important only for very high water contents of ~0.1-1 wt%. However, as suggested by Karato (1995), indirect effects such as the enhancement of anelasticity in seismic wave propagation or the effect of water on seismic anisotropy are likely to be significant. During convection in the upper mantle, deformation produces lattice-preferred orientation (LPO) of olivine. Because of the large elastic anisotropy of olivine crystals, the olivine LPO is responsible for seismic anisotropy in mantle rocks (Nicolas and Christensen, 1987; Mainprice and Silver, 1993). Karato (1995) suggested that hydrogen incorporation influences the LPO of olivine. The experimental work by Jung and Karato (2001) and Jung et al. (2006) showed that by adding a large amount of water in olivine, the relationship between flow geometry and seismic anisotropy changes. Those experimental data are consistent with, for example, investigations of natural olivine fabrics from the Higashi-akaishi peridotites from southwest Japan (Mizukami et al., 2004) as well as with olivine fabrics from the garnet peridotite at Cima di Gagnone, Central Alps (Frese et al., 2003). Moreover, there are a number of puzzling observations of seismic anisotropy in subduction zone regions, which could be attributed to the enrichment of water in these regions (Long and van der Hilst, 2005; Nakajima and Hasegawa, 2004; Smith et al., 2001).
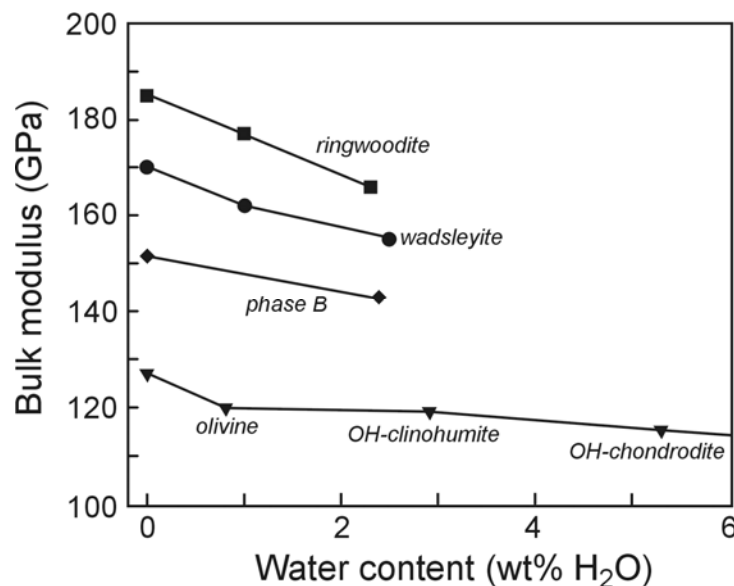
Figure 1.1-1. *Plot of bulk modulus against water content for various nominally anhydrous minerals (redrawn from Jacobsen, 2006)*

1. Introduction

- Water may change phase stabilities and therefore the location of seismic discontinuities in the mantle. For example, Wood (1995) suggested that the presence of water would expand the stability field of wadsleyite to lower pressure and enlarge the pressure range where olivine and wadsleyite coexist. He calculated that the presence of 500 ppm H_2O would broaden the binary loop from 7 km for dry system to at least 22 km. The observed sharpness of the 410-km discontinuity would therefore constrain the maximum H_2O content of the upper mantle olivine to about 200 ppm. Experimental work by Smyth and Frost (2002) showed both a decrease in the pressure of the olivine-to-wadsleyite transition in the presence of water and an increase in the width of the binary phase loop from 0.4 GPa (12 km) to 1.3 GPa (40 km), which would translate into much more water in upper mantle olivine than according to Wood's model. However, there may be other parameters that could affect the olivine-wadsleyite loop such as higher temperature or increasing the garnet content, which would sharpen the discontinuity, while adding H_2O would broaden the transition (Frost, 2003). Seismic observations by van der Meijde et al. (2003) provide evidence of a 20-35-km-thick discontinuity near 410 km under the Mediterranean, which they interpreted as being due to 700 ppm H_2O dissolved in olivine.

    Schmerr and Garnero (2007) recently interpreted seismic observations near the 410 and 670-km discontinuities beneath South America in a way that is very different from previous studies, including Wood (1995). They observed a deepening of the 410 km discontinuity, which they interpreted as boundary between hydrated and less hydrated wadsleyite. During hydration wet wadsleyite remains at the top of the transition zone, since it is chemically buoyant compared with anhydrous wadsleyite. The transition between those two wadsleyite phases may be responsible for the deep 410 km boundary.

- Changes in electrical conductivity of the mantle might point to the presence of water. Karato (1990) discussed possible changes in the electrical conductivity of olivine as a function of water content. The calculations suggested that the electrical conductivity of olivine increases significantly when hydrogen is present. The experimental results by Wang et al. (2006) showed indeed that the electrical conductivity is strongly dependent on water content and only slightly depends on temperature (Figure 1.1-2 A). The recent experimental study by Yoshino et al. (2006) also showed that the conductivity olivine increases with water. However, the electrical conductivity of hydrous olivine is anisotropic with the highest values along the [100] crystallographic axis. They also observed that the anisotropy in the electrical conductivity of olivine becomes smaller with

increasing temperature (Figure 1.1-2 B). Based on measurements of electrical conductivity Tarits et al. (2004) suggested 1000-1500 ppm H_2O dissolved in the olivine at 200-400 km depth beneath the French Alps. Yoshino et al. (2006) compared their experimental study with electromagnetic studies underneath the Pacific Ocean. They suggested that the high electrical conductivity obtained from some regions could not be explained by the hydration of olivine alone. The values for electrical conductivity near the East Pacific Rise would correspond to very high water contents in olivine, which would exceed the solubility limit. In addition, they pointed out that the weak anisotropy, observed in the East Pacific Rise, disagrees with the difference of the conductivity between ridge-parallel and ridge-normal directions.
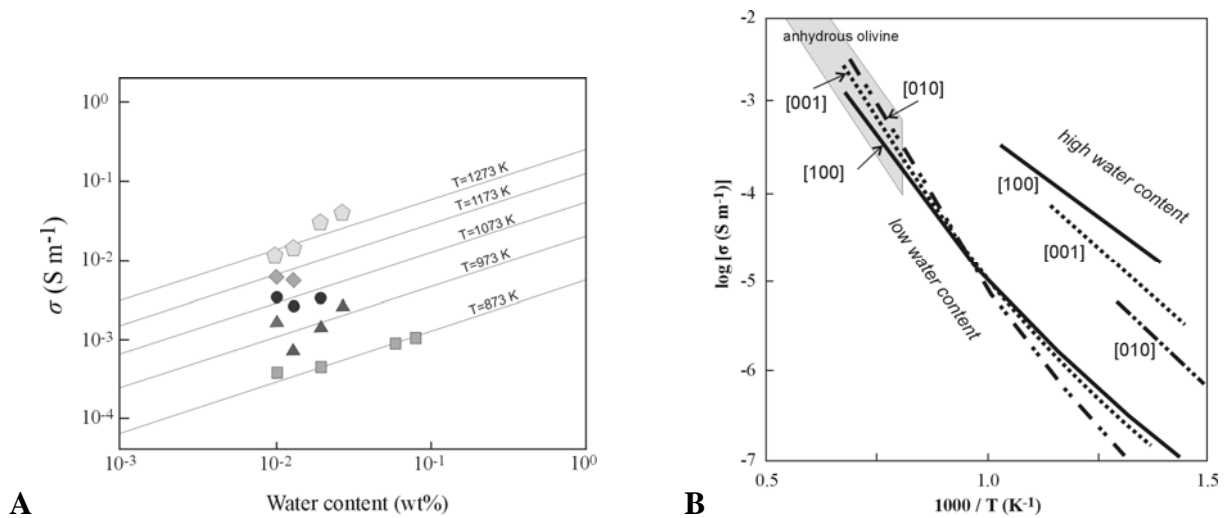
Figure 1.1-2. Experimental data on the influence of water on the electrical conductivity of olivine: A) by Wang et al. (2006). Electrical conductivity versus water content. Each symbol corresponds to the data for a given temperature (in K). The plot is redrawn from Wang et al., 2006; B) by Yoshino et al. (2006). Electrical conductivity of olivine as a function of reciprocal temperature. The plot is modified after Yoshino et al. (2006).
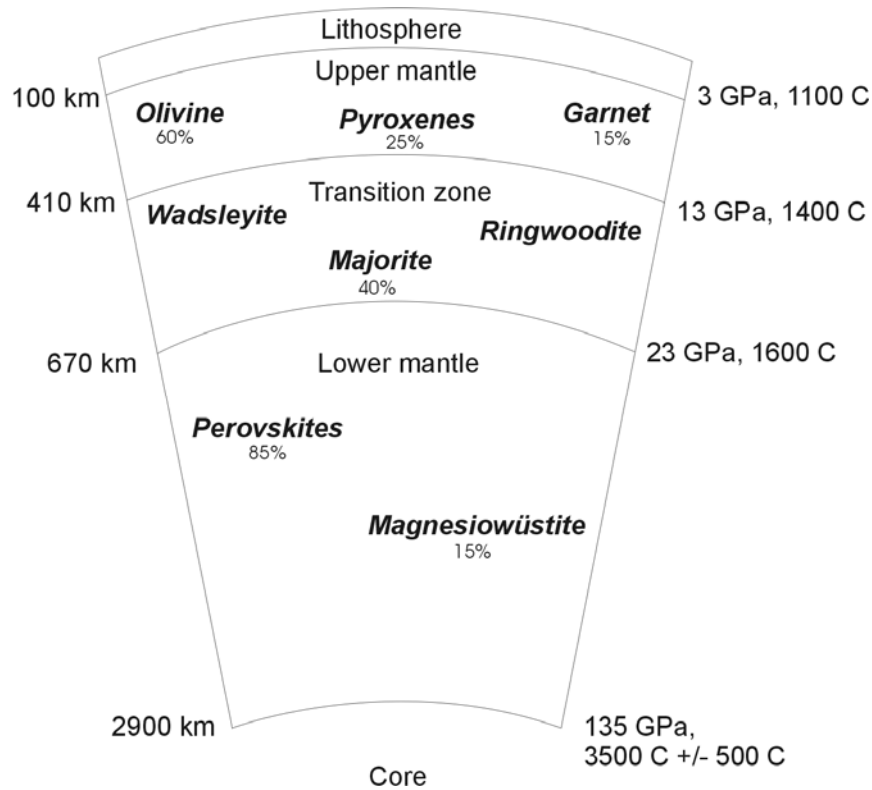
Figure 1.1-3. *Scheme of the Earth's mantle with the main mineral phases.*
Redrawn from Bolfan-Casanova (2000a)

The distribution of water in the mantle is affected by the different properties of the minerals stable in the upper mantle, transition zone and the lower mantle (Figure 1.1-3).

There is a large number of experimental studies on measuring water content and water solubility of the major minerals of the upper mantle. The water contents measured for natural olivine, the principal phase in the upper mantle, are quite low as compared to pyroxenes (Table 1.1-1). But the H_2O storage capacity of olivine increases greatly with H_2O fugacity and consequently with depth up to 1300 ppm at 410 km (Kohlstedt et al., 1996). The measurements by Mosenfelder et al. (2006) on Fe-bearing olivine, using a new infrared calibration, indicate a water solubility up to 5000 ppm H_2O. Orthopyroxenes (Rauch and Keppler, 2002; Mierdel and Keppler, 2004; Stalder and Skogby, 2002; Mierdel et al., 2007) and, possibly clinopyroxenes (Skogby, 1994; Bromiley and Keppler, 2004; Bromiley et al., 2004) are able to store much more water in their structure than olivine. Water solubility increases with aluminum incorporation in pyroxene (Rauch and Keppler, 2002; Mierdel et al., 2007). The water storage capacity of garnet is less

known than for other minerals. Lu and Keppler (1997) have shown the maximum solubility of water in pyrope to be 200 ppm. Natural garnets from mantle xenoliths show similar values (Bell and Rossman, 1992; Ingrin and Skogby, 2000).

The transition zone mostly consists of majoritic garnet, wadsleyite and ringwoodite. The two latter phases are β and γ high-pressure polymorphs of olivine $(Mg,Fe)_2SiO_4$, respectively. Those minerals may dissolve much more water then upper mantle phases. Smyth (1987) demonstrated that because of its structure, β-$(Mg,Fe)_2SiO_4$ might be a major host phase for water in the mantle. Experimental work by Young et al. (1993) reported up to 0.4 wt% of water in wadsleyite and Kohlstedt et al. (1996) reported that almost 3 wt% of water could be stored in the structures of wadsleyite and ringwoodite. According to the data on water solubility in $(Mg,Fe)_2SiO_4$ polymorphs, the largest part of water in the mantle is believed to be stored in the transition zone.

Water solubility in lower mantle minerals is less well known. Table 1.1-2 shows water contents in the principal lower mantle phases reported by Murakami et al. (2002) and by Bolfan-Casanova et al. (2000b, 2002, 2003). The high water contents in the samples of Murakami *at el*. (2002) could be caused by H_2O-rich fluid or melt inclusions or inclusions of hydrous minerals (superhydrous phase B), which were indeed observed by Bolfan-Casanova et al. (2003) in similar experiments. If the principal lower mantle minerals may dissolve only little water, the lower mantle may be essentially dry.

Table 1.1-2. Experimentally observed water contents in main phases of the lower mantle

Mg-perovskite	Ca-perovskite	Mg-wüstite	References
62 ppm H_2O			Meade et al. (1994)
1900-2400 ppm H_2O	3700-3800 ppm H_2O	1900 ppm H_2O	Murakami et al. (2002)
below detection limit			Bolfan-Casanova et al. (2000b)
		20 ppm H_2O	Bolfan-Casanova et al. (2002)
2 ppm H_2O		20-75 ppm H_2O	Bolfan-Casanova et al. (2003)

1.2. The global water cycle

During subduction of the oceanic lithosphere significant volumes of water may be recycled back into the Earth's deep interior. At the same time, magmatic degassing at middle oceanic ridges and on ocean islands transports water from the mantle to the surface. These plate tectonics processes may therefore contribute to fluctuations in global sea level.

1.2.1. The subduction zone water cycle

Recycling of oceanic crust, lithosphere and sediments into the mantle by plate tectonic processes could potentially transport large volumes of water back into the mantle.

The oceanic crust is hydrated by different processes. During deposition, sediments become saturated by pore water and they also contain structurally bound water in clay minerals and other phases. Plank and Langmuir (1998) estimate the average water content of oceanic sediments to be 7.29 wt.% H_2O. The water content of oceanic crust below the sediment layer is enhanced through high- and low-temperature hydrothermal processes. The average water content in the upper layer of the oceanic crust is 1.3-2.8 wt.% H_2O and in the deep oceanic crust is 1.5-0.2 wt.% H_2O, depending on the age and the degree of alteration of the crust (Wallmann, 2001; Ito et al., 1983).

The degree of hydration of the lithospheric mantle below the oceans is less constrained. During subduction the oceanic lithosphere bends and generates faults. These faults provide possible fluid pathways for deep water transport. The seawater may infiltrate through the faults, reaching the lithospheric mantle and reacting with it to produce serpentine, which was proposed to be a significant host of water (Ranero et al., 2003; Schmidt and Poli, 1998). However, there are no reliable estimates of the degree of mantle serpentinization in subducted lithosphere and there is no evidence that serpentinized mantle occurs everywhere in subduction zones, although reduced seismic P velocities possibly indicative of serpentinization have been observed at some localities (Berhorst et al., 2003; Sallares and Ranero, 2003).

Ito et al. (1983) assumed that ca. 8.8 x 10^{14}g of water/per year can be subducted into the mantle through altered crust. But not all subducted water reaches the mantle. The oceanic crust together with overlying sediments loose water during continuous dehydration processes, changing the water content in the slab with depth.
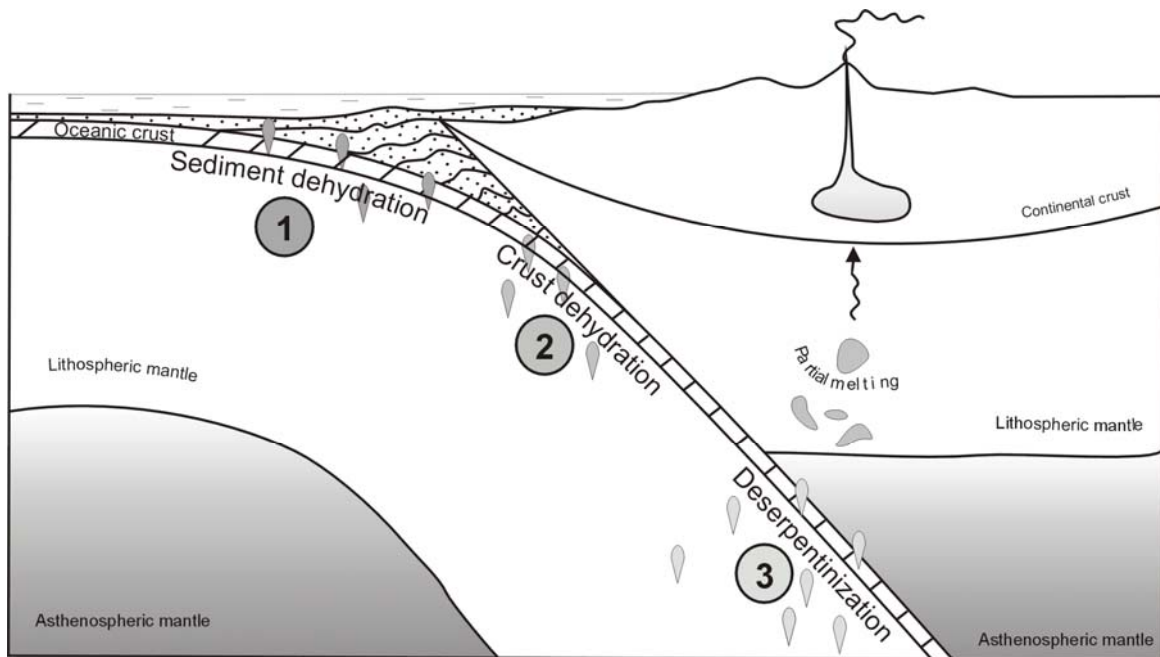
Figure 1.2-1. *Schematic drawing of subduction zone water cycle*
(modified after Rüpke et al., 2004)

The dehydration of the subducting slab may proceed in several stages. For example, Rüpke et al. (2004) described this process as (see Figure1.2-1): (1) water release from sediments at shallow levels (< 20 km) with expulsion of large volumes of fluid waters; (2) water release from sediments and oceanic crust (20-100 km), when most of the hydrous phases become unstable; (3) deep fluid release (> 100 km) from oceanic crust and deserpentinizing mantle.

First, sediments dehydrate at shallow depth. According to the model by Rüpke et al. (2004), at ~50 km depth the sediments have already dewatered by over 50 % and by ~100 km they contain only 25 % of their initial water. Ito et al. (1983) described the process of dewatering of sediments as follows: first, water is expelled from sediments at a depth of ~18 km. This water percolates along the faults and fractures and returns to the surface. Clay minerals carry water down to 20-50 km depth, and finally at a depth of 30-70 km water is expelled from some metamorphosed sediments.

Dehydration in deep subducting lithosphere is controlled by complex reactions involving a variety of hydrous phases. The hydrous phases involved can be divided into three major groups based on their stability range (see Kawamoto, 2006): (1) low-pressure hydrous minerals such as chlorite, talk and amphibole; (2) high-pressure hydrous phases such as DHMS (dense hydrous magnesium silicates), K-richterite and phase A; (3) middle-pressure hydrous minerals such as

phlogopite, antigorite, Mg-sursassite and 10Å phase. Dehydration of hydrous phases occurs continuously during subduction and the degree of the dehydration depends on their stability at the elevated P-T conditions in the subduction slab. For example, the stability of Mg-sursassite overlaps the stabilities of hydrous phases such as chlorite towards lower pressures and phase A at higher pressures (Bromiley and Pawley, 2002). A similar stability field was reported by Fumagalli et al. (2001) for the 10Å phase. Therefore, the group (3) of hydrous minerals may be important for delivering water from low-pressure hydrous minerals to high-pressure hydrous minerals.

The thermal structure of a subduction zone depends on many parameters including the thermal structure of the incoming lithosphere, convergence rate, the geometry of subduction, radioactive heating, induced convection in the overlying mantle wedge, and the amount of shear heating along the subduction shear zone (Peacock, 1996). These parameters affect the amount of water that can be transferred into the deeper parts of the mantle (Rüpke et al., 2004). Rüpke et al. (2004) modeled the water release during subduction. Their model very much emphasizes the importance of serpentine for transporting water deep into the mantle. The older and colder slab, the more water can be retained in the serpentinized mantle at the same depth (Figure 1.2-2).
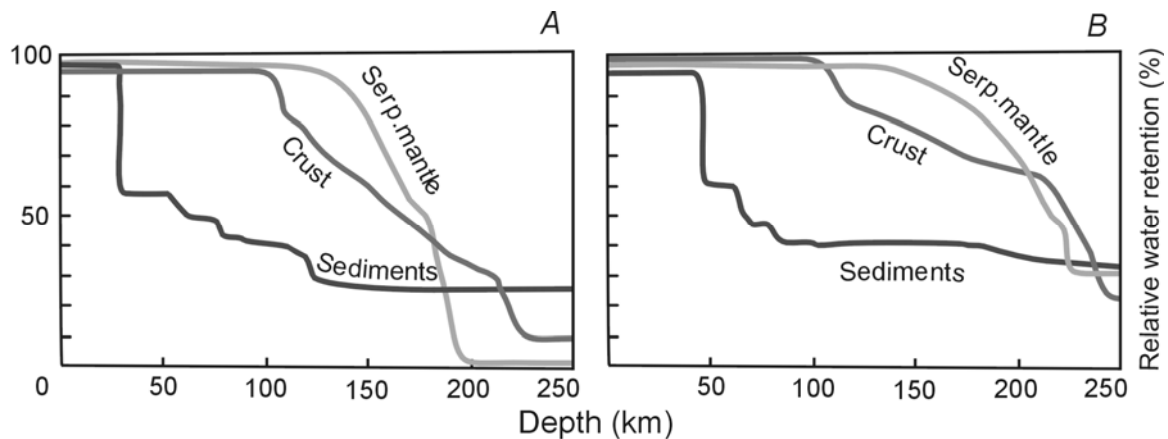
Figure 1.2-2. *Modeled water release during subduction (redrawn from Rüpke et al., 2004), showing the relative degrees of water retention at 8 GPa for the three different lithologies. A – for 40-Ma-old slab; B – for 120-Ma-old slab.*

It is somewhat uncertain, however, whether this model really properly describes the recycling of water into the mantle. First, it is uncertain whether serpentine really occurs in significant proportions in the lithospheric mantle in all subducted slabs. Second, even if serpentine is present, it will decompose completely before reaching the stability field of other hydrous phases, unless the subducted plate follows a very cold trajectory. This implies that for earlier Earth history, where geothermal gradients may have been higher, the model by Rüpke et al. (2004) would predict no recycling of water into the mantle.

There are two important effects that are not considered in the model described above: (1) After all dehydration reactions, trace amounts of water can still be present within NAMs, such as olivine, garnet and pyroxenes and therefore water can be transported deeper into the upper mantle and transition zone. (Bell and Rossman, 1992; Smyth et al., 1991; Ingrin and Skogby, 2000; Katayama et al., 2006; etc.). (2) Even if water is released from the subducting slab, it will percolate in the overlying mantle wedge, where it may be dissolved in minerals such as olivine. Advective flow of mantle material parallel to the subducting slab may then also transport a significant part of this water into the mantle.

The transfer of H_2O from the mantle to the surface reservoir is assumed to occur by magmatic activities at the oceanic ridges (1.1 x 10^{14}g of water / year), hotspots (0.13 x 10^{14}g of water / year) and volcanic arcs (1.0 x 10^{14}g of water / year) (Ito et al., 1983).

1.2.2. Global sea level variations

Eustatic sea-level change is a vertical movement of the sea surface relative to the centre of the Earth (Reading and Levell, 1996). It reflects variation in the volume of ocean water or the ocean basin. In contrast, vertical movement of the sea surface relative to a moving reference point (oceanic crust or overlying sediments) is called relative sea-level change. The processes that affect water volume may be distinguished by rate and amplitude (Figure 1.2-3). High rate and low amplitude processes are desiccation, thermal expansion and variations in groundwater and lake storage. Water volume changes are dominated by growth and decay of continental ice sheets, which produce high-amplitude, rapid eustatic changes. Changes in ocean basin volume are dominated by slow variations in sea-floor spreading rates or ocean ridge lengths or sedimentation (Miller et al., 2005).
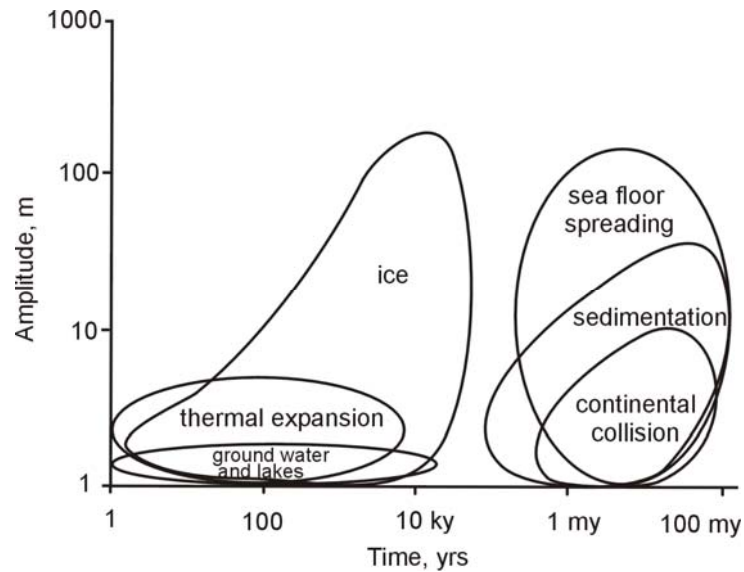
Figure 1.2-3. *Timing and amplitudes of geologic mechanisms of eustatic change (redrawn from Miller et al., 2005)*

Recognition of sea level changes in the rock record is commonly based on the preserved three-dimensional stacking patterns of transgressive, regressive, lowstand and highstand depositional sequences (Eriksson, 1999). Newell (1967) and Hallam and Wignall (1999) suggested that eustatic sea-level changes may be associated with the big five mass extinctions (at the end of Ordovician, Permian, Triassic and Cretaceous and in the late Devonian) and several lesser extinction events.

Recent eustatic variations can be estimated from satellite measurements, tide gauges, shoreline markers, reefs and atolls, oxygen isotopes and the flooding history of continental margins and cratons (Miller et al., 2005).

The determination of past variations in spreading has been viewed as an alternative method to estimate global eustatic sea level variations. For example, as it was shown by Hays and Pitman (1973), that the Cretaceous transgression occurred at approximately the same time as an increase in the spreading rate of oceanic plates. Increased rates of plate spreading increase the volume of oceanic ridges and, therefore, decrease the volume of ocean basins. This type of lithospheric model does not consider subduction of oceanic lithosphere. Therefore, Gurnis (1990) showed that changes in plate velocity lead to changes in the rate of subduction of lithosphere into the mantle and that this process leads to sea level fluctuations fundamentally different from the single lithospheric model.

Previous models usually assumed that slow eustatic sea level changes result from changes in the volume of the ocean basins, while the total amount of water on Earth's surface remained unchanged. Only in recent years, the possibility of changes in the amount of water on Earth's surface by exchange with the reservoir in the Earth's mantle is seriously being considered.

Rüpke et al. (2004) estimated that the global sea level might have dropped by several hundred meters due to subduction of water since the Cambrian. Their estimates are based on the assumption of widespread serpentinization of the suboceanic mantle, which is described above in section 1.2.1. According to their model since ~2-2.5 Ga the water recycling may be dominated by serpentinized mantle even assuming a small amount of serpentinization. However, nominally anhydrous minerals may play an important role in transporting water into the mantle which may also influence sea level. From experimental results on water solubility in pyrope Lu and Keppler (1997) pointed out that a significant fraction of total water in the hydrosphere has been recycled into the mantle since the Proterozoic.

1.3. Water in clinopyroxenes

1.3.1. Crystal chemistry of clinopyroxenes

Pyroxenes are chain silicates that belong to either the orthorhombic or the monoclinic crystal system. Monoclinic pyroxenes are called clinopyroxenes. Their space groups are $C2/c$, $P2_1/c$ and $P2/n$, depending on their crystal composition and genetic history. The crystal structure of clinopyroxene is shown in Figure 3.1-1. It consists of corner-shared tetrahedral and edge-shared octahedral chains elongated along the crystallographic c-axis. The octahedral chains connect with tetrahedral chains by sharing corners. The general chemical formula for all pyroxenes is $M2\,M1\,T_2\,O_6$. $M2$ is the distorted 6- to 8-coordinated site, $M1$ – the octahedral site and T is the tetrahedral site (Morimoto, 1988). The following elements may occupy the various sites:

T *Σ=2.00* Si^{4+} Al^{3+} Fe^{3+}

                    ↓   ↓

M1 *Σ=1.00* Al^{3+} Fe^{3+} Cr^{3+} Ti^{4+} V^{3+} Ti^{3+} Zr^{4+} Sc^{3+} Zn^{2+} Mg^{2+} Fe^{2+} Mn^{2+}

                                                                          ↓   ↓   ↓

M2 *Σ=1.00* Mg^{2+} Fe^{2+} Mn^{2+} Li^+ Ca^{2+} Na^+
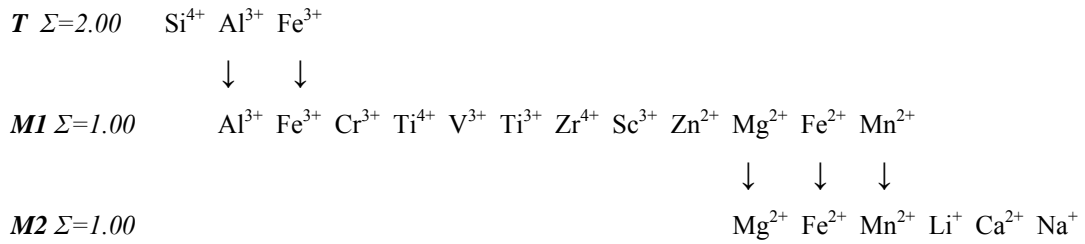
Omphacite can be considered as a solid solution between the jadeite (Jd) $NaAlSi_2O_6$ and diopside (Di) $CaMgSi_2O_6$ end members. Natural omphacites usually have more complex compositions and can involve such end-members as hedenbergite (Hd) $CaFe^{2+}Si_2O_6$, aegirine (Ae) $NaFe^{3+}Si_2O_6$, Ca-Tschermak's component (CaTs) $CaAlAlSiO_6$, and Ca-Eskola component (Ca-Es) $Ca_{0.5}\square_{0.5}AlSi_2O_6$.
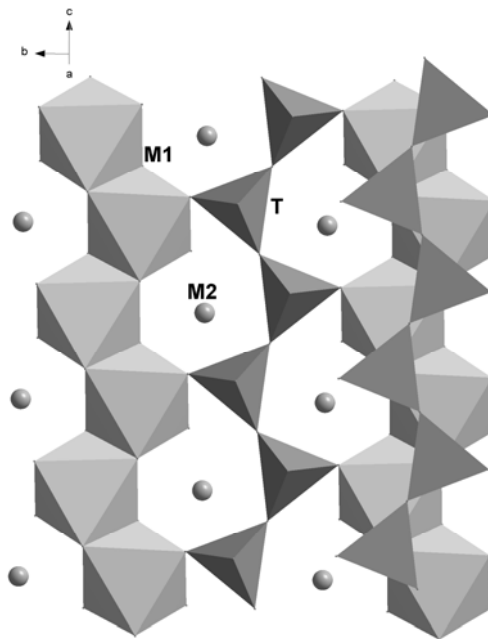
Figure 1.3-1. *Clinopyroxene crystal structure with C2/c space group*
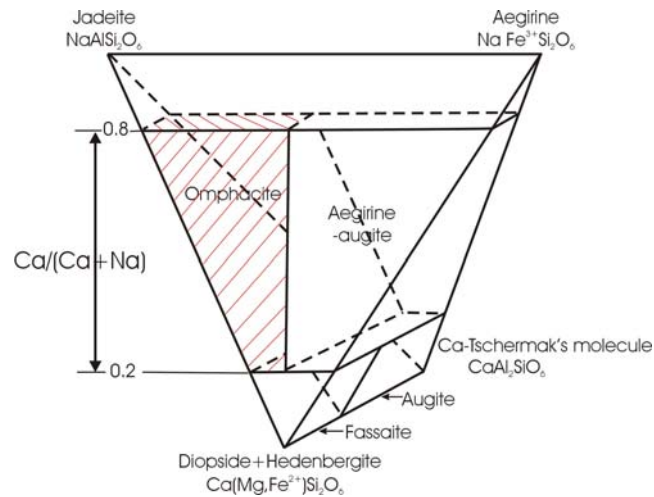
Figure 1.3-2. *Nomenclature of clinopyroxenes in the system NaAlSi$_2$O$_6$ (Jd) – NaFe^{3+}Si$_2$O$_6$ (Ae) – CaMgSi$_2$O$_6$ (Di) – CaFeSi$_2$O$_6$ (Hd) – CaAl$_2$SiO$_6$ (CaTs) showing the compositional fields of omphacite, aegirine-augite, fassaite and augite (redrawn after Clark and Papike, 1968)*

Clark and Papike (1968) defined omphacites compositionally within the system Di-Hd-Jd-Ac-CaTs as being confined between the boundary planes $0.2 \leq$ Na / (Na+Ca) ≤ 0.8, and a limited to the ratio $[Al]^6$ / $([Al]^6 + Fe^{3+}) \geq 0.5$ (Figure 1.3-2). The end-members display *C*2/*c* space group, whereas natural omphacitic pyroxenes in eclogitic assemblages, with a composition close to the binary jadeite-diopside join, display a transformation from *C*2/*c* to *P*2/*n* at intermediate compositions, related to coupled Ca/Na and Al/Mg cation ordering.

1.3.2. Composition of mantle clinopyroxenes

In general, the compositions of mantle clinopyroxenes are different depending on their paragenesis. For example, Smulikowski (1968) gives the maximum, minimum and average weight percent of main oxides in omphacitic pyroxenes from garnet peridotites, common eclogites and ophiolitic eclogites. The differences between the groups are quite noticeable, in particular with respect to Na$_2$O, Al$_2$O$_3$ and MgO.

Peridotite is the dominant rock of the upper mantle. It is an ultramafic rock made of Mg-rich olivine and lesser amounts of pyroxene, usually both Ca-Mg-rich clinopyroxene and Ca-poor, Mg-

rich orthopyroxene. Depending on pressure, peridotite also contains some amount of plagioclase, spinel or garnet (Best, 2003). Mantle peridotite is sampled by xenoliths (rock inclusions) hosted in alkaline basaltic and kimberlitic rock (Nixon, 1987). These xenoliths are classified according to their clinopyroxene in two types: Cr-rich diopside-type or Al-Fe-Ti-rich clinopyroxene-type. The Cr-diopside peridotite is the most common mantle-derived xenoliths. Depending on the proportions of olivine and both pyroxenes, the peridotite may be classified as lherzolite and harzburgite. The clinopyroxene is essentially diopside ($CaMgSi_2O_6$) that contains only a small weight percentage of alumina, Fe-oxide and few tenths of weight percent of Cr_2O_3 which gives an emerald-green color (Best, 2003; Smulikowski, 1968).

Together with pyrope-rich garnet, omphacite is the main constituent of eclogites. Eclogite is roughly the chemical equivalent of basalt, but it recrystallized under high pressures, so its mineralogy is different from that of basalt. Kyanite may also occur in eclogites with compositions relatively rich in Ca and Na. Primary accessory phases in mantle eclogites include coesite, corundum, sanidine, rutile, phlogopite, amphibole, graphite and diamond (Ragland, 1989; Hall, 1996). There are many data related to the pressure and temperature conditions of eclogite formation in the literature. Figure 1.3-3 demonstrates the most common and quite wide range of eclogite P-T conditions. The conditions were calculated by Peacock (2000) for the Japanese subduction region.
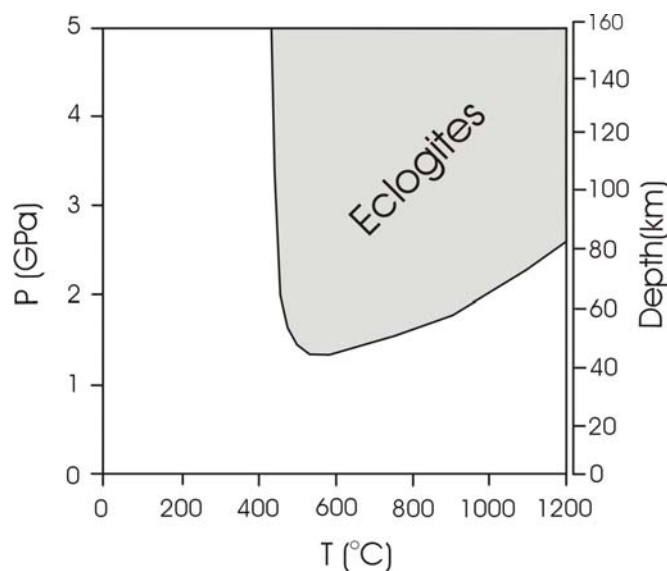
Figure 1.3-3. *P-T conditions for eclogite formation given by Peacock (2000)*

for the Japanese subduction zone

a)

b)

c)

d)
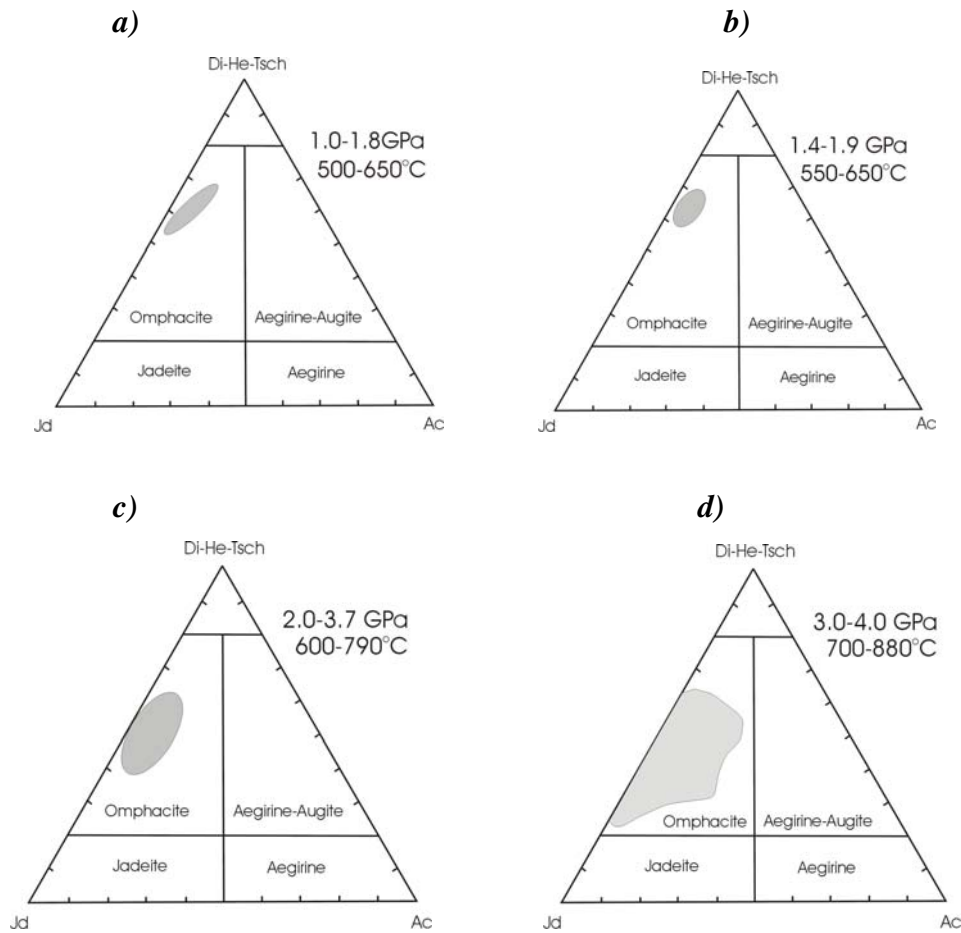
Figure 1.3-4. *Chemical composition of some eclogitic omphacites from different occurrences:*

   a)   *Eclogites of Hong'an, Eastern China (Eide and Liou, 2000);*

   b)   *NE Sardinia, Italy (Giacomoni et al., 2005);*

   c)   *Dora-Maira Massif, Western Alps (Nowlan et al., 2000);*

   d)   *Donghai, Eastern China (Zhang et al., 2000).*

Generally, jadeitic pyroxenes form in high-pressure environments and are characteristic of the blueschist or eclogitic facies. The clinopyroxenes in the eclogite rocks in general range in composition from about $Jd_5Di_{80}Hd_{15}$ to $Jd_{70}Di_{25}Hd_5$ (Smyth, 1980). Aegirin and Ca-Tschermak's components can also be present in eclogitic omphacites (e.g., Smulikowski, 1968). Figure 1.3-4 demonstrates examples of eclogitic omphacite compositions from different regions. There is some systematic dependence of composition on P-T conditions in some locations. In general, the jadeite component appears to increase with pressure.

Smyth (1980) reported that most of the analyses of eclogitic omphacites show a significant excess of octahedrally-coordinated Al over tetrahedrally-coordinated Al. There is enough silica in most of samples to fill the tetrahedral site, so that there is relatively little Al^{IV} and the excess of Al cannot be ascribed to Ca-Tschermak's molecule. This is consistent with diagrams by White (1964) in which the percentage of jadeite component is plotted against the percentage of Tschermak's component (Figure 1.3-5). There is a clear distinction between eclogites and granulite facies pyroxenes. Some of the omphacites are not always soda-rich as often alleged, but they are also low in Tschermak's molecule. The theoretical basis for this separation into two well-defined groups is that amount of aluminum in four-fold coordination is expected to increase with temperature whilst that in six-fold coordination increases with pressure. So in the eclogite facies pyroxenes, Al is concentrated in the sites with six-fold coordination whereas in granulites facies pyroxenes Al is approximately equally partitioned between sites with both six- and four-fold coordination.
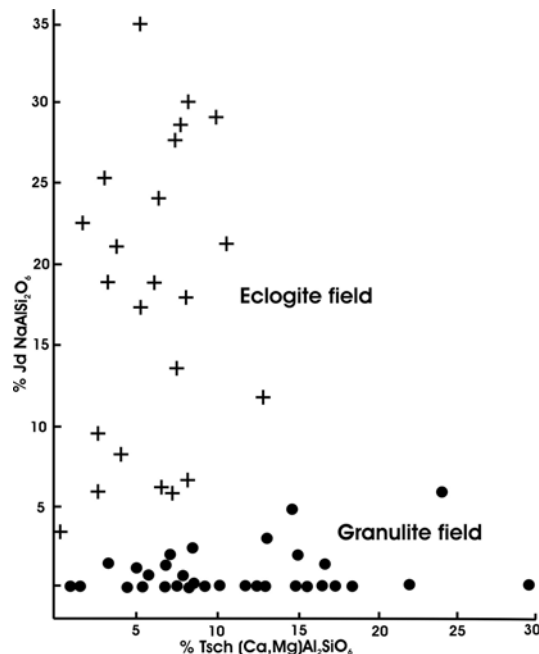
Figure 1.3-5. *Plot of mol. percent jadeite against Tschermak's molecule showing the clear separation of eclogitic and granulitic clinopyroxenes (redrawn after White, 1964)*

1.3.3. Water solubility in clinopyroxenes

Natural mantle clinopyroxenes, particularly from eclogites show the highest concentration of hydroxyl in their structure among other nominally anhydrous minerals. From experimental studies (e.g., Skogby, 1994; Bromiley and Keppler, 2004) and from studies of natural samples (Bell and Rossman, 1992; Smyth et al., 1991; Skogby et al., 1990) it is known that clinopyroxenes are able to store up to two thousand ppm of H_2O (Table 1.3-1). Bromiley and Keppler (2004) suggested that, the most important factor controlling water solubility even more important than temperature and pressure is the bulk chemistry of omphacite. This is consistent with the relatively low water solubility (59-557 ppm at 2 GPa and 1100-1330°C) found by Stalder and Ludwig (2007) for pure diopside.

Table 1.3-1. *Water content in some clinopyroxenes from eclogites of mantle xenoliths*

Location	Water content, ppm H_2O	References
Rietfontien, South Africa	1080	Bell and Rossman (1992)
Robert Victor, South Africa	1200	Smyth et al. (1991)
Bobbejaan mine	1840	Smyth et al. (1991)
Dan-Carl mine	1055	Smyth et al. (1991)
Mexico and Simcoe, USA	140-528	Peslier et al. (2002)

There are several possibilities for hydroxyl to enter the pyroxene structure. In pure diopside ($CaMgSi_2O_6$) there may be a Si vacancy in tetrahedral position, $4H^+ = Si^{4+}$ (hydrogarnet defect), or a Mg vacancy in the octahedra, $2H^+ = Mg^{2+}$. Another possibility is a coupled substitution of hydrogen together with some other cation in order to achieve charge balance. For example, as it was shown by Rauch and Keppler (2002) for orthopyroxene, Al plus hydrogen may substitute Si in a tetrahedral position ($Al^{3+} + H^+ = Si^{4+}$) or in an octahedral site ($Al^{3+} + H^+ = 2Mg^{2+}$). It is also possible that there are several substitution mechanisms operating at the same time.

The main components in omphacite that are expected to influence water solubility are jadeite, Ca-Escola component and Ca-Tschermak's component. The low cation content in some natural samples may be related to hydrogen incorporation in omphacite. An increase in the vacancy

concentration is expected to lead to an increase in the capacity of omphacite to incorporate water during subduction (Smyth, 1980). Cation deficiency correlates with the appearance of oriented needles of quartz in omphacite under ultra high-pressure conditions (Krogh Rayna and Paquin, 2003). This may be due to the exsolution of a former non-stoichiometric omphacite through the reaction: CaEs = CaTs + 3Qtz (Smyth, 1980). Smyth et al. (1991) found that samples with high Ca-Eskola components contain the highest OH concentrations observed in pyroxenes. Moreover, the experimental study of Bromiley and Keppler (2004) demonstrated that small amounts of the Ca-Eskola component considerably increase the amount of OH incorporation in synthetic jadeite. Gatzemeier and Wright (2006) calculated that for pure diopside and jadeite anhydrous phases, the *M2* cation (Ca in diopside and Na in jadeite) vacancy is predicted to be most favourable. On the other hand, for both pure phases the most energetically favourable means of hydrogen incorporation will be via the formation of the hydrogarnet defect ($Si^{4+} = 4H^+$). The water solubility in clinopyroxenes may increase with increasing Al content in tetrahedral coordination. The computer modeling by Gatzemeier and Wright (2006) confirmed that this kind of substitution facilitates hydrogen incorporation in diopside. The solubility and incorporation mechanisms of water in synthetic jadeite were investigated by Bromiley and Keppler (2004). They also established the importance of cation vacancies on the *M2* site in providing mechanisms for hydrogen incorporation. Besides, their results also suggested that substitution of lower valency cations onto *M1* site may also be important.

Since hydroxyl in clinopyroxene can be incorporated at different point defects in the crystal structure, it results in several absorption bands in the infrared range between 3200 and 3700 cm^{-1}. In natural clinopyroxene samples the absorption bands usually occur at around 3355, 3460, 3535 and 3640 cm^{-1} (Smyth et al., 1991; Skogby et al., 1990; Ingrin et al., 1989). Smyth et al. (1991) found that the intensity of the band near 3460 cm^{-1} correlates with the amount of Ca-Eskola component. Therefore, this band was assigned to vacancies in the *M2* site, which was confirmed by experimental work on synthetic diopside (Stalder and Ludwig, 2007). Natural omphacites, investigated by Koch-Müller et al. (2004), exhibited three groups of absorption bands at 3445-3465, 3500-3540 and 3600-3624 cm^{-1}. Koch-Müller et al. (2004) assigned the first group to cation vacancies in *M2* position and the second group to Al^{3+} substituting Si in the tetrahedral site and the third group had an uncertain origin. Stalder and Ludwig (2007) established that synthetic pure diopside shows one OH-absorption band at 3357 cm^{-1} which can be related to Mg-vacancies, whereas additional absorption bands appear for Al-, Fe- and Cr-doped diopsides at 3462, 3443 and 3432 cm^{-1} respectively. The absorption bands in the 3600 cm^{-1} range were proposed to be assigned to Si-vacancies or other tetrahedral defects. Therefore, they concluded that their FTIR spectra may

detect the silica activity under which the pyroxenes crystallized. Moreover, the absence of high wavenumber absorption bands at ~3600 cm^{-1} may be diagnostic for a high silica activity and the absence of Si-vacancies in the clinopyroxene structure. All these observations suggested that the individual absorption bands represent defects of different cationic environment in the pyroxene structure.

Skogby et al. (1990) and Bromiley et al. (2004) analyzed polarized spectra from natural diopside which yielded the OH location and orientation within the crystal structure. They concluded that the OH dipole that causes the bands at ~3600 cm^{-1} in diopside substitutes for the O2 oxygen and points directly toward an O3 oxygen, although Bromiley et al. (2004) proposed a second possible mechanism: incorporation of hydrogen onto the O2 site with vibration of the OH dipole towards the O1 or O2 site. The O2 position is the most favourable for OH substitution, since it is highly underbonded (Cameron and Papike, 1980). If Al substitutes for Si, it will increase the underbonded character of the O2 even further, making OH substitution at the O2 site more favourable (Skogby et al., 1990). According to Skogby et al. (1990), the hydroxyl groups that cause the OH-stretching bands at lower wavenumber are also caused by substitution for O2, but they point in another direction. This conclusion is in contrast to Smyth et al. (1991) who suggested that both high and low wavenumber absorption bands correspond to hydroxyl dipoles pointing in the same direction. The computer modeling results from Gatzemeier and Wright (2006) also suggested that the defect associated with the substitution $Al^{3+} + H^+ = Si^{4+}$ in the tetrahedral site belongs to the O2 oxygen atom. They showed that oxygen vacancies would preferentially form on O2 sites in diopside and on O3 sites in jadeite and these defects would be charge balanced by *M2* rather than *M1* vacancies.

Despite all of this previous work, a systematic study of water solubility in clinopyroxenes over a wide range of pressure, temperature and Al-content is still missing.

1.3.4. Effect of water on the equation of state of clinopyroxene

The presence of hydroxyl in major mantle minerals causes defects in their structures and hence can significantly change compressibility and seismic wave velocities. To detect water in the mantle from seismic observations we need to know the effect of water on the elastic moduli of major mantle minerals.

Several studies have been carried out (Nestola et al., 2006a; Nestola et al., 2006b; Nestola et al., 2008; etc.) on the crystal chemistry, high-temperature and high-pressure behavior of clinopyroxenes with different chemical composition. These works established some correlations between substitutions in pyroxenes and their equations of state. For example, Nestola et al. (2006a) studied the high-pressure crystal structure along the jadeite $NaAlSi_2O_6$ – aegirine $NaFeSi_2O_6$ solid solution. They observed that the bulk modulus K_o decreases from 134 GPa for pure jadeite to 116 GPa for pure aegirine. However, little is know about the effect of water on the elastic properties of pyroxenes. Despite extensive work on the incorporation of water in orthopyroxenes (Rauch and Keppler, 2002; Mierdel and Keppler, 2004; etc.), no studies on the elastic properties of OH-bearing orthopyroxenes are available. For clinopyroxenes, McCormic et al. (1989) measured the compressibility of two omphacites with the same jadeite content $Jd_{58}Di_{42}$, but with different concentrations of vacancies, attributed to Ca-Eskola component ($Ca_{0.5}\square_{0.5}AlSi_2O_6$). The vacancy-poor omphacite is significantly less compressible than the vacancy-bearing pyroxene. Jacobsen (2006) suggested that although the samples were not analyzed for water, it is possible that the vacancy-rich omphacite from the study of McCormic et al. (1989) contained significant amounts of water as $HAlSi_2O_6$, which is similar to the Ca-Eskola component, $Ca_{0.5}\square_{0.5}AlSi_2O_6$.

1.4. Aims of the thesis

The aim of this thesis is to study the role of clinopyroxenes in water storage and water transport in Earth's mantle. Here, the following key questions shall be answered:

1) What is the contribution of clinopyroxene to water storage in the upper mantle?

2) What is the role of clinopyroxenes in recycling water from oceans back into the mantle?

3) Can water in the upper mantle be detected by seismic observations?

To determine the amount of water that may be stored in clinopyroxenes in the upper mantle or in a subducting slab, two series of experiments were carried out:

a) Determination of water solubility in pure diopside. These experiments are particularly useful to establish structural and thermodynamic models of water solubility, because in such a compositionally simple system, the assignment of infrared bands to certain defects and a thermodynamic analysis of the data is relatively easy.

b) Determination of the influence of the Al content on water solubility in diopside.

In order to address the possibility of detecting water by seismic observations, the effect of water on the elastic properties of clinopyroxenes was studied by high-pressure diffraction experiments. An addition, in order to understand better the mechanism of hydroxyl incorporation into the diopside the structural refinements of hydrous and anhydrous diopside have been performed.

2. EXPERIMENTAL TECHNIQUES

2.1. High-pressure experiments for measuring water solubility in diopside

2.1.1. Starting materials

Starting material for the synthesis of pure diopside was a mixture of high-purity of $Mg(OH)_2$, $Ca(OH)_2$ and SiO_2 with excess water. The mixture was nearly stoichiometric according to the following reaction with 10 wt.% excess of silica:

$$Ca(OH)_2+Mg(OH)_2+2SiO_2 = CaMgSi_2O_6+2H_2O$$

To determine the influence of activities of different components in the system during crystallization, a separate series of experiments was carried out. The starting materials for these of experiments were prepared with an excess or a deficiency of $Mg(OH)_2$, $Ca(OH)_2$ or SiO_2 (Table 2.1-1).

Table 2.1-1. *Mixtures for the synthesis of diopside*

Diopside (Di)	Deficiency of oxide / hydroxide	Excess of oxide / hydroxide
$Ca(OH)_2+Mg(OH)_2+2SiO_2 = CaMgSi_2O_6+2H_2O$	5 wt.% $Ca(OH)_2$ 5 wt.% $Mg(OH)_2$ 5 wt.% SiO_2	15 wt.% $Ca(OH)_2$ 15 wt.% $Mg(OH)_2$ 30 wt.% SiO_2

The starting material for the synthesis of aluminous clinopyroxenes were mixtures of high-purity $Mg(OH)_2$, $Ca(OH)_2$, $Al(OH)_3$ and SiO_2 with excess water. The composition of the starting materials lies along the join diopside ($CaMgSi_2O_6$) – Ca-Tschermak's component ($CaAl_2SiO_6$) with different ratios of these two end members (Table 2.1-2).

Table 2.1-2*. Mixtures for the synthesis of diopside – Ca-Tschermak's component solid solution*

Components	Diopside (Di)	Ca-Tschermak's component (CaTs)
Reactions	$Ca(OH)_2+Mg(OH)_2+2SiO_2 = CaMgSi_2O_6+2H_2O$	$Ca(OH)_2+2Al(OH)_3+SiO_2 = CaAl_2SiO_6+4H_2O$
Mixtures	Di90-CaTs10 Di85-CaTs15 Di80-CaTs20 Di75-CaTs25 Di70-CaTs30	

The starting mixtures were ground under ethanol for ca. 1 hour and subsequently dried in an oven at 150 ^{o}C.

2.1.2. Sample and capsule preparation

For piston-cylinder experiments, 120-140 mg of the starting mixtures were sealed together with 30-35 mg of distilled water into platinum-rhodium capsule ($Pt_{95}Rh_5$) by arc welding. The capsules were made from $Pt_{95}Rh_5$ tube with 5 mm outer diameter and 4.6 mm inner diameter. The bottom was closed by a lid made from $Pt_{95}Rh_5$. To prevent water evaporation during welding the capsule was cooled by liquid nitrogen. In addition, the top part of the capsule was machined down to 0.2 mm wall thickness and closed with a lid made of pure Pt of 0.2 mm thickness to facilitate welding (Figure 2.1-1).
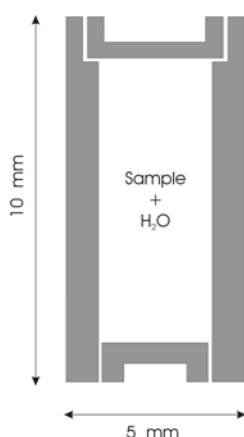
Figure 2.1-1*. Schematic drawing of PtRh capsule used for piston-cylinder experiments*

For multi-anvil experiments, the capsules were made from $Pt_{95}Rh_5$ tube with 2 mm outer diameter and 1.6 mm inner diameter. 12-13 mg of the starting mixture were sealed together with 2.5-3.5 mg of distilled water into the capsule which was closed by bending the edges and welding. Capsules were cooled by liquid nitrogen during welding to prevent water loss. The capsule dimension for multi-anvil pressure cells was 2 mm in diameter and up to 3.5 mm in length.

A major experimental problem is the synthesis of clear, inclusion-free single crystals large enough to be polished and oriented for measuring by infrared spectroscopy. Therefore, to get large, good-quality crystals, a chemically layered starting material sometimes was used, as it is shown on Figure 2.1-2. It helps to increase crystal size by reducing nucleation rates. However, this method has the disadvantage that not all activities are completely controlled during crystal growth anymore.
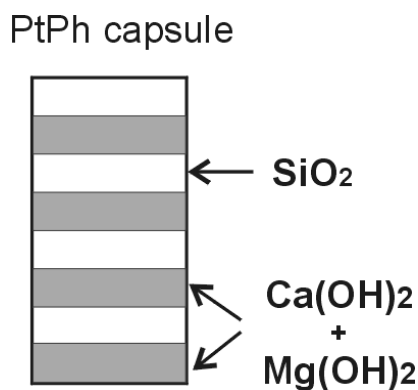
PtPh capsule

Figure 2.1-2. Scheme of PtRh capsule with a layered starting material for piston-cylinder experiments

2.1.3. High-pressure apparatus

The experiments at high pressure and high temperature for measuring water solubility in diopside were performed in a piston-cylinder or multi-anvil apparatus.

2.1.3.1. Piston-Cylinder press

The majority of experiments were carried out with an end-loaded piston-cylinder apparatus. The apparatus consist of a tungsten carbide pressure vessel supported by a steel ring (bomb) (Boyd

and England, 1960). The pressure vessel is end-loaded during a run with a thrust delivered by a hydraulic press (see Figure 2.1-3). The pressure is applied to the sample via pressure amplification from a small force on a large piston to a large force on a small piston, driven by a second hydraulic press. The load is transferred from ram to the tungsten carbide piston which is pushed into the bomb applying pressure to the sample.
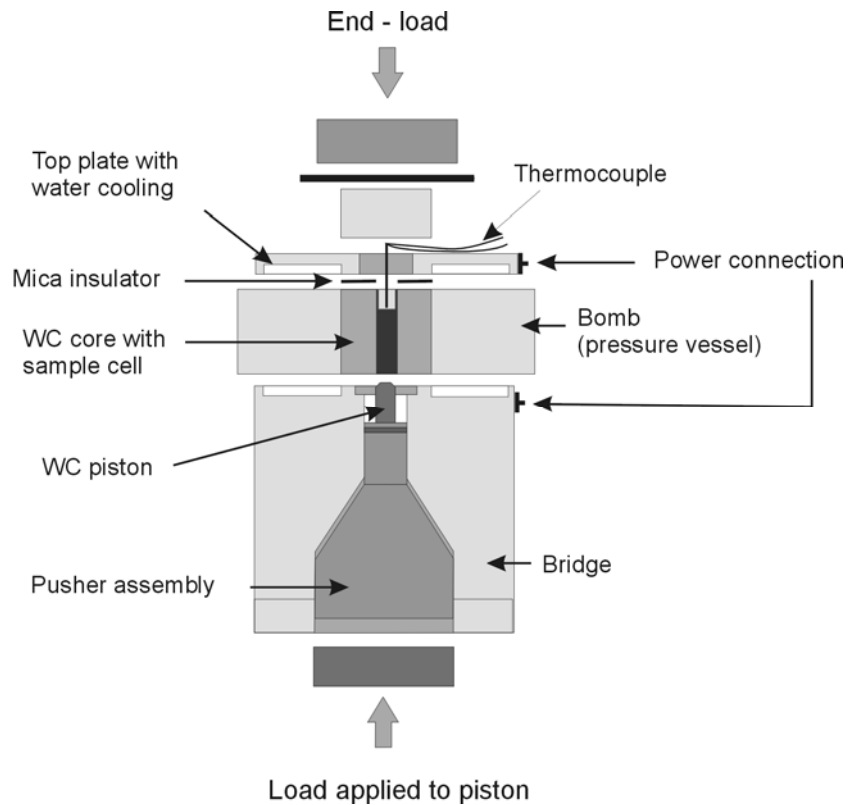
Figure 2.1-3. Schematic drawing of end-loaded piston-cylinder apparatus. Redrawn from Mierdel (2006).

The experiments were carried out using pressure assemblies made of talc as pressure transmitting medium, graphite as resistance furnace, Pyrex glass as electrical insulator, and crushable alumina (Figure 2.1-4). The graphite furnace was tapered to minimize temperature gradients along the length of the capsule. To reduce water loss from the capsule during experiments pyrophyllite sleeves were used around the capsule (Bromiley et al., 2004). For the

synthesis of pure diopside, the capsule sleeves were made from MgO to avoid alumina contamination in the sample.

Temperature was controlled using a Pt_{100} - $Pt_{90}Rh_{10}$ thermocouple (type S) (wire Ø=0.25 mm) within a 2-hole Al_2O_3 sleeve. In this study, the samples were first pressurized up to 90 % of the desired pressure, and then they were heated to the final temperature at 100^oC per min. Once the temperature was stable, the pressure was increased to the final pressure. The pressure was controlled automatically by a hydraulic pump. The duration of each run was 2.5-3 days.

The experiments were quenched isobarically by shutting off the power. A quench from 1000^oC to room temperature takes approximately 15 seconds.
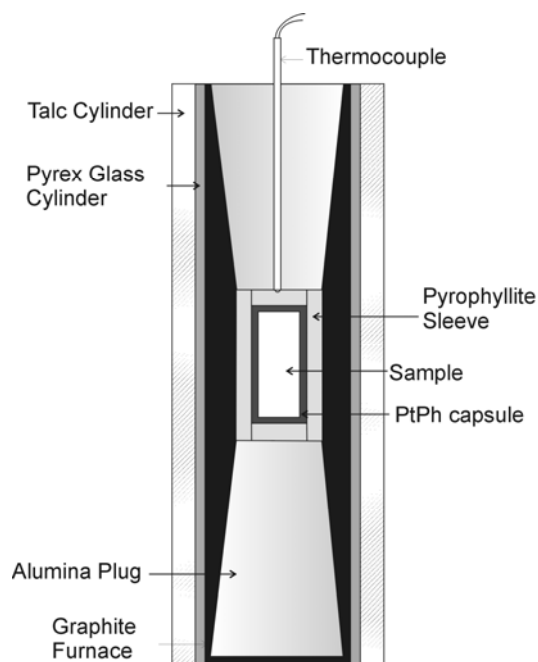
Figure 2.1-4. *Details of the 1/2 inch assembly for piston-cylinder experiments*

2.1.3.2. Multi-Anvil press

In order to study the pressure and temperature dependence of water solubility in diopside, a series of multi-anvil experiments was performed. All experiments were done using a 6-8 Kawai-type multi-anvil press (Kawai and Endo, 1970) at Bayerisches Geoinstitut (BGI). The details of the multi-anvil technique and experimental procedure are given by Rubie (1999). Schematically, the details of the multi-anvil apparatus are shown in Figure 2.1-5.
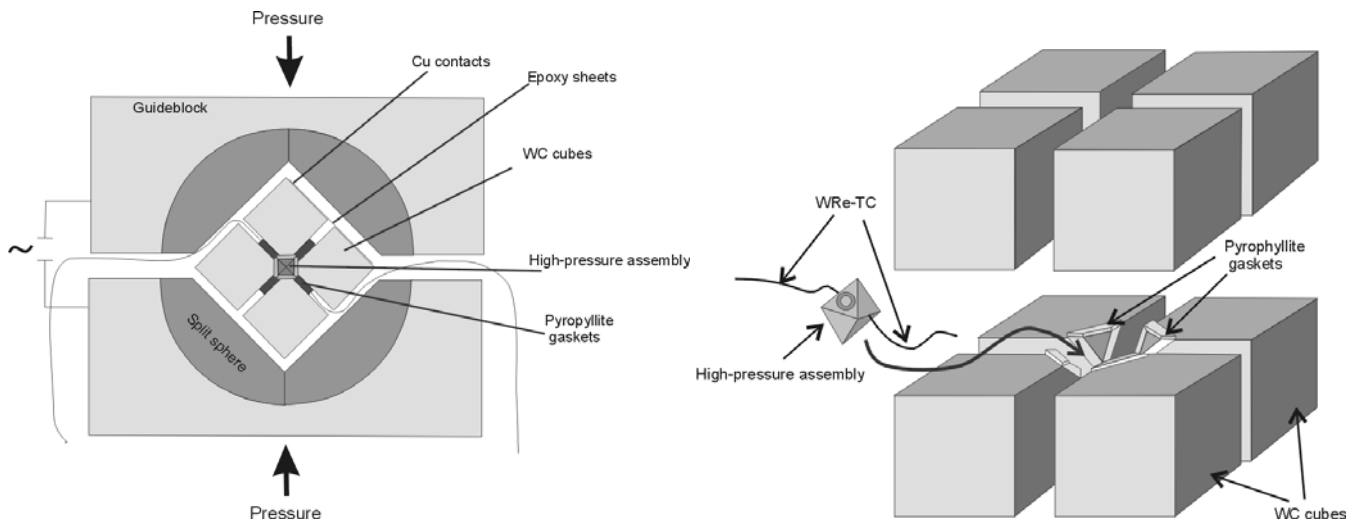
Figure 2.1-5. *Details of multi-anvil apparatus. Left: two guide blocks enclosing six anvils forming a cubic cavity. Right: eight tungsten-carbide anvils with octahedral cavity formed by their truncated corners. Redrawn from Stoyanov (2006).*
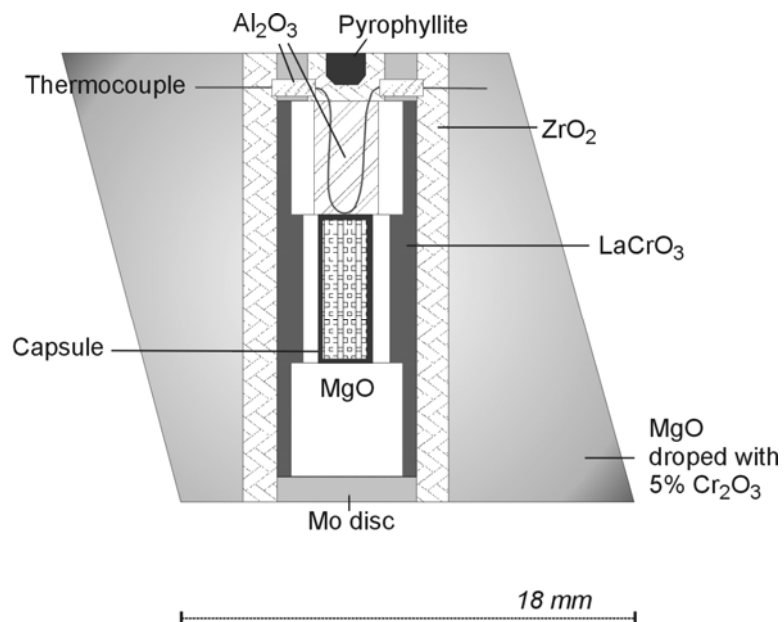
Figure 2.1-6. *Details of the 18/11 multi-anvil pressure assembly. Modified after Rubie (1999).*

The 18/11 (octahedral edge length / tungsten-carbide anvil truncation in mm) pressure cell was used in the 1200 tonne press in combination with 32-mm tungsten-carbide anvils. The pressure cells contain stepped cylindrical $LaCrO_3$ heaters (Figure 2.1-6). In this type of furnace, the wall thickness of the central part is thicker than the two end sections. This shape insures relatively low resistance in the central part of the heater. This minimizes the thermal gradient along the sample. A cylindrical zirconia sleeve surrounding the heater provides thermal insulation (Rubie, 1999). A MgO sleeve insulates the capsule from the heater to avoid chromium contamination from the furnace. The capsule was placed inside an octahedron of MgO doped with 5% Cr_2O_3 to reduce heat loss by radiation. The W_3Re_{97}-$W_{25}Re_{75}$ thermocouple (wire Ø=0.25 mm) within a 4-hole Al_2O_3 sleeve was positioned at the top of the capsule and separated from it by a Re disc. For all multi-anvil experiments in this study, the samples first were fully pressurized and then slowly heated at ca. 100^oC per min. At the end of the run the experiments were quenched isobarically by shutting off the power.

The octahedral sample assembly was compressed by a set of eight corner-truncated tungsten-carbide cubes (first stage anvils). Pyrophyllite gaskets were used between the cubes. The cubes were packed all together using epoxy-impregnated fiberglass laminate sheets which also insure electrical insulation towards the guided six anvils. This set of cubes is then compressed by the six outer tool-steel anvils (second stage), which are driven by a hydraulic press in an uniaxial direction (see Figure 2.1-5).

In such a two-stage Kawai-type multi-anvil configuration, one of the difficulties is to correctly measure the pressure on the sample. This can be achieved through calibrations. At room temperature, pressure may be calibrated by measuring *in situ* the variation of the electrical resistance of a standard material during a phase transformation. At high temperatures, the pressure is affected by a number of factors. One of them is that an increase in temperature results in a thermal expansion of the cell and increases the pressure. In addition, the gasket begins to flow, resulting in a decrease of pressure. In this case, pressure may be calibrated for a range of temperatures using known equilibria such us quartz-coesite (Bohlen and Boettcher, 1982), coesite-stishovite (Zhang et al., 1996), olivine-wadsleyite (Morishima et al., 1994), wadsleyite-ringwoodite (Suzuki et al., 2000). The calibration for the 18/11 assembly was based on the calibration curve developed by Frost et al. (2004).

2.1.4. Analytical techniques for the investigation of run products

After each experiment, the capsules from both piston-cylinder and multi-anvil experiments were first checked for the presence of excess water. For that purpose, the capsule was weighed, then perforated and placed in an oven for a couple of hours. After heating, the capsule was weighed again and the water content was determined by the weight difference. In some cases the water was coming out immediately after perforating in the capsule. This indicates water saturation in the system during crystallization. The capsules were opened by cutting the bottom.

2.1.4.1 Chemical analysis

The chemical composition of crystalline run products was measured with a JEOL JXA-8200 electron microprobe (EMPA) at the Bayerisches Geoinstitut (BGI). Accelerating voltage in all cases was 15kV and the beam current was 15nA. The concentrations of Ca, Mg, Si (with diopside standard) and Al (spinel standard) were determined and the oxygen concentration was calculated by difference. The electron beam size was focused and about 1-2 μm in diameter. Peak counting times were always 20 s. For each sample ca. 50-100 points were collected.

2.1.4.2. Infrared spectroscopy

In a Fourier-transform infrared spectrometer a beam of polychromatic infrared light is emitted from an IR source, and it is modulated in intensity by an interferometer. The light passing through the sample is partly absorbed by interaction with characteristic vibrations of the material and finally is detected by an IR detector (Libowitzky and Beran, 2004).

The stretching vibration of hydroxyl groups is typically in the frequency range of about 3000-3600 cm^{-1} (Figure 2.1-7). Only proton-bearing species absorb infrared radiation in this range, which makes infrared spectroscopy a very sensitive method for the determination of hydroxyl. Hydroxyl groups may absorb infrared radiation only if a component of the electrical field vector of the incident wave is parallel to the OH dipole. To quantify OH contents of anisotropic crystals, polarized measurements should be carried out with the electrical field vector parallel to the three axes of the indicatrix (Figure 2.1-7) (Libowitzky and Beran, 2004).

Infrared spectra were measured using a Bruker IFS 120 HR high-resolution Fourier-transform spectrometer coupled with a Bruker IR microscope. The principle of a Fourier-transform

spectrometer based on the Michelson interferometer is shown on Figure 2.1-8. It consists of two perpendicular mirrors, one of which is stationary while other moves at a constant velocity in the direction shown. Between these mirrors is a semitransparent beam splitter, at which the incoming beam is divided and later recombined after a path difference has been introduced between the two beams. This introduces a characteristic modulation of intensity for every frequency in the beam. After that the modulated light beam passes through the sample to the detector (from Kawata, 2002). From the modulation of the beam intensity seen by the detector, the intensity of each frequency in the beam can be calculated by Fourier transformation. Before measuring the sample, the spectrum of intensity versus frequency is first measured without the sample in the beam ("background measurement"). The actual absorption spectrum is calculated by comparing the intensity spectrum obtained with and without sample.

Near infrared (NIR) measurements were carried out using a tungsten light source, a Si coated CaF_2 beam splitter and a high-sensitivity narrow band MCT (mercury-cadmium-telluride) detector cooled with liquid nitrogen. Polarized infrared radiation was generated using an Al wire polarizor on a KRS-5 substrate.
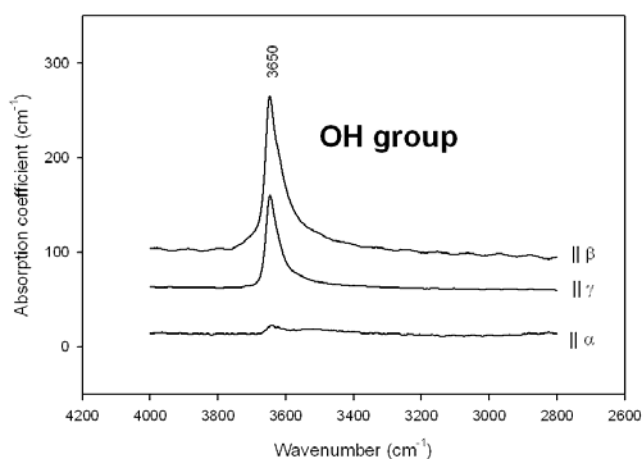
Figure 2.1-7. *Example of polarized IR spectra of diopside with hydroxyl absorption bands*
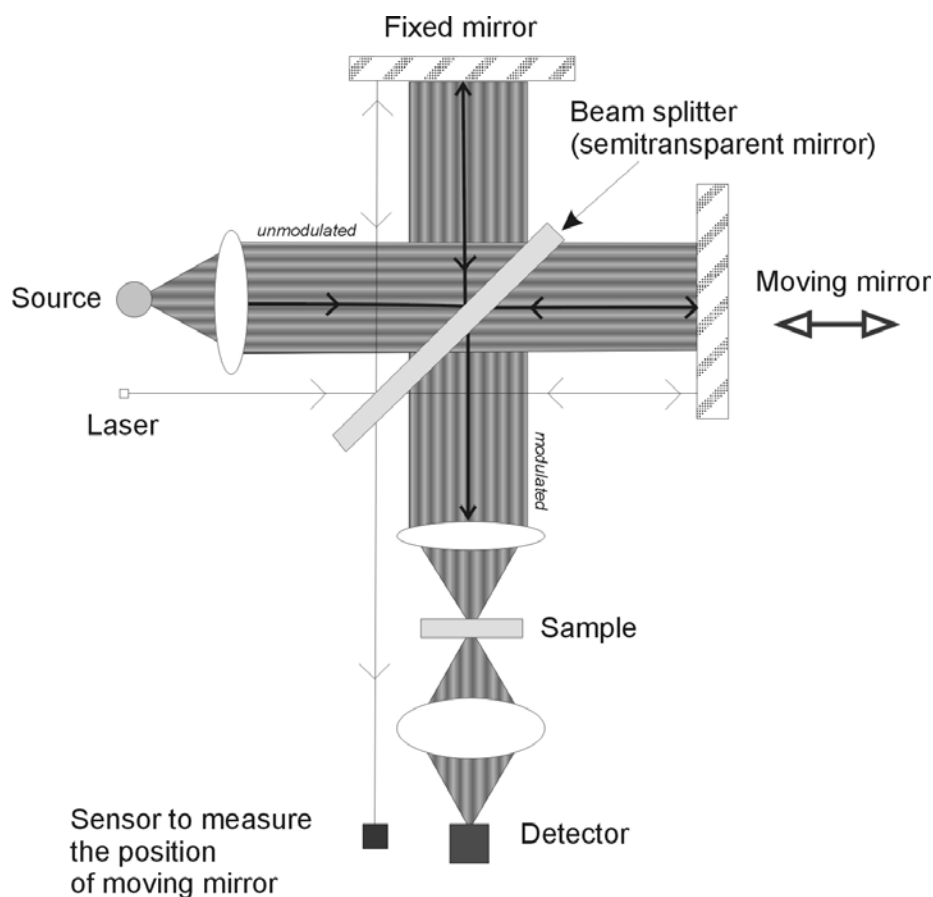
Figure 2.1-8. *Schematic drawing of a Fourier-transform spectrometer based on the Michelson interferometer (redrawn from Kawata, 2002)*

FTIR absorption spectra were obtained under a microscope with all-reflecting Cassegranian optics from optically clear areas of doubly polished crystals. Several hundred scans were accumulated for one measurement. All measurements were done by immersing the sample in polytrichlorofluoroethylene oil on a CaF_2 substrate in order to reduce interference fringes in the spectra arising from multiple reflections of the IR beam on the sample surface. The spot size was determined by an aperture in the rear focus plane of the objective.

Calculation of water content

The measurement of water contents by IR spectroscopy is based on the Beer Lambert law, where absorption of light depends on the thickness of the sample and on the concentration of the absorbing species:

$$A = \varepsilon \cdot c \cdot d$$

where **A** is absorbance [A = *log I₀/I*]

ε is the molar extinction coefficient [cm⁻¹/(*mol/l*)]

c   is concentration of the absorber [*mol/l*]

d   is sample thickness [cm].

The value of the extinction coefficient has to be determined by calibration against an independent method. In this study, two types of calibrations of extinction coefficients were used: Paterson (1982) and Bell et al. (1995).

According to the calibration suggested by Paterson (1982), there is a systematic relationship between the extinction coefficient and the stretching frequency of the OH group:

$$C_{OH} = \frac{Xi}{150\xi} \int \frac{K(\bar{v})}{(3780 - \bar{v})} d\bar{v}$$

where C_{OH} is the concentration of hydroxyl (in ppm H_2O)

ξ is the orientation factor which is 1/3 for unpolarized measurements

$K(\bar{v})$ is the absorption coefficient (in cm⁻¹) for a given wavenumber $\bar{v}$.

Xi is a density factor given by: $Xi = \frac{18}{2 \times d} 10^6$, where *d* is density of mineral (in *g/l*); for pure diopside *d* = 3283 *g/l*.

The calibration of Paterson was established from a variety of substances, including silicate glasses, quartz and water in various solvents. This correlation suggests a linear increase of the extinction coefficient with wavenumber with an origin at 3780 cm⁻¹, as shown in Figure 2.1-9. The calibration made by Libowitzky and Rossman (1997) has a similar slope with origin at 3780 cm⁻¹, but it slightly deviates from Paterson's correlation.
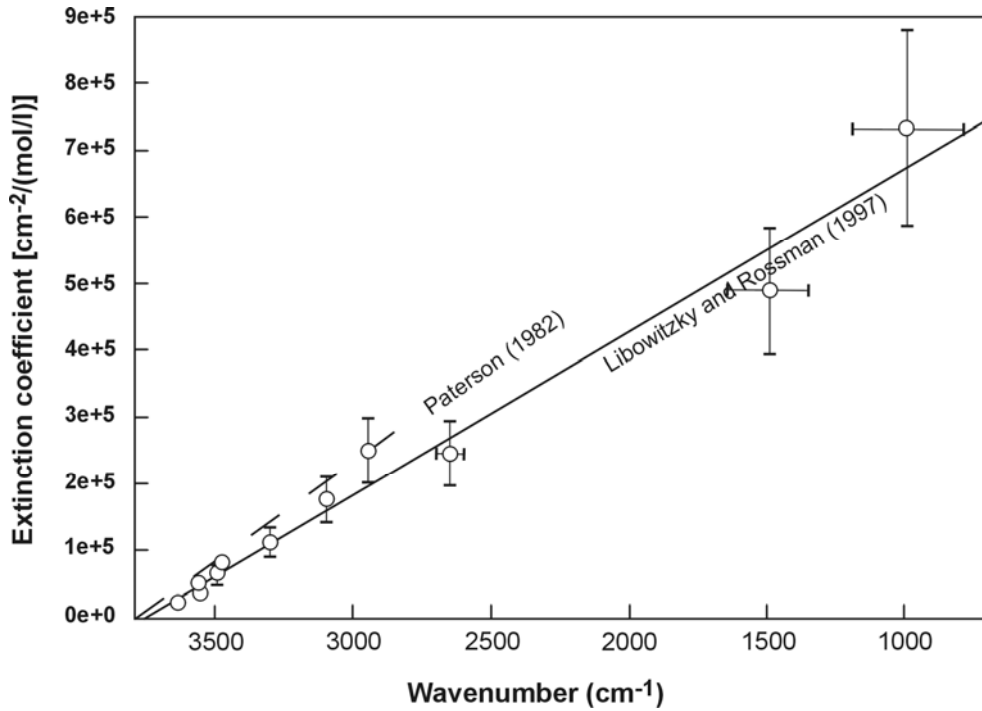
Figure 2.1-9. *Correlation of the extinction coefficient vs. wavenumber of the OH stretching bands. Redrawn from Libowitzky and Rossman (1997)*

In addition to the Paterson calibration, the calibration of extinction coefficients by Bell et al. (1995) was used:

$$C_{OH} = \frac{1}{I'} \int K(v)dv$$

where C_{OH} is the concentration of hydroxyl where

$K(v)$ is the absorption coefficient (absorbance per unit thickness) of the OH as a function of wavenumber

I' is the integrated extinction coefficient.

Bell et al. (1995) obtained calibration results roughly comparable to Paterson (1982), but with significant deviations for individual minerals. They used the extraction of H_2 gas under vacuum and manometry to measure the water content in garnet and pyroxenes samples. The integral

extinction coefficient (*I'*) for clinopyroxenes in their work equals 7.09 ± 0.32 [$1/(\text{ppm} \cdot \text{cm}^2)$], which was used for the calculations in this study.

The concentrations of the hydroxyl groups for all experiments were calculated from the infrared spectra by integrating the absorption bands in region around 4000-2500 cm^{-1}. Background and thickness corrections were applied. The method used for correcting background was to fit the background shape as a spline curve which was drawn through several chosen points. The points for background were chosen under absorption bands as shown on Figure 2.1-10.
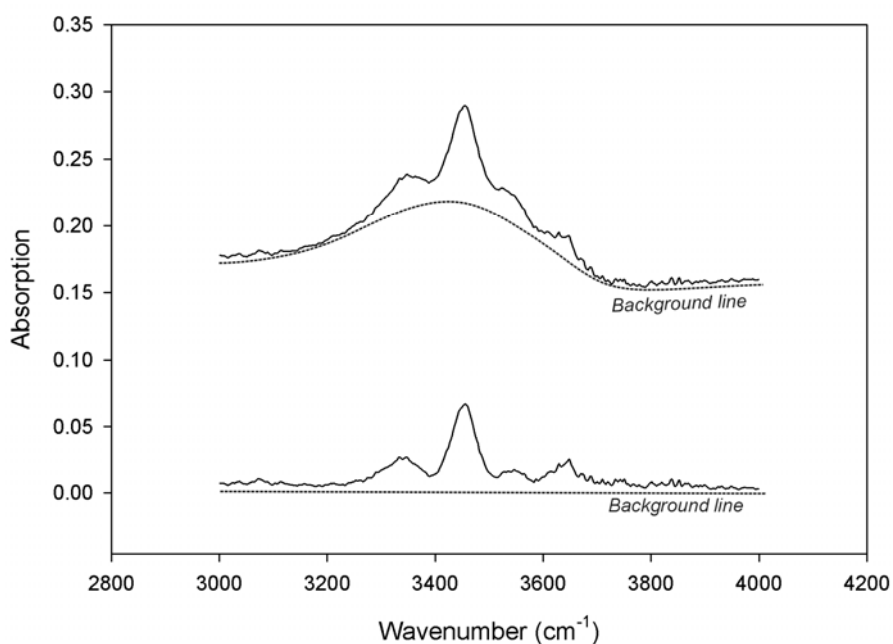
Figure 2.1-10. *Principle of background correction of IR spectra of diopside*

Polarized measurements

The principles of measurements of absorbance in anisotropic crystals were described by Libowitzky and Rossman (1996) in detail.
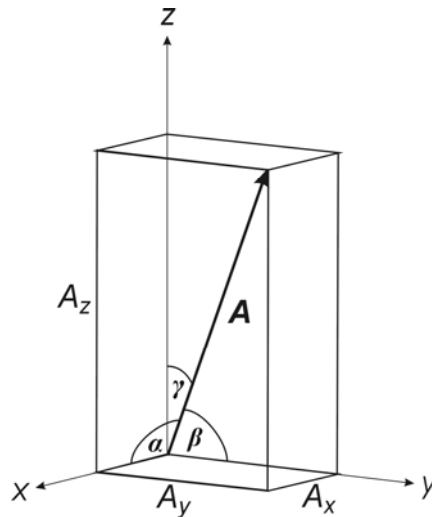
Figure 2.1-11. *Orientation and intensity of an absorber within a crystal*

(after Libowitzky and Rossman, 1996)

IR light linearly polarized parallel to one of the principal indicatrix directions is absorbed according to the projection of an absorber onto the electric vector of polarized light according to:

$$A(\theta) = A \cos^2 \theta$$

$A(\theta)$ is the projection of A onto the **E** vector of light. θ is the angle between E and the principle axis of the indicatrix. According to this equation the absorbance along the axes of the indicatrix (Figure 2.1-11) is given by:

$$A_x = A \cos^2 \alpha \qquad A_y = A \cos^2 \beta \qquad A_z = A \cos^2 \gamma$$

where α, β and γ describe the inclination of the absorber towards the three orthogonal axes (x, y, z) and are related by:

$$\cos^2 \alpha + \cos^2 \beta + \cos^2 \gamma = 1$$

The total absorbance is obtained by:

$$A_{tot} = A_x + A_y + A_z$$

In the case of monoclinic diopside (Figure 2.1-12) polarized IR spectra were measured along three indicatrix axes (x, y, z). First, a single crystal was oriented and double polished perpendicular

to the (100), (010) or (001) planes. After that the indicatrix axes were optically determined on one of the planes based on the angle of extinction between crossed polarizers and on the observation of the addition or subtraction of interference colors with a compensator.
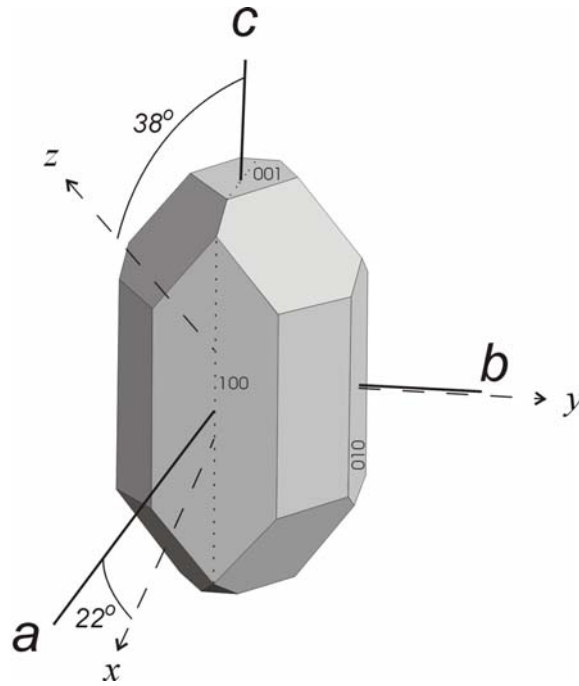
Figure 2.1-12. *Diopside single crystal with monoclinic lattice parameters axes (a, b, c)*
and indicatrix axes (x, y, z)

2.1.4.3. Powder X-ray diffraction

For phase identification in run products, powder X-ray diffraction patterns were collected from all samples with the Siemens D5000 diffractometer at BGI, using CuKα radiation, in most cases in the 2θ range from 20° to 120°. In some cases full profile refinements on the run products were done using the General Structure Analysis System (GSAS, Larson and Von Dreele, 1994) program and the windows interface, EXPGUI (Toby, 2001).

2.1.4.4. Single crystal X-ray diffraction

Intensity data collections for the structural refinements of diopside were performed on a Xcalibur diffractometer (operated at 50 kV and 40 mA and equipped with a CCD detector) using MoK_α radiation (graphite monochromator) with the crystals mounted on glass fibers. A combination of *omega* and *phi* scans was used to obtain a coverage of half reciprocal sphere up to $2\theta_{max} = 80°$. An exposure time of 20 s/frame for cpx_1, 15 s/frame for cpx_2, 20 s/frame for cpx_3 and 10 s/frame for cpx_4 was used. The sample-detector distance was 50 mm. Reflection intensities were corrected taking into account Lorenz and the polarization factors using the CrysAlis package (Oxford Diffraction, 2006). An analytical absorption correction based on the crystal shape, for which the degree of absorption is related to the distance traveled through the sample and to its composition (through an absorption coefficient), was performed using the same CrysAlis Package (Oxford Diffraction, 2006).

In addition, we used single crystal diffraction to select single crystals suitable for further high-pressure X-ray diffraction experiments to determine the elastic properties of water-saturated diopside. Moreover, diopside crystals were oriented for infrared measurements with a single-crystal four-circle Huber diffractometer (with Mo$K\alpha$ radiation, operating at 50 kV and 40 mA).

2.2. High-pressure X-ray diffraction experiments

One of the aims of this study was to determine the effect of water on the elastic properties of diopside. For that purpose, high-pressure X-ray single-crystal diffraction experiments were carried out using a diamond anvil cell (DAC).

2.2.1. Diamond anvil cell

The principle of DAC experiments is to use two gem-quality diamonds to apply a force to a sample. The size of the diamond culet (the working area of a DAC) determines the maximum pressure that can be achieved during an experiment. A detailed description of the diamond-anvil cell technique may be found in Miletich et al. (2000). The sample and a pressure calibrant were placed in a pressure chamber created between the flat parallel faces (culets) of two opposed diamond anvils and a gasket (metal foil with a hole drilled in the middle). The free volume of the chamber is filled with a pressure-transmitting medium. It should be a fluid which exerts a hydrostatic pressure on the sample (Figure 2.2-1).

Pressure is generated by forcing the two opposite diamond anvils together. The force-generating mechanism in most diamond cells used for X-ray diffraction consists of two platens, which support the two diamond anvils, and several tightening screws, which force them together (Figure 2.2-2).

Ruby is often used as pressure calibrant in diamond cells. Ruby, Cr^{3+} doped α-Al_2O_3, is known to be stable without phase transition up to megabar pressures. Ruby has a strong fluorescence spectrum which depends on pressure. The spectrum consists of two sharp band components at 694.2 nm (*R*1) and 692.8 nm (*R*2). During compression, the *R*1 and *R*2 lines shift to higher wavelengths (Figure 2.2-3).
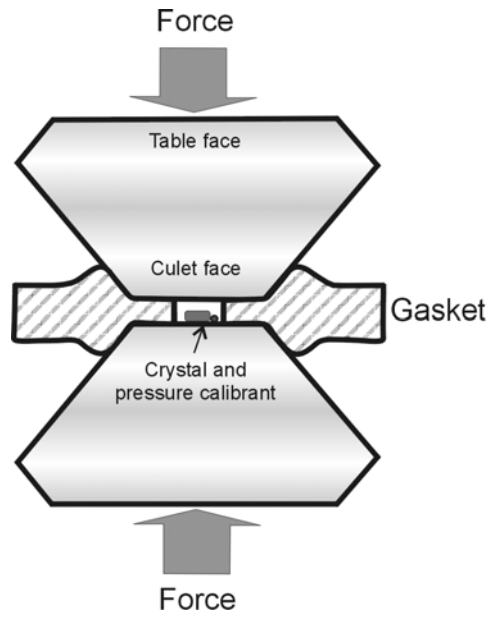
Figure 2.2-1. *Principle of pressure generation in diamond anvil cell*
(redrawn from Miletich et al., 2000)
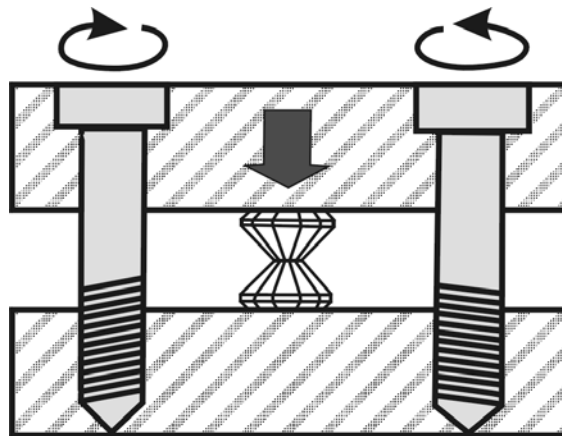
Figure 2.2-2. *Schematic drawing of force generating mechanisms*
(redrawn from Miletich et al., 2000)
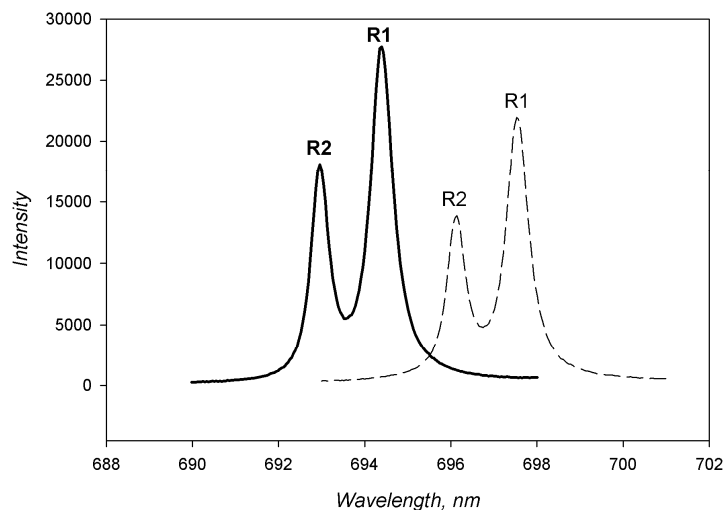
Figure 2.2-3. *Ruby fluorescence lines shift with pressure, as measured by a Raman spectrometer;*
the solid line corresponds to ambient pressure; the dashed line correspond to pressure of 9.3 GPa.

Pressures may be calculated according to Mao et al. (1986) by the following formula:

$$P = A / B \{[1+(\Delta\lambda / \lambda_0)]^B - 1\}$$

where P is pressure in megabars

λ is the wavelength of the ruby R line

$A = 19.04 \quad B = 7.665$

In this study, the high-pressure diffraction experiments were performed with a diamond-anvil cell of BGI – design (Bayerisches Geoinstitut) (Figure 2.2-4), Type I diamonds (0.3 carat) with culet size of 600 μm were used together with steel gaskets pre-indented to a thickness of 90 μm and with a hole of 300 μm diameter. A 4:1 mixture of methanol:ethanol was used as hydrostatic pressure medium. Ruby spheres were used as pressure calibrant. Ruby fluorescence was measured with Jobin Yvon LABRAM spectrometer. The fluorescence was excited with a 632.8 nm HeNe laser.
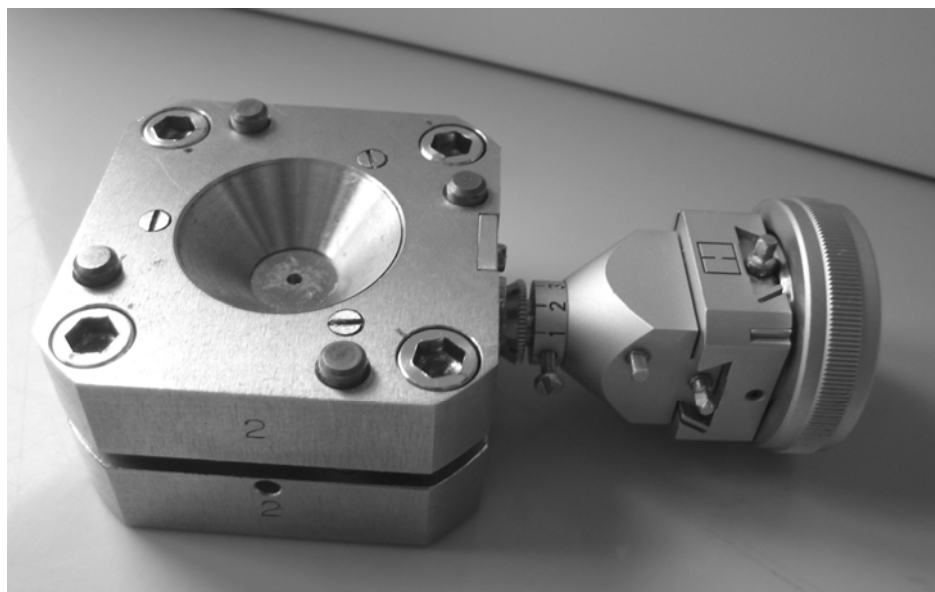
Figure 2.2-4. *The BGI diamond-anvil cell used for high-pressure X-ray diffraction experiments*

2.2.2. Four-circle X-ray single-crystal diffractometer

After the cell was prepared, unit-cell parameters of diopside single crystals were determined at each pressure using a four-circle Huber diffractometer (with Mo$K\alpha$ radiation) operating at 50 kV and 40 mA, at room temperature. The eight-position centering procedure of each diffraction peak was used (King and Finger, 1979). The procedure consists of centering a single reflection at the 8 equivalent positions on the diffractometer. The setting angles of a single reflection always deviate from the "true" angles as a result of a number of experimental aberrations (Angel et al., 2000). These aberrations may include offsets of the crystal from the center of the goniometer, absorption by the crystal and a number of diffractometer aberrations (incorrect zero position). Therefore, using the 8-position technique provides more precise results. All details for high-pressure diffractometry are described by Angel et al. (2000).

The SINGLE04 software written by Angel was used as a diffractometer control software package. This program carries out the calculations necessary for controlling the four-circle Huber diffractometer. It incorporates all of the conventions for geometry, the requirements for DACs and the algorithms for eight-position peak-centering.

3. RESULTS

3.1. Water solubility in clinopyroxene

3.1.1. Water solubility in pure diopside

3.1.1.1. Exploratory experiments

In some exploratory experiments, diopside single crystals were synthesized at 20-30 and 100 kbar and 800-1100°C from an oxide and hydroxide starting mixture (see Section 2.1.1) containing 10 % excess silica. The duration of each experiment was from 2.5 up to 3 days. Most experiments were carried out in the piston cylinder apparatus with pyrophyllite sleeves around the sample capsule. Two experiments were performed in multi-anvil apparatus at 100 kbar and 1000°C or 1100°C, for 8-10 hours. After each experiment, the capsule was checked for the presence of excess water, see Table 3.1-1.

The colorless samples recovered from the capsule were in the form of crystalline mass with a small amount of larger single crystals of diopside. Clear inclusion-free crystals were used for further investigations.

The sizes of the diopside crystals usually reached up to 50-100 µm, in some cases up to 200 µm. Some of the crystals are shown in Figure 3.1-1. Because of the small size of the crystals only some of them were used for further analysis and infrared measurements.
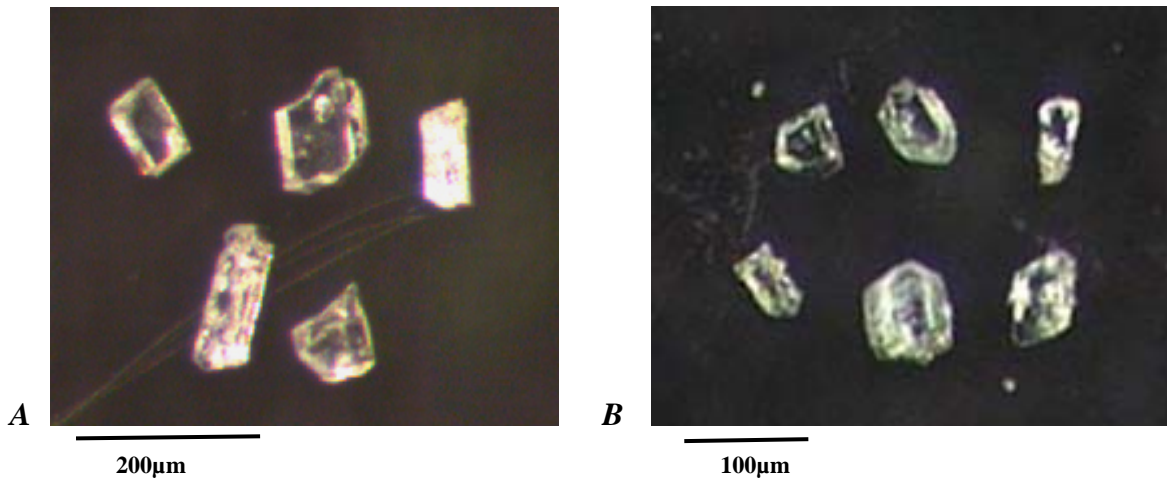
Figure 3.1-1. *Diopside crystals synthesized at 30 kbar, 1100 ˚C (A) and at 25 kbar, 800 ˚C (B)*

X-ray powder diffraction was used for phase identification after each experiment. In some cases the full-profile Rietveld refinements of the run products have been performed. It was observed that the run products of some experiments were slightly different. In most of the samples the run products were diopside with a small amount of coesite (or quartz). Olivine was present in several run products (#4, #19) in the form of large (up to 100 μ) colorless crystals, which were identified by Raman spectroscopy. It may indicate high activity of MgO in the experiment. The presence of olivine in some run products may be related to the preferential dissolution of silica in the aqueous fluid. Alternatively, it may be due to some chemical inhomogeneity of the starting mixture. There was no difference noted in the run products between piston-cylinder and multi-anvil experiments. Experimental details, run conditions and products as well as calculated water contents are tabulated in Table 3.1-1.

Most of the diopside crystals were chemically pure, corresponding to the ideal diopside formula $CaMgSi_2O_6$. The chemical analyses for each experiment are presented in the Appendix 1. Ca, Mg and Si as well as Al concentrations were analyzed for all pure diopside crystals. A slight contamination of the samples by Al cannot be completely ruled, although the measured Al concentrations were close to the detection limit.

Table 3.1-1. *Experimental details, run products and average water content calculated from FTIR spectra of pure diopside crystals from the exploratory experiments*

# exp.	Conditions		Layered (L) or homogeneous (H) starting material*	Water out of the capsule after experiment	Water loss from capsule after drying (%)**	Run products	*n* and type of spectra	Water content (ppm H$_2$O)	
	P (kbar)	T (°C)						Paterson (1982)	Bell et al. (1995)
# MP-2	100	1100	H	no	56	diopside	1 (p), I	251	300
# MP-1	100	1000	H	no	74	diopside, coesite	2 (u), I	164 ± 22	138 ± 17
# 4	30	1100	L	no	65	diopside, olivine	1 (p), II	169	201
# 24	30	1000	L	yes	54	diopside, coesite[a]	1 (p), II	665	728
# 21	30	900	L	no	66	diopside, coesite	1 (p), I	300	397
# 22	30	800	L	yes	20	diopside	1 (p), I	189	208
# 17	25	1100	L	yes	65	diopside	2 (u), I	55 ± 5	63 ± 5
# 20	25	1000	H	no	60	diopside, quartz[a]	3 (u), II	151 ± 22	166 ± 43
# 42	25	900	H	yes	59	diopside	2 (u), I	167 ± 28	180 ± 35
# 23	25	800	L	yes	10	diopside, quartz[a]	1 (p), I	358	395
# 43	20	1100	H	no	69	diopside, quartz	3 (u), II	125 ± 38	153 ± 22
# 19	20	800	H	yes	60	diopside, olivine[b]	3 (u), II	143 ± 8	119 ± 13

* The starting material for diopside synthesis contained 10% excess of SiO$_2$ for each experiment

** in % of the total amount of water loaded, the starting amount of water for PC experiment was 0.030-0.035 g and for MA experiments – 0.0035 g.

n – number of measurements; (p) –data were calculated based on polarized measurements; (u) - on unpolarized measurements.

a – mineral was identified in run products by microprobe analyses; b – by Raman spectroscopy.

All infrared spectra measured from pure diopside show several absorption bands in the region between 3000 and 3500 cm^{-1}, which are assigned to O-H stretching modes. For all experiments with pure diopside, water contents were relatively small, in the order of several hundreds ppm H$_2$O. Water contents in pure diopside range from 63 ppm H$_2$O at 25 kbar and 1100°C to 728 ppm H$_2$O at 30 kbar and 1000°C. Unpolarized spectra for diopside crystals from all experiments are shown on Figure 3.1-2. The water content calculated from every experiment and run products are presented in Table 3.1-1.
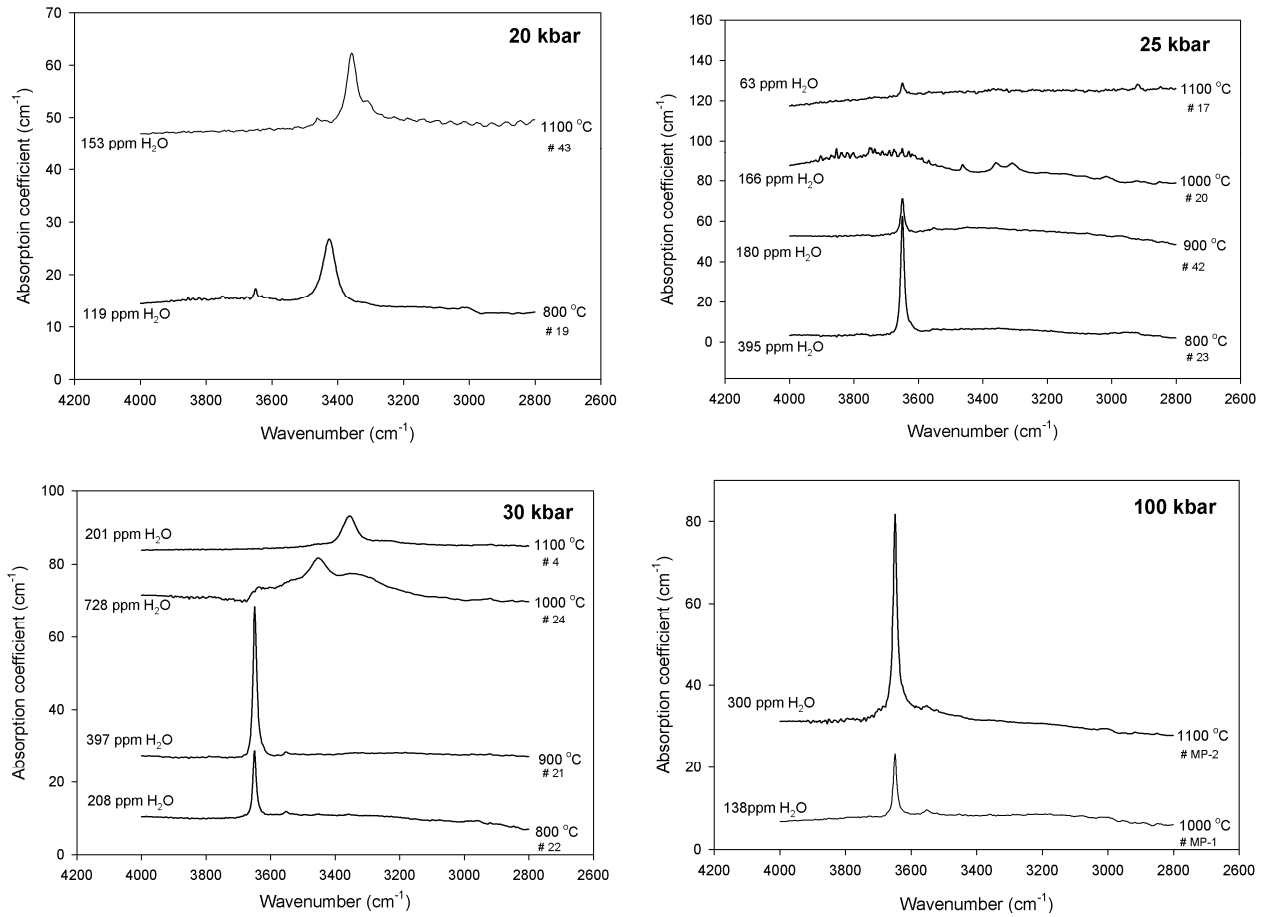
Figure 3.1-2. *Unpolarized infrared spectra for pure diopside synthesized at different conditions*
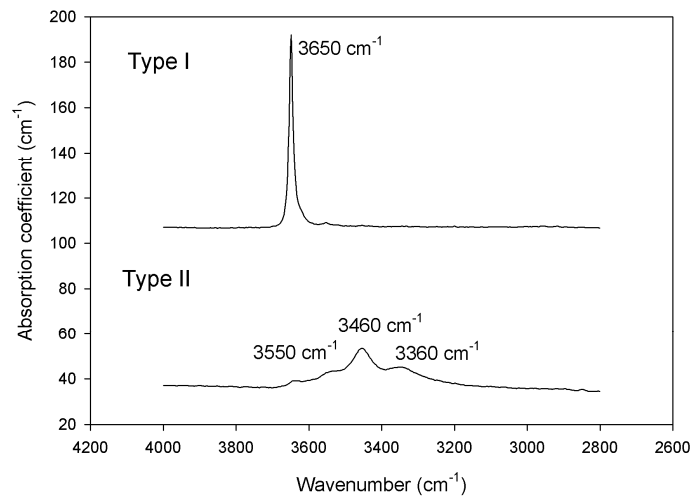
Figure 3.1-3. *Two different types of IR spectra observed for pure diopside*
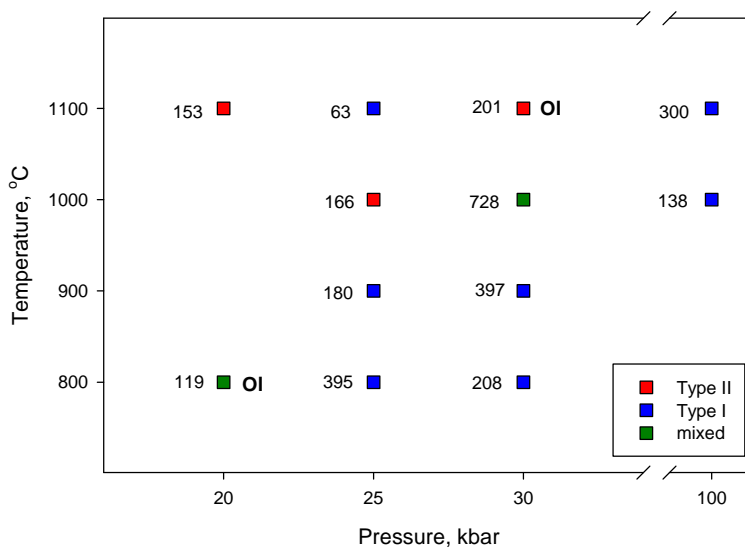
***Figure 3.1-4.** Experimental conditions for diopside synthesis.*
*The calculated water concentration (in ppm H_2O) for the experiments is shown close to each point. The type of infrared spectra is indicated by different colors: blue points – spectra with absorption bands at 3650 cm^{-1}, red – with bands at 3357 cm^{-1} and green points – with several absorption bands including both 3650 and 3357 cm^{-1}. **Ol** indicates the presence of olivine in run products.*

Two groups of absorption bands were observed in the infrared spectra of pure diopside samples. The first group (Type I) occurs at higher wavenumbers, at 3650 cm^{-1}; and the second group (Type II) at lower wavenumbers, at 3480-3280 cm^{-1} (Figure 3.1-2 and 3.1.3). The spectra of the first group were observed for diopside crystals synthesized at 25 kbar and 800, 900, 1100°C, at 30 kbar and 800, 900°C, at 100 bar and 1000, 1100°C. The second group spectra were observed in experiments at 20 kbar and 800, 1100°C, at 25 kbar and 1000°C, at 30 kbar and 1000, 1100°C. The experimental conditions and the types of absorption bands as well as calculated water content are presented on Figure 3.1-4.

The spectra of Type I always look the same, showing only one sharp absorption band at 3650 cm^{-1} and one additional band at 3550 cm^{-1} with very low intensity. The spectra of Type II are more variable. In come cases they show only one absorption band at 3350 cm^{-1} (e.g., 30 kbar and

1100°C). Some of the infrared spectra of Type II show several absorption bands with the strongest ones at 3357 and 3460 cm^{-1} (e.g., 25 kbar, 1000°C; 20 kbar and 1100°C).

Figure 3.1-5(*A*) shows polarized spectra of diopside synthesized at 25 kbar and 800°C (Type I spectra). There is only one major O-H absorption band for this sample at 3650 cm^{-1} for three different orientations. Figure 3.1-5(*B*) shows polarized Type II spectra of diopside (30 kbar, 1100°C) with absorption bands at 3356 cm^{-1}. It was established for both types of spectra that the O-H group is located mostly between *(010)* and *(001)* crystallographic planes.
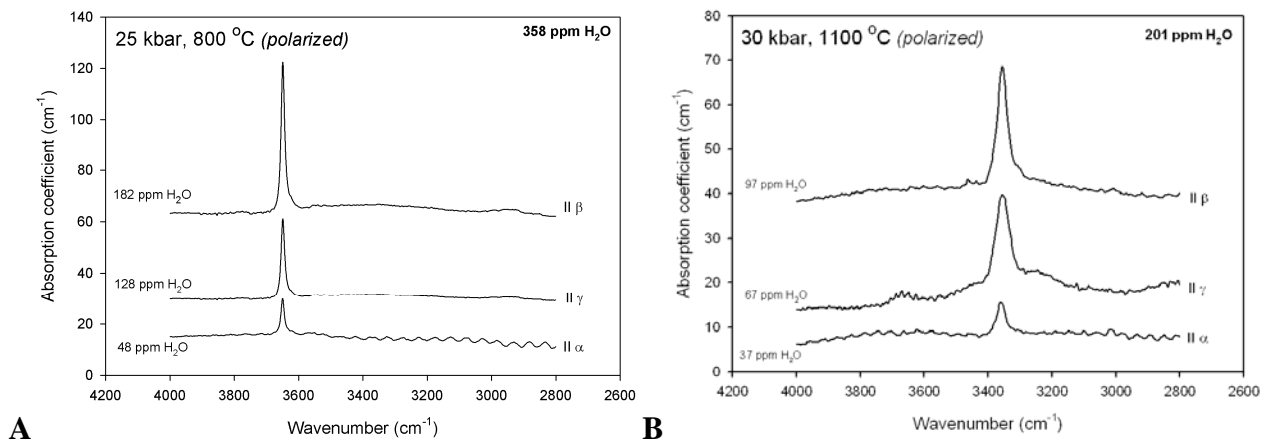
Figure 3.1-5. Polarized infrared spectra with different orientation of the electrical field vector E for diopside crystals synthesize at 25 kbar, 800°C (A) and at 30 kbar, 1100°C (B)

From these exploratory experiments, it was not possible to establish any systematic dependence of water solubility on pressure or temperature. Moreover, the appearance of Type I or Type II spectra was neither correlated with pressure, temperature or the phases present the run (diopside plus olivine or coesite). It is possible, however, that in particular coesite may be a quench phase precipitated from the fluid. This phase may not have been stable under these conditions. A possible explanation for the unsystematic results could also be a slight contamination of some samples by alumina from the pyrophyllite sleeve around the capsule.

3.1.1.2. Effect of activities of components in the system on infrared spectra

The differences in the spectra point towards substitution mechanisms involving different vacancies, which in turn could be the result of different oxide activities in the starting material. To examine this hypothesis, another series of experiments has been carried out. The starting materials for each of these experiments were prepared with a large excess or deficiency of $Mg(OH)_2$ or SiO_2 components. Details of the chemical compositions of starting materials are listed in Table 2.1-1 (in section 2.1). All experiments were carried out in the piston-cylinder apparatus at 30 kbar and 900^oC, the duration of each experiment was 3 days. MgO sleeves were used around the sample capsules to avoid any contamination by alumina.

Table 3.1-2. *Experimental conditions, run products and average water content calculated from FTIR spectra of pure diopside crystals*

# exp.	Conditions		Starting material *	Water coming out of the capsule after experiment	Water loss from capsule after drying (%)**	Run products	n and type of spectra	Water content (ppm H_2O)	
	P (kbar)	T (^oC)						Paterson (1982)	Bell et al. (1995)
# 55	30	900	30 wt.% excess SiO_2 (H)	no	98	diopside, coesite	1 (p), II	208	293
# 56	30	900	5 wt.% deficiency SiO_2 (H)	yes	57	diopside, coesite	1 (p), I	342	397
# 57	30	900	15 wt.% excess $Mg(OH)_2$ (H)	no	84	diopside, olivine[a]	1 (p), I	289	308

* the starting material was homogeneous for each experiment (H);

** in % of the total amount water loaded, the starting amount of water for PC experiment was 0.033-0.037 g;

n – number of measurements; (p) –data were calculated based on polarized measurements;

a – mineral was identified in run products by Raman spectroscopy.

Results of the experiments are presented in Table 3.1-2 and Figure 3.1-6. Run products were diopside and a small amount of coesite for experiments #55 and #56, with excess and deficiency of SiO_2 in starting material respectively. In experiment #56 coesite may be a quench phase. In experiment #57 (with excess of $Mg(OH)_2$ in starting material) diopside together with olivine was found. Microprobe analyses (see Appendix 1) show that in the run #55 where an excess of silica in

the starting material was used, there may be vacancies in both Ca and Mg positions. For the run #57 (excess of Mg) some deficiency in the Si position was observed.

Depending on excess or deficiency of the SiO_2 and MgO components, the infrared spectra show different types of absorption bands. Starting materials with low silica activity yielded Type I bands, at 3650 cm^{-1} wavenumber. The absorption bands in this range were proposed by Stalder and Ludwig (2007) to be assigned to an Si-vacancy in the *T* site or the other tetrahedral defects. They suggested that it might be diagnostic for a low silica activity. When a starting material with an excess of SiO_2 component was used, the appearance of several absorption bands at 3650, 3540, 3460, 3360 cm^{-1} was observed (Type II spectra). According to Stalder and Ludwig (2007) the absorption band at 3360 cm^{-1} may be related to Mg-vacancies in the *M2* site in the diopside structure. Smyth et al. (1991) proposed that the 3460 cm^{-1} absorption band correlated with Ca-Eskola component (vacancy in *M2* site).

Based on these observations, we assume that spectra of Type II might be assigned to a combination of protonated Mg (*M1*) and Ca (*M2*) vacancies in diopside for combined spectra with both 3357 and 3460 cm^{-1} absorption bands. Only one single band at 3357 cm^{-1} (also Type II) may be related to a protonated vacancy in the Mg (*M1*) site.
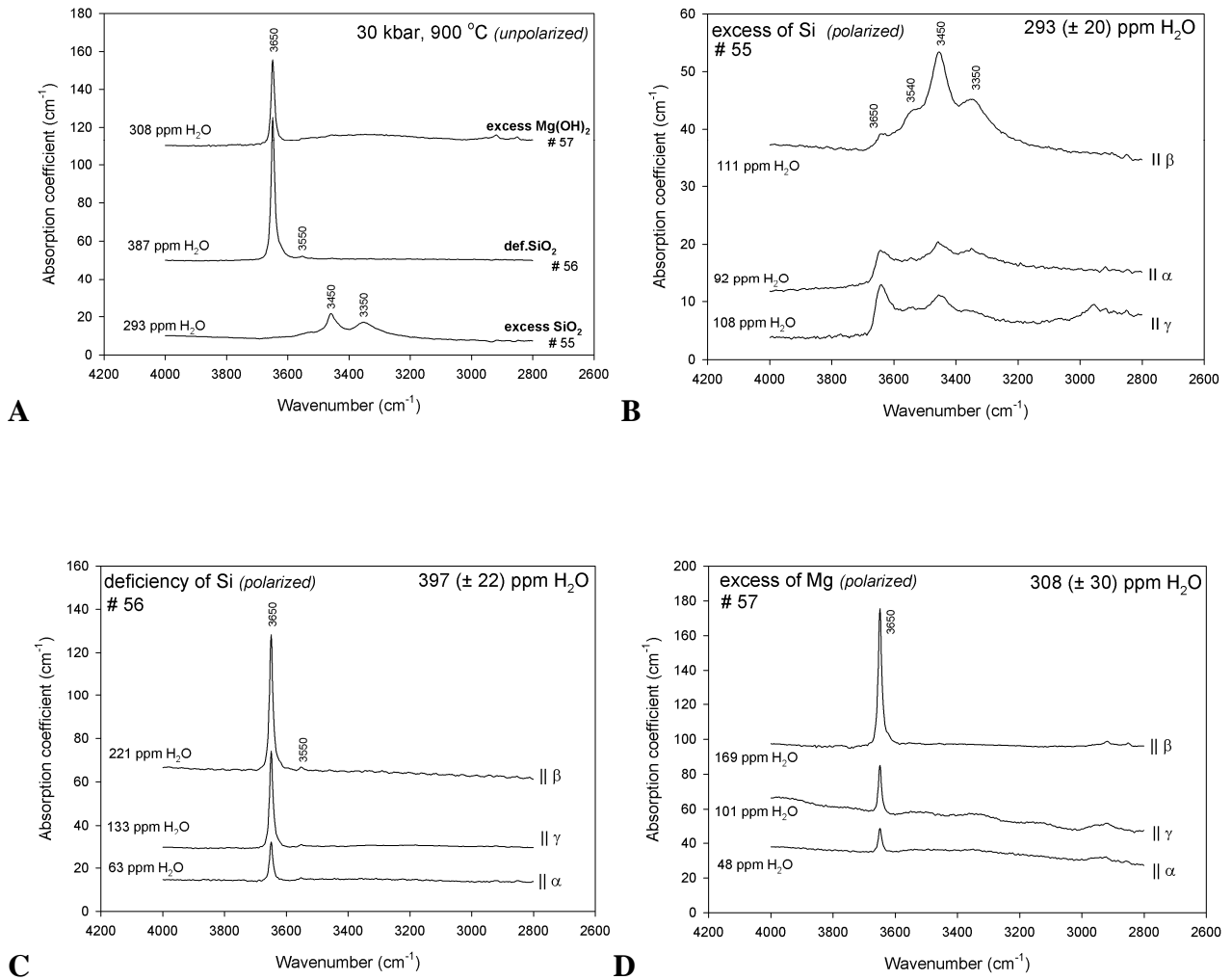
Figure 3.1-6. *Infrared spectra of the diopside crystals synthesized at 30 kbar and 900°C with different compositions of starting material.* **A** *– unpolarized spectra for each experiment;* **B** *– polarized spectra of diopside synthesized with starting material having 30 wt.% excess SiO_2;* **C** *– 5wt.% deficiency of SiO_2;* **D** *– 15 wt.% excess $Mg(OH)_2$.*

3.1.1.3. Orientation of hydroxyl group

From the observed infrared spectra it is possible to determine the location of the protons in the diopside structure. The frequency of the O-H stretching vibration is controlled by the strength of the hydrogen bond. According to Libowitzky (1999) there is a correlation of O-H stretching frequencies with O…O and H…O bond lengths in minerals (Figure 3.1-7). Therefore, the length of the OH bond can be estimated from that correlation. Moreover, an OH group may absorb infrared radiation only if a component of the electrical field vector (***E***) of the incident wave is parallel to the OH dipole. Thus, it is possible to determine the orientation of the OH group within the crystal structure from polarized infrared absorption measurements.
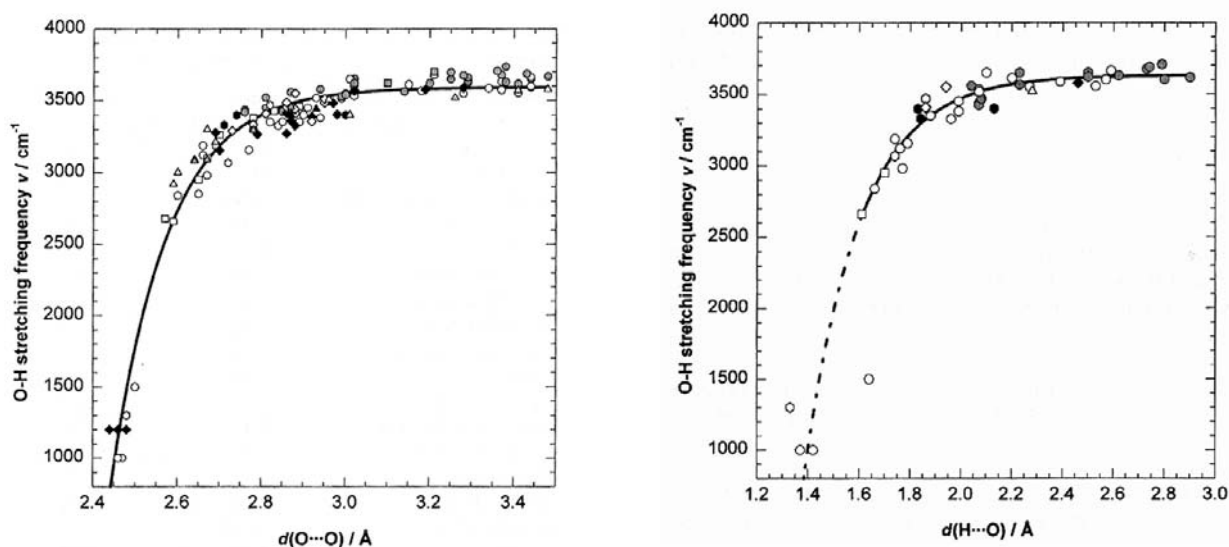
Figure 3.1-7. *Correlation between OH-stretching frequency and O-H…O (left) and H…O (right) distances (redrawn from Libowitzky, 1999)*

First, according to the equations described by Libowitzky and Rossman (1996) (see also section 2.1.4.2) the angles between the O-H dipole vector and the three indicatrix axes were calculated. Since the indicatrix axes do not coincide with the crystallographic axes of diopside (see Figure 2.1-12 in section 2.1.4.2) these data were converted to angles between the O-H dipole vector and the crystallographic *a*, *b* and *c* axes.

As discussed in the introduction (section 1.3.3), the O2 position is the most favourable site for OH substitution in clinopyroxene (Cameron and Papike, 1980; Skogby et al., 1990; Gatzemeier and Wright, 2006). Bromiley et al. (2004) suggested 3 major mechanisms for hydrogen incorporation in diopside. The mechanism 1 involves a hydrogen atom attached to the O2 atom with vibration of the OH dipole in the direction of the O3 atom (along the edge of an *M2* polyhedral site). Mechanism 2 involves hydrogen bonded to the O2 atom and vibration of the OH dipole in the direction of the O1 site, along a shared *M1-M2* polyhedral edge. Mechanism 3 corresponds to hydrogen on the O2 oxygen pointing towards another O2 atom along the edge of an *M1* octahedron.

For the polarized infrared spectra of diopside of Type I with one absorption band at 3650 cm^{-1} a Si vacancy in the tetrahedral site was assumed (see for example Figure 3.1-5 A). For the given O-H stretching frequency of 3650 cm^{-1}, the oxygen-oxygen bond length corresponds to ~3.0-3.4 Å (see Figure 3.1-7 left). The angles between the O-H dipole vector and the three indicatrix axes are 70° to the *α*-axis, 36° to the *β*-axis and 62° to the *γ*-axis (Table 3.1-3). The angles of the OH dipole relative to the crystallographic axes are 61° to the *a*-axis, 36° to the *b*-axis and 81° to the *c*-axis (Table 3.1-3). Using these angles, orientation vectors [*u,v,w*] of the O-H group were calculated. These vectors (blue) starting from an O2 oxygen atom and pointing to the approximate location of the hydrogen atom are shown in Figure 3.1-9. Then, according to the three types of mechanisms proposed by Bromiley et al. (2004) and two additional possibilities (see Figure 3.1-9) the angles between O-O vectors and the *a*, *b* and *c* axes were calculated from the crystal structure. Table 3.1-3 shows the calculated angles only for three major mechanisms (Bromiley et al., 2004) because the two other ones strongly deviated from the observed OH dipole direction. Therefore, based on the correlation of Libowitzky (1999), which suggests a O-O distance of ~3.0-3.4 Å and on the comparison of calculated and measured angles from Table 3.1-3 it was inferred that infrared spectra of Type I suggest: a) Si vacancy in the tetrahedral site; b) mechanism 1 with bonding of the hydrogen atom to the O2 oxygen and the O-H dipole pointing to the O3 oxygen atom corresponding to a distance O2-H…O3 of 3.072 Å (see Figure 3.1-10). Moreover, since the O-H…O angle in a hydrogen bond in crystal structures of minerals usually equals less than 180° (see scheme on Figure 3.1-8), the small deviation between the OH dipole vector and the vector between the O2 and O3 atoms can be explained.

Table 3.1-3. *Measured and calculated angles between the OH dipole direction and the monoclinic lattice axes in the diopside structure for infrared spectra of Type I*

Measured angles (obtained from polarized infrared measurements)		Calculated angles for different O-O directions		
		1. along *M2* edge O2-O3 with 3.072 Å	2. along *M1-M2* edge O2-O1 with 2.975 Å	3. along *M1* edge O2-O2 with 2.984 Å
ψ α 70°	ψ a 61°	**58°**	47°	13°
ψ β 36°	ψ b 36°	**48°**	61°	90°
ψ γ 62°	ψ c 81°	**69°**	70°	61°

Figure 3.1-8. *Schematic illustration of hydrogen bonding which is a donor-acceptor interaction involving hydrogen atom in the moiety O-H⋯O*
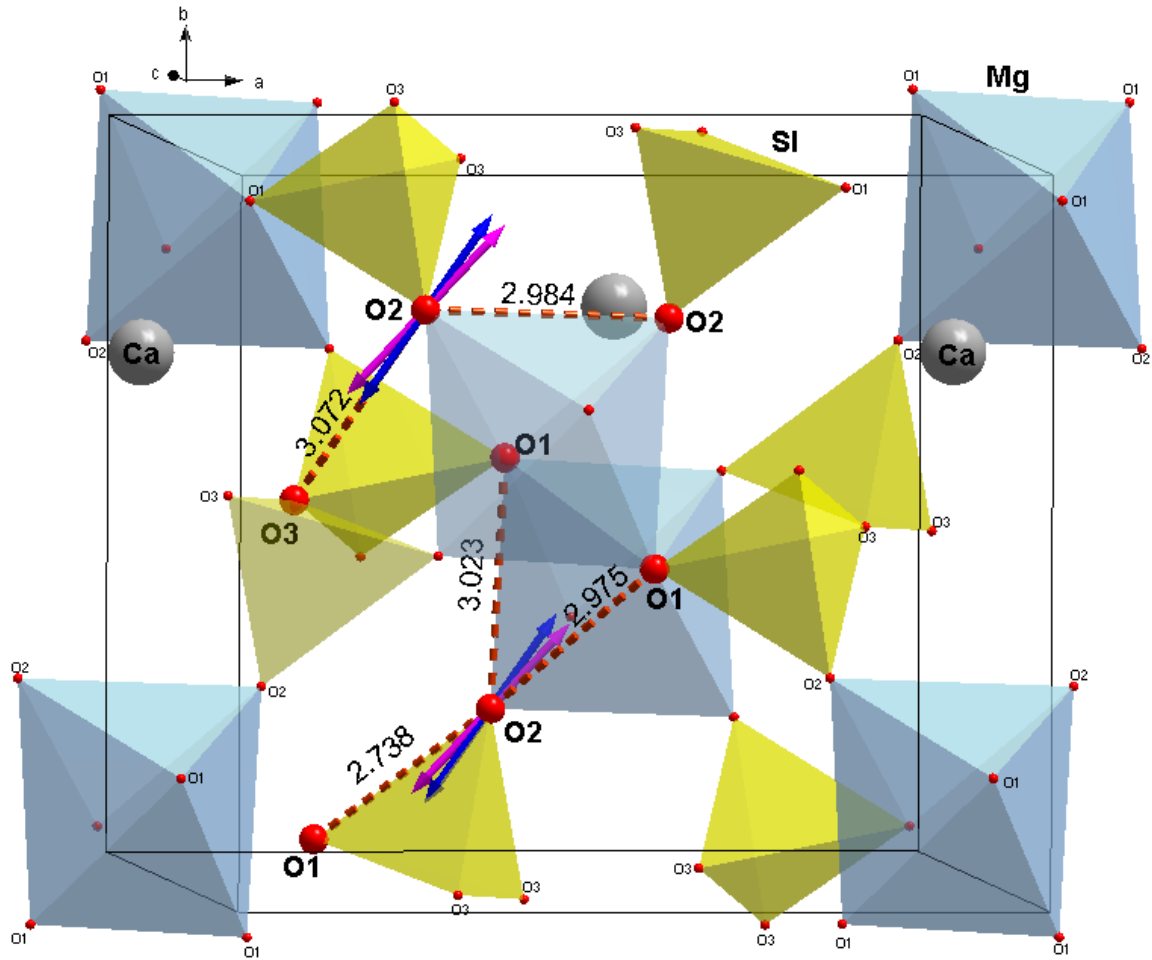
Figure 3.1-9. *Fragment of the crystal structure of diopside. Possible positions of the hydrogen atom and directions of hydrogen bonds determined from both Type I (blue vectors) and Type II (pink vectors) infrared spectra. Dashed O-O vectors with their lengths (in Å) show different possibilities for the vibrating directions of OH dipole.*
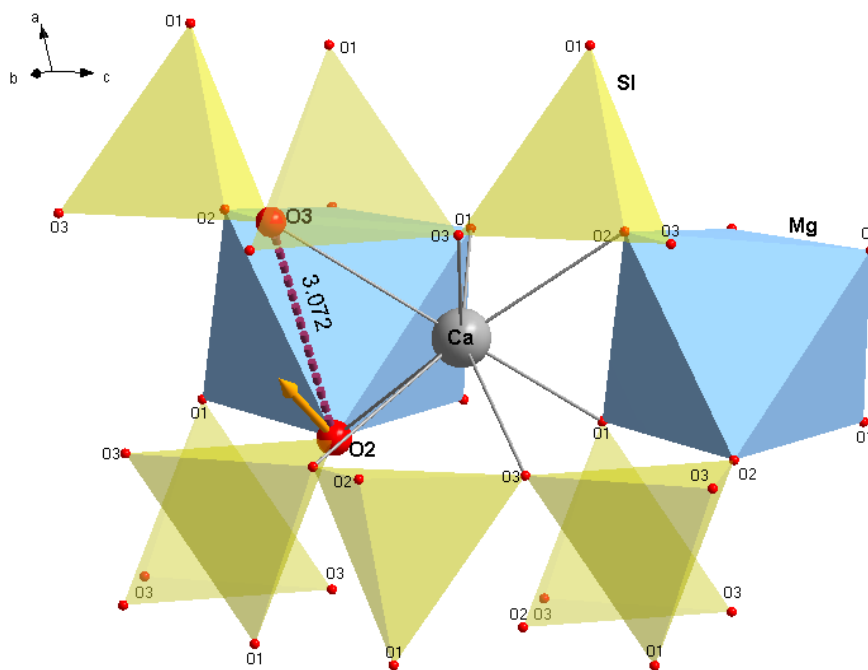
Figure 3.1-10. *Fragment of the crystal structure of diopside showing the direction of the hydrogen bond with a proton attached to the O2 oxygen atom and the OH dipole pointing to the O3 oxygen atom (mechanism 1). The end of the vector originating from O2 points towards the position of the proton. This is the mechanism responsible for Type I infrared spectra.*

Infrared spectra of Type II with only one strong absorption band at 3357 cm^{-1} were assumed to indicate a Mg vacancy in the octahedral site (see Figure 3.1-5 B). The O-O distance may vary for the observed O-H stretching frequency at 3357 cm^{-1} from ~2.6 to 3.0 Å (see Figure 3.1-7 left). According to the polarization of the absorption bands, the OH dipole is inclined 56° to the *a*-axis, 46° to the *b*-axis and 77° to the *c*-axis (Table 3.1-4). From these angles, orientation vectors [*u,v,w*] of the O-H group were calculated. These vectors (pink) starting from the O2 oxygen and pointing to the approximate location of hydrogen atom are shown on Figure 3.1-9. Then, according to the three types of mechanisms proposed by Bromiley et al. (2004) and two additional possibilities (see Figure 3.1-9) the angles between O-O bonds and *a*, *b* and *c* axis were calculated from the crystal structure of diopside, in the same way as for Type I spectra. Table 3.1-4 presents the calculated angles only for three major mechanisms (Bromiley et al., 2004) because the two other ones strongly deviated from the OH dipole direction. Therefore, based on the correlation of Libowitzky (1999) which suggests an O-O distance of ~2.6-3.0 Å and on the comparison of calculated and

measured angles from Table 3.1-4 it was inferred that spectra of Type II imply: a) a Mg vacancy in the *M1* octahedral site; b) mechanism 2 of hydrogen incorporation onto the O2 oxygen atom with the O-H dipole pointing to the O1 oxygen atom corresponding to distance O2-H…O1 of 2.975 Å (see Figure 3.1-11). The actual location of the proton is found to be inside the *M1* site.

Table 3.1-4. *Measured and calculated angles between the OH dipole direction and the monoclinic lattice axes in the diopside structure for infrared spectra of Type II*

Measured angles (obtained from polarized infrared measurements)		Calculated angles for different O-O directions		
		1. along *M2* edge O2-O3 with 3.072 Å	**2. along *M1-M2* edge O2-O1 with 2.975 Å**	3. along *M1* edge O2-O2 with 2.984Å
ψ α 68°	*ψ a* 56°	58°	**47°**	13°
ψ β 46°	*ψ b* 46°	48°	**61°**	90°
ψ γ 52°	*ψ c* 77°	69°	**70°**	61°

Figure 3.1-11. *Fragment of the crystal structure of diopside showing the direction of the hydrogen bond with the proton attached to the O2 oxygen atom and the OH dipole pointing to the O1 oxygen (mechanism 2). The end of the vector originating from O2 points towards the position of the proton. This is the mechanism responsible for Type II infrared spectra.*

3.1.1.4. Water solubility in diopside with excess silica

Based on the observation that spectra of Type I with only one absorption band at 3650 cm^{-1} may be an indicator of a Si vacancy in the *T* site or of some other tetrahedral defect, another series of synthesis experiments has been carried out using both the piston cylinder and multi-anvil apparatus. In order to avoid any contaminations, which may cause defects in the tetrahedral site (such as aluminum which may come from pyrophyllite capsule sleeves), MgO capsule sleeves have been used. The run conditions ranged from 20 to 100 kbar and from 700 to 1100°C. The run products were diopside and coesite, as in previous experiments (see Table 3.1-1). As an exception in run #77, which was performed at 30 kbar and 900°C diopside and coesite were observed, while in the previous experiment #4 (under the same conditions) diopside with olivine were found. Both

runs had infrared spectra of Type II with single absorption band at 3357 cm^{-1}. The run conditions, run products and calculated water content from infrared measurements are listed in Table 3.1-5. The presence of olivine in run #M9 may be due to some local inhomogenity of the starting material.

Table 3.1-5. *Experimental conditions, run products and average water content calculated from FTIR spectra of pure diopside crystals*

# exp.	Conditions		Water coming out of the capsule after experiment	Water loss from capsule after drying (%)**	Run products	*n* and type of spectra	Water content (ppm H$_2$O)	
	P (kbar)	T (ºC)					Paterson (1982)	Bell et al. (1995)
# M5	100	900	no	78	diopside, coesite^a	1 (p), II	108	121
# M7	80	900	no	74	diopside, coesite	1 (p), II	155	170
# M9	60	900	no	100	diopside, olivine^a	1 (p), II	225	242
# 77	30	900	no	82	diopside, coesite	1 (p), II	389	402
# 78	20	900	yes	54	diopside	1 (p), II	240	259
# 84	30	1100	yes	60	diopside, coesite	1 (p), II	370	408
# 83	30	1000	yes	68	diopside	1 (p), II	487	568
# 81	30	700	no	40	diopside, coesite	1 (p), II	229	248

* The starting material for diopside synthesis was with 10% excess of SiO$_2$ for each experiment

** in % of the total amount of water loaded, the starting amount of water for PC experiment was 0.034-0.037 g and for MA experiments – 0.0035 g.

n – number of measurements; (p) –data were calculated based on polarized measurements;

a – mineral was identified in run products by microprobe analyses.

All infrared spectra measured from pure diopside from these experiments show one main absorption band at 3357 cm^{-1}. Water contents were relatively small, in the order of several hundreds ppm H$_2$O. Water contents in pure diopside range from 121 ppm H$_2$O at 100 kbar and 900ºC to 568 ppm H$_2$O at 30 kbar and 1000ºC (see Table 3.1-5).

In most cases only two out of three polarized spectra could be measured. The water content in the third direction of the indicatrix was then reconstructed with the assumption that the ratios of the absorbances for the three directions are always the same for the same type of spectrum. The completed polarized spectra from diopside synthesized at 60 kbar and 900ºC are illustrated in

Figure 3.1-12. In this case, the amount of water measured parallel to the *β* indicatrix axis equals 47.5% of the total water content. For some other crystals from these experiments the following percentage was found: *α* 15-23%, *β* 44-48%, *γ* 33-37%. Spectra measured only parallel to the *β* indicatrix axis for each experiment are presented on Figure 3.1-13.
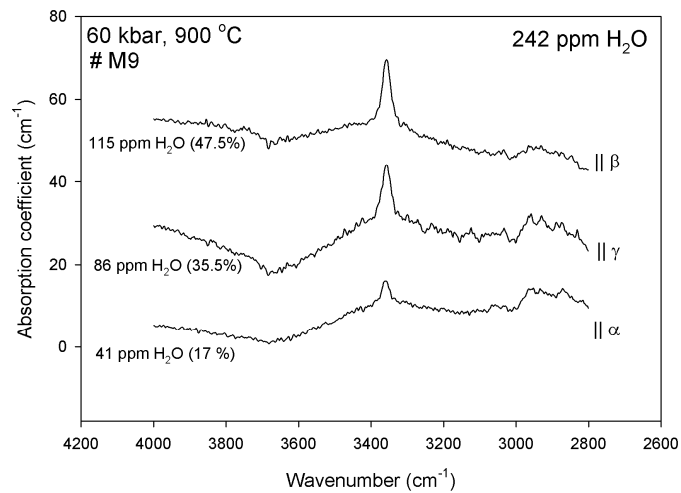
Figure 3.1-12. *Polarized infrared spectra of diopside synthesized at 60 kbar and 900°C. The water contents for spectra measured parallel to each indicatrix axis are given together with their percentage of the total amount.*

Figure 3.1-14 shows that water solubility at 30 kbar increases from 700 to 1000°C. Above 1000°C, it drops again. This drop may be related to an elevated concentration of silicate in the fluid, which reduces water activity. At 900°C, water solubility first increases with pressure up to 25 kbar and then decreases at higher pressures (Figure 3.1-15).
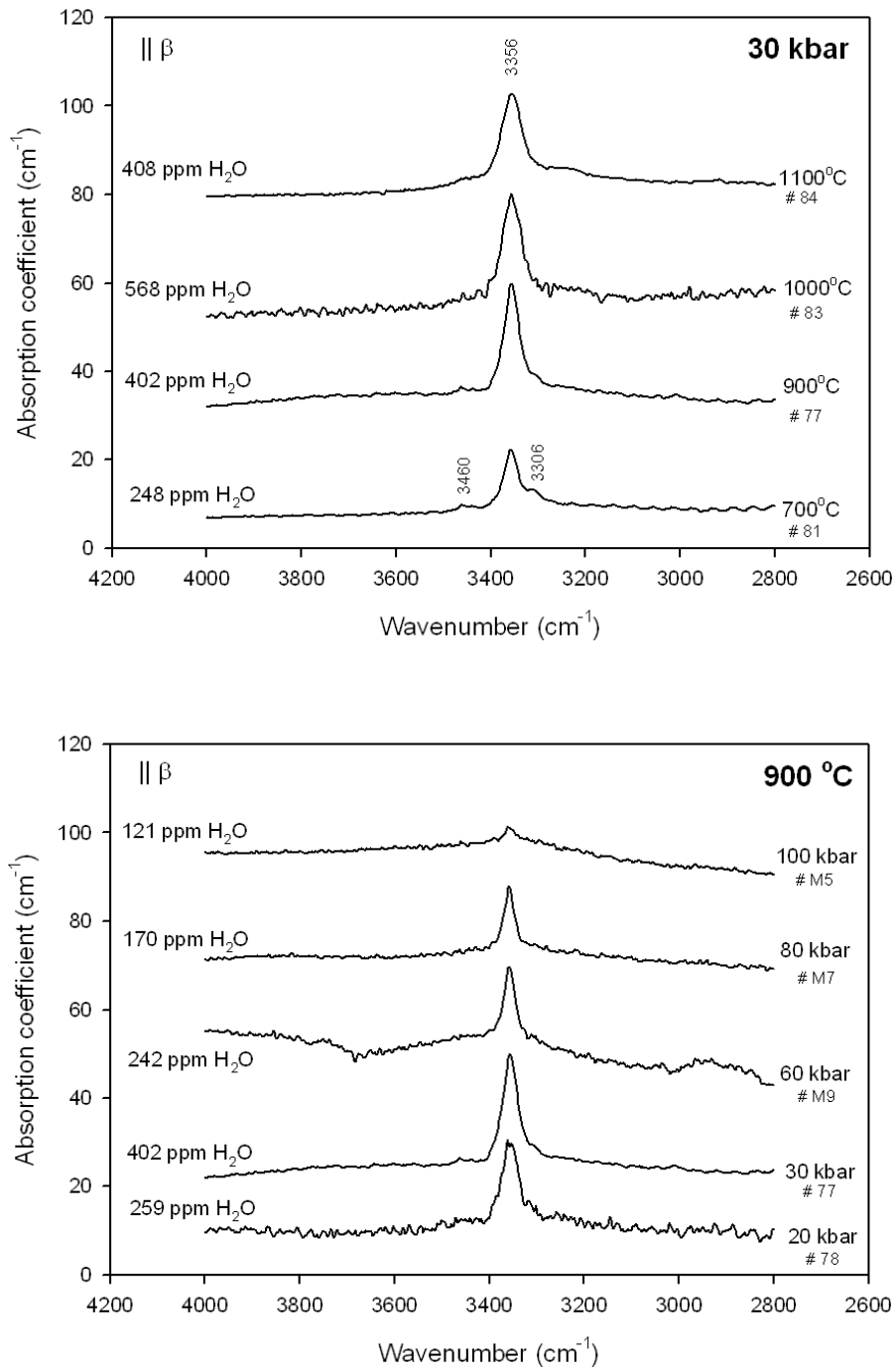
Figure 3.1-13. *Polarized infrared spectra of pure diopside synthesized at different conditions. The spectra presented at these plots were measured only parallel to one indicatrix axis β. Total amounts of water are given close to each spectrum.*
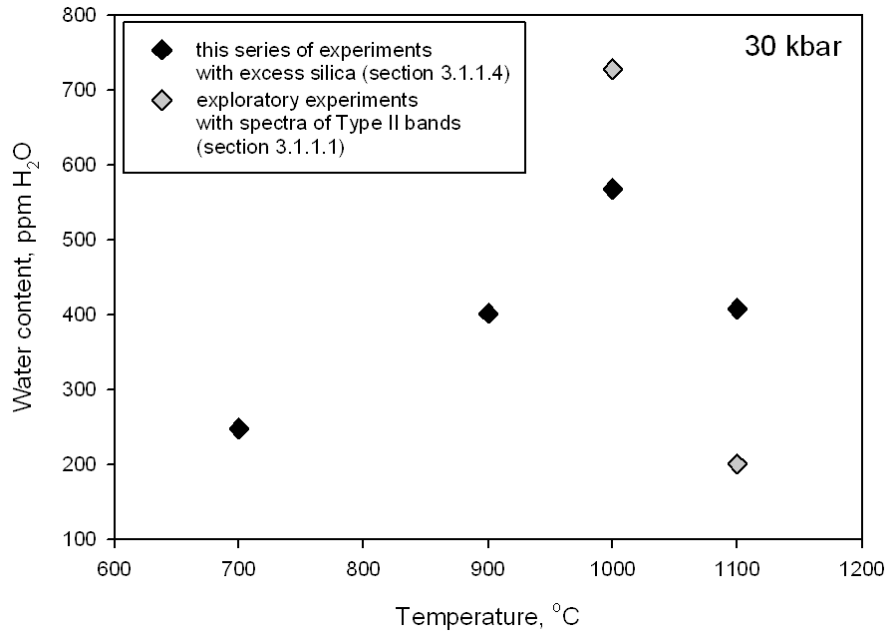
Figure 3.1-14. *Water solubility in diopside as a function of temperature at constant pressure of 30 kbar*
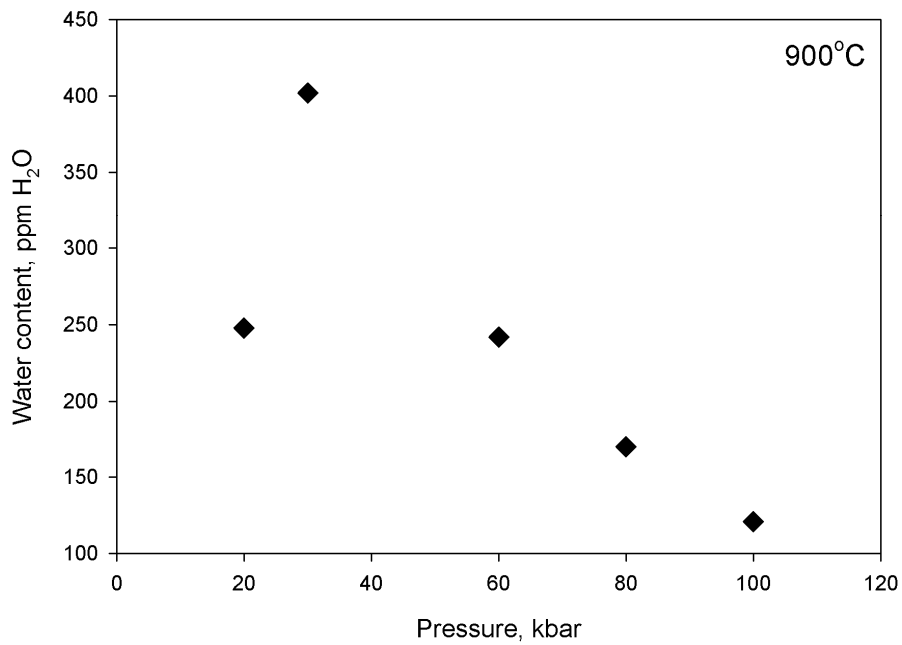
Figure 3.1-15. *Water solubility in diopside as a function of pressure at constant temperature of 900 ^{o}C*

3.1.1.5. Thermodynamic model of water solubility

Since all infrared spectra measured on diopside crystals from the last series of experiments show one dominant absorption band at 3357 cm^{-1} I propose a water dissolution mechanism as OH pair charge balanced by Mg^{2+} or Ca^{2+} vacancies. This may be written as:

$$H_2O + O = (OH)_2$$
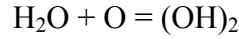
where "O" is some non-protonated oxygen atom.

The equilibrium constant for this reaction is:

$$K = \frac{a(OH)_2}{a_{H2O}a_O}$$

Since nearly pure water is in equilibrium with diopside, a_{H2O} may be assumed as 1. The activity of the non-protonated oxygen atoms a_O may be assumed to be constant. Therefore, K is directly proportional to the water content in ppm by weight.

K is related to standard state thermodynamic properties according to:

$$-RT \ln K = \Delta G = \Delta H^{1bar} - T \Delta S^{1bar} + \Delta V^{solid} (P - 1bar) - RT \ln (f/f_0)_{H2O}$$

where ΔH^{1bar} and ΔS^{1bar} are the reaction enthalpy and entropy at 1 bar,

ΔV^{solid} is volume change in the pyroxene upon water incorporation;

f_{H2O} is water fugacity;

T is temperature, in K;

P is pressure, in bars;

R is the gas constant

f_0 is by definition 1 bar, in the term (P-1bar) 1 bar can be neglected for the pressures considered . With these simplifications, the equation can be rearranged to:

$$C_{H2O} = A f_{H2O} \ exp(-\Delta H^{1bar} / RT) \ exp(-P\Delta V^{solid} / RT)$$

where C_{H2O} is water solubility, in ppm H$_2$O by weight;

A is a temperature-dependent constant;

A multiple regression fit of all data from Table 3.1-5 using water contents calculated with extinction coefficient calibration by Bell et al., (1995) yielded the following parameters:

$A = 0.0185\ (\pm 0.00174)$ ppm/bar

$\Delta H^{1bar} = -11117\ (\pm 994)$ J/mol

$\Delta V^{solid} = 14.62 \pm (0.59)$ cm^3/mol

The values for water fugacities were calculated using $RT\ln f(H_2O)$ (kJ/mol) dataset form Holland and Powell (1998). Figure 3.1-16 compares water contents calculated with the model to the measured data. In general, the agreement is quite good.
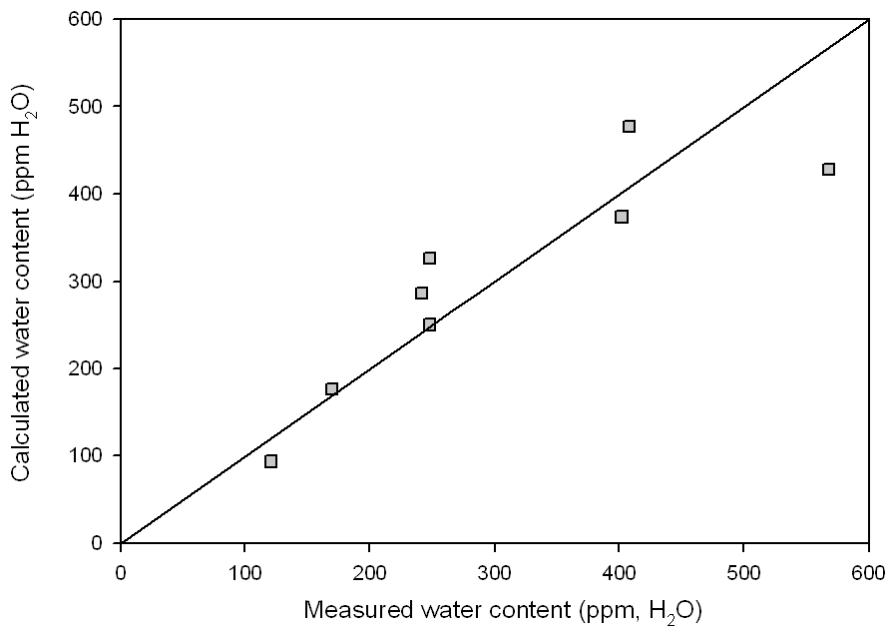
Figure 3.1-16. *Comparison of measured water solubilities in diopside and water solubilities predicted by the thermodynamic model*

3.1.2. Effect of Al on water solubility in diopside

3.1.2.1. Description of run products

Single crystals of Al-bearing diopside were synthesized in the piston-cylinder press at 15 and 25 kbar and 900-1100°C. The duration of each experiment was from 2.5 up to 3 days. The composition of starting materials lies along the join diopside (Di) – Ca-Tschermak's component (CaTs) with different ratios of these two end members (see section 2.1.1 for details). After each experiment, the capsule was checked for the presence of excess water (see Table 3.1-6).

Recovered samples were in the form of a colorless, crystalline mass with a small amount of clear inclusions-free single crystals of diopside, which were large enough for further investigations. The sizes of the diopside crystals usually reached up to 50-100 μm.

X-ray powder diffraction was used for phase identification after each experiment. The run product in most of the experiments were Al-bearing diopside only. In two runs some crystals of corundum were found by microprobe, but they were not detected in the diffraction pattern. In general the powder patterns consist only of diffraction peaks of diopside. A few weak diffraction peaks in some samples could not be unambiguously assigned. The diffraction pattern for run product #36 synthesized at 15 kbar and 1000°C showed one relatively strong peak which could not be identified (see Figure 3.1-17). The diffraction peaks of diopside in all samples were quite broad, which may reflect an inhomogeneous distribution of alumina in the diopside crystals.

Experimental details, run conditions and products as well as calculated water contents are listed in Table 3.1-6.

Chemical analyses of a few crystals from each experiment are presented in Appendix 2. Al contents in diopside were sometimes slightly inhomogeneous. The compositions of all Al-bearing diopsides measured are listed in Table 3.1-6. In general, the composition of the large crystals used for infrared analyses, was somewhat less aluminous than the starting material (Figure 3.1-18). Possibly, the smaller diopside crystals had higher alumina content or small amounts of alumina were present as a separate phase, e.g. corundum.
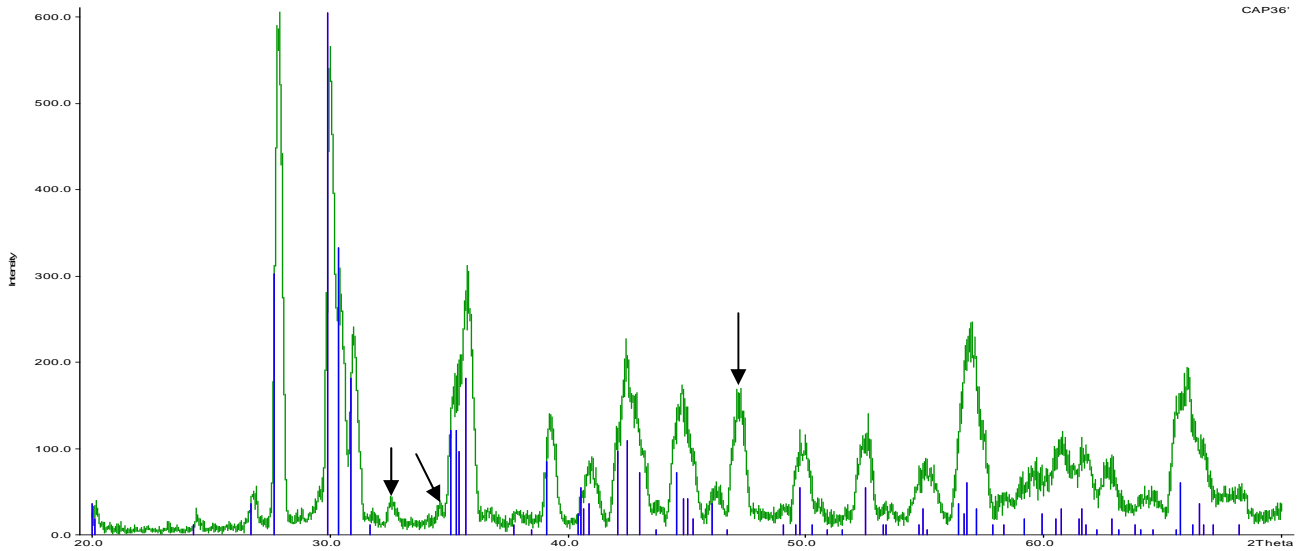
Figure 3.1-17. *Powder diffraction pattern (CuKα-radiation) of run # 36 synthesized at 15 kbar and 1000°C. All diffraction peaks (in blue) corresponding to pure diopside are assumed to shift to higher values of 2 Theta angles because of the presence of Al. Black arrows point to the peaks which were not identified.*
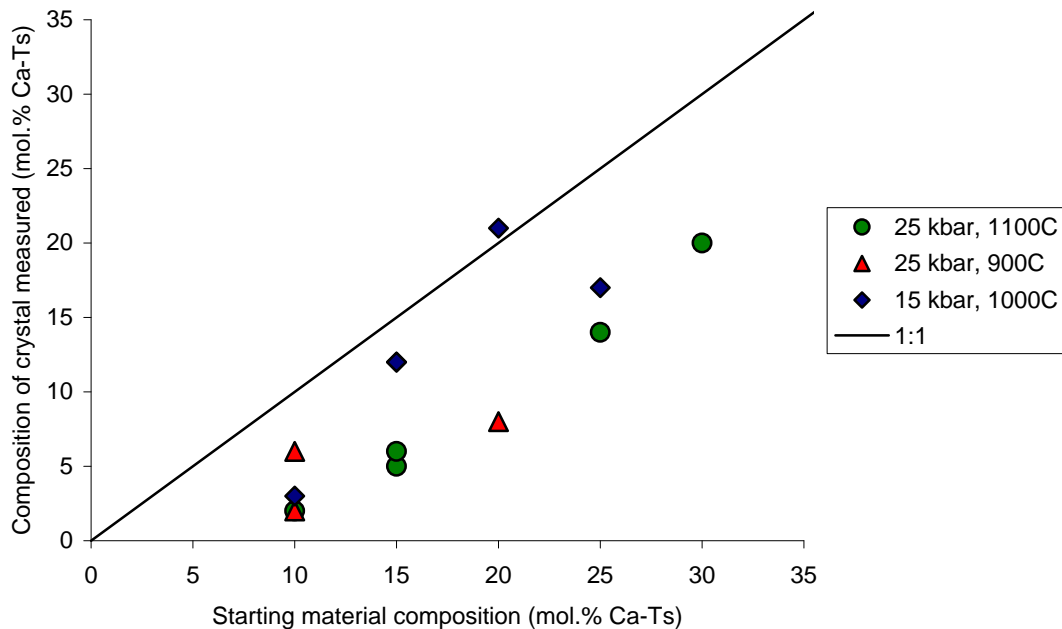
Figure 3.1-18. *Comparison of the measured composition of the single crystals with the bulk composition of the starting material, in mol. % of Ca-Tschermak's component*

Table 3.1-6. *Experimental details, run products and average water content calculated from FTIR spectra of Al-bearing diopside crystals*

# exp.	Conditions		Starting material	Resulting composition	Water coming out of the capsule after experiment	Water loss from capsule after drying (%)*	Run products	*n* and type of spectra	Water content (ppm H_2O)	
	P (kbar)	T (°C)							Paterson (1982)	Bell et al. (1995)
# 38	25	1100	$Di_{90}CaTs_{10}$	$Di_{98}CaTs_2$	no	46	Di	1 (p), I	504	573
# 40	25	1100	$Di_{85}CaTs_{15}$	$Di_{95}CaTs_5$	no	92	Di	1 (p), I	560	636
# 44	25	1100	$Di_{85}CaTs_{15}$	$Di_{94}CaTs_6$	no	70	Di	2 (p), I	798 ± 79	869 ± 83
# 47	25	1100	$Di_{75}CaTs_{25}$	$Di_{86}CaTs_{14}$	no	57	Di	2 (p), I	966 ± 99	1054 ± 119
# 49	25	1100	$Di_{70}CaTs_{30}$	$Di_{80}CaTs_{20}$	no	63	Di	2 (p), I	1865 ± 202	2591 ± 241
# 61	25	900	$Di_{90}CaTs_{10}$	$Di_{94}CaTs_6$	yes	53	Di	1 (p), I	1278	1722
# 63	25	900	$Di_{80}CaTs_{20}$	$Di_{92}CaTs_8$	no	73	Di	1 (p), I	1322	1995
# 66	25	900	$Di_{90}CaTs_{10}$	$Di_{98}CaTs_2$	no	48	Di	1 (p), I	651	825
# 28	15	1000	$Di_{90}CaTs_{10}$	$Di_{97}CaTs_3$	yes	73	Di	2 (p), I	833 ± 57	901 ± 98
# 32	15	1000	$Di_{85}CaTs_{15}$	$Di_{88}CaTs_{12}$	yes	24	Di, Crn	2 (p), I	955 ± 120	1181 ± 194
# 35	15	1000	$Di_{85}CaTs_{15}$	$Di_{88}CaTs_{12}$	yes	20	Di	2 (p), I	1220 ± 101	1797 ± 118
# 39	15	1000	$Di_{75}CaTs_{25}$	$Di_{83}CaTs_{17}$	yes	27	Di, Crn	2 (p), I	1776 ± 187	2060 ± 211
# 36	15	1000	$Di_{80}CaTs_{20}$	$Di_{79}CaTs_{21}$	yes	20	Di	2 (p), I	1641 ± 135	2510 ± 156

* the starting material was homogeneous for each experiment (H);

** in % of the total amount water loaded, the starting amount of water for PC experiment was 0.033-0.037 g;

n – number of measurements; (p) –data were calculated based on polarized measurements;

Di – Al-bearing diopside; Crn – corundum was analyzed by microprobe analyses in the form of single crystals.

3.1.2.2. Infrared spectra

All infrared spectra of the Al-containing diopside samples show one main absorption band at 3650 cm^{-1} (Type I spectra). Therefore, only one type of OH substitution mechanism dominates in aluminous diopside. For all experiments it was observed that water solubility strongly increases with Al content up to 2500 ppm H_2O. The lowest water content of 573 ppm H_2O was measured for run #38 synthesized at 25 kbar and 1100°C containing 1.54 wt.% of Al_2O_3. The highest water content was measured for run #49 synthesized at the same conditions of 25 kbar and 1100°C containing 8.37 wt.% of Al_2O_3. Calculated water contents for each experiment are listed in Table 3.1-6. Polarized infrared spectra measured parallel to the *β* indicatrix axis for each experiment are shown in Figure 3.1-19.
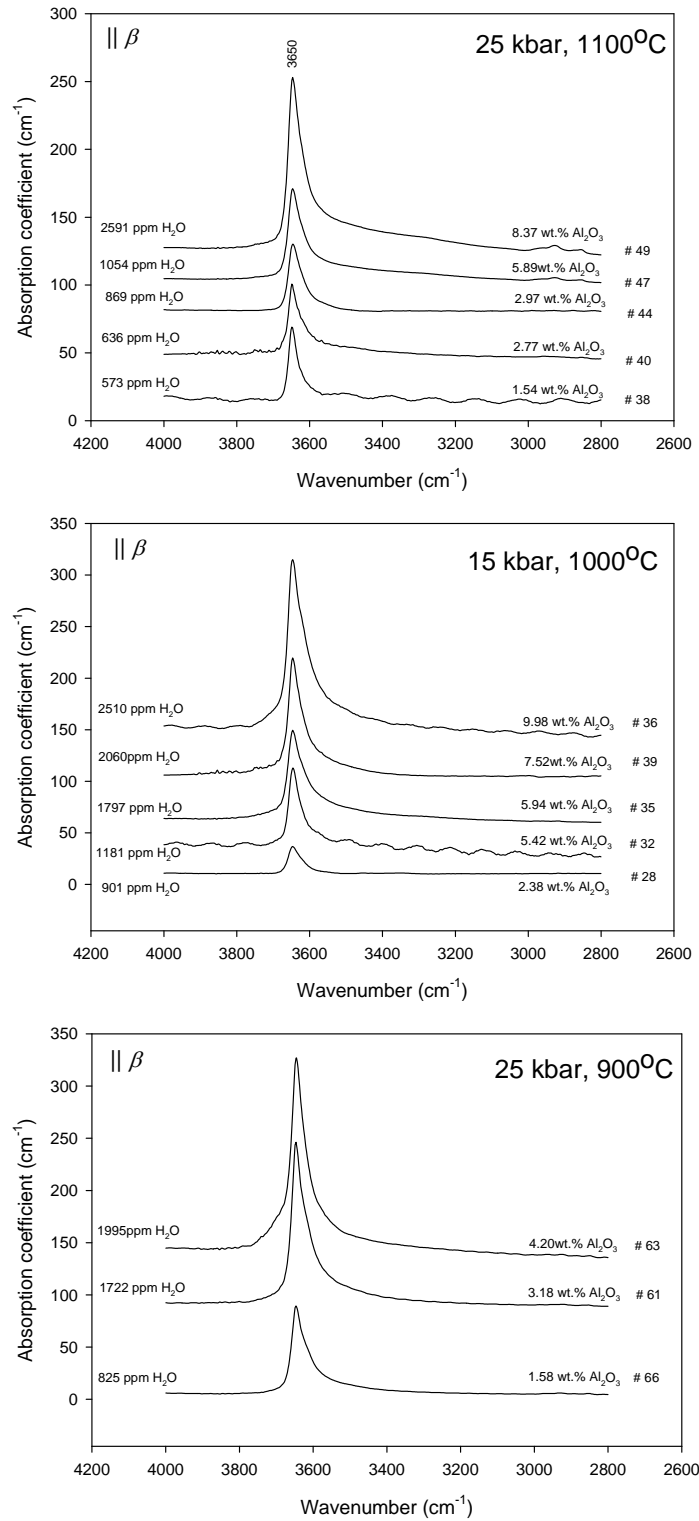
Figure 3.1-19. *Polarized infrared spectra of Al-bearing diopside synthesized at different conditions. The spectra presented here were measured parallel to the β axis of the indicatrix. Total amounts of water are given close to each spectrum as well as Al concentrations (in wt.%).*

For each experiment polarized infrared spectra were measured. There is only one strong absorption band at 3650 cm⁻¹ along all three indicatrix axes (Figure 3.1-20 A). The absorption band at this frequency is likely to be related to the defect in the Si site. For some experiments, additional weak absorption bands at 3360 and 3460 cm⁻¹ were observed in the spectra measured along the α indicatrix axis (see Figure 3.1-20 B). This observation suggests an additional, minor hydrogen incorporation mechanism in Al-bearing diopside. Absorption bands at 3360 and 3460 cm⁻¹ possibly indicate vacancies (or other defects) in the Mg (*M1*) and Ca (*M2*) crystallographic sites, respectively. All spectra show the same polarization behavior with the highest absorption in β direction, almost identical but slightly smaller absorption parallel γ, and the lowest absorption along the α axis of the indicatrix ($A_\beta \geq A_\gamma > A_\alpha$).
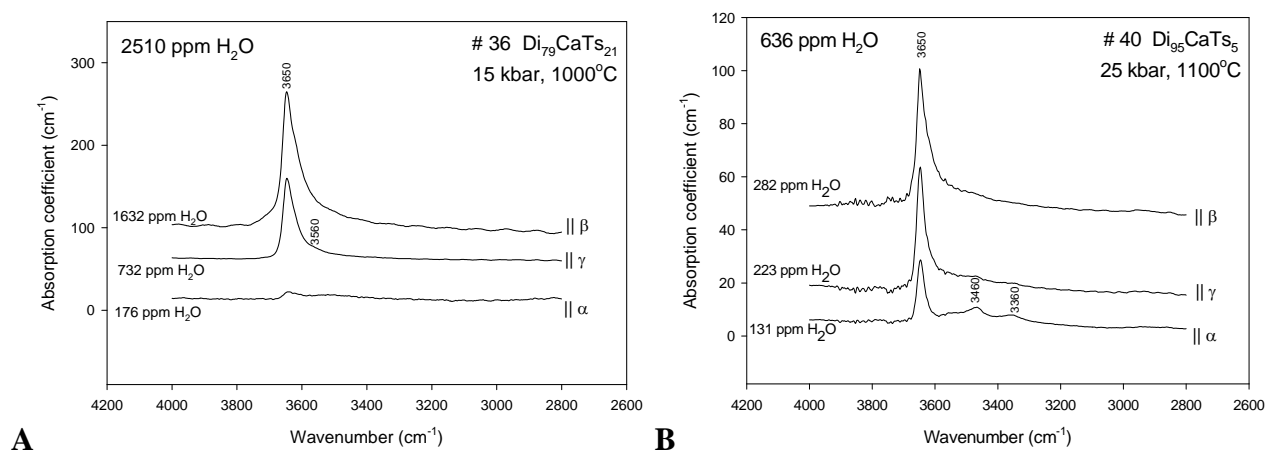
Figure 3.1-20. *Polarized infrared spectra with different orientation of the electrical field vector E for aluminous diopside crystals synthesized at 15 kbar, 1000°C (A) and at 25 kbar 1100°C (B)*

3.1.2.3. P-T dependence of water solubility

At all conditions studied, water solubility increases linearly with Al content (see Figure 3.1-21). Figure 3.1-21 show that water solubility in Al-bearing diopside increasing with decreasing temperature from 1100 to 900°C at 25 kbar. The effect of pressure on water solubility could not yet be unambiguously defined, since the experiments at 15 kbar were done at temperature different from the 25 kbar experiments (see Figure 3.1-22). The pressure effect appears to be rather small, however.
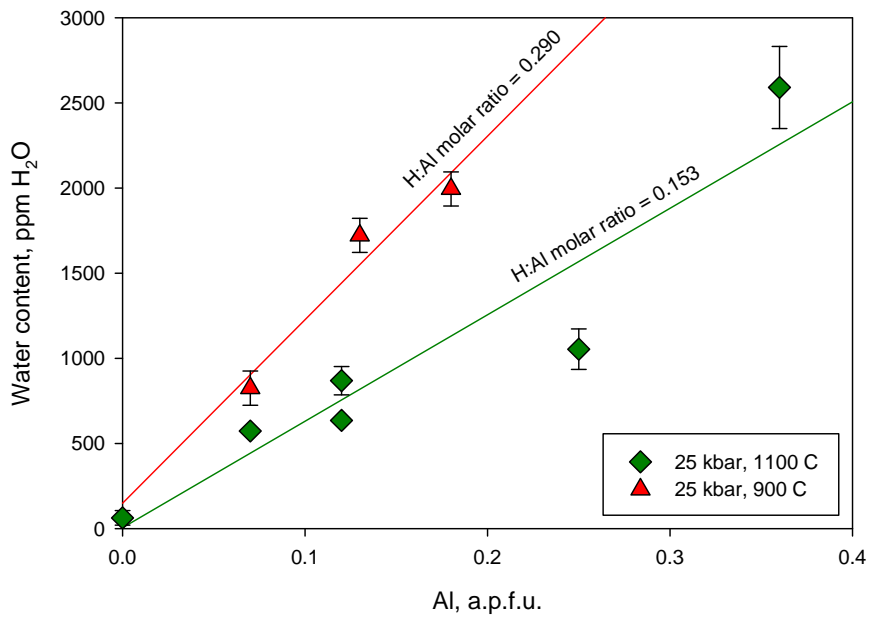
Figure 3.1-21. *Correlation between water content and Al concentration in diopside at 25 kbar and 1100 and 900°C. The plot shows that water solubility increases with decreasing temperature.*
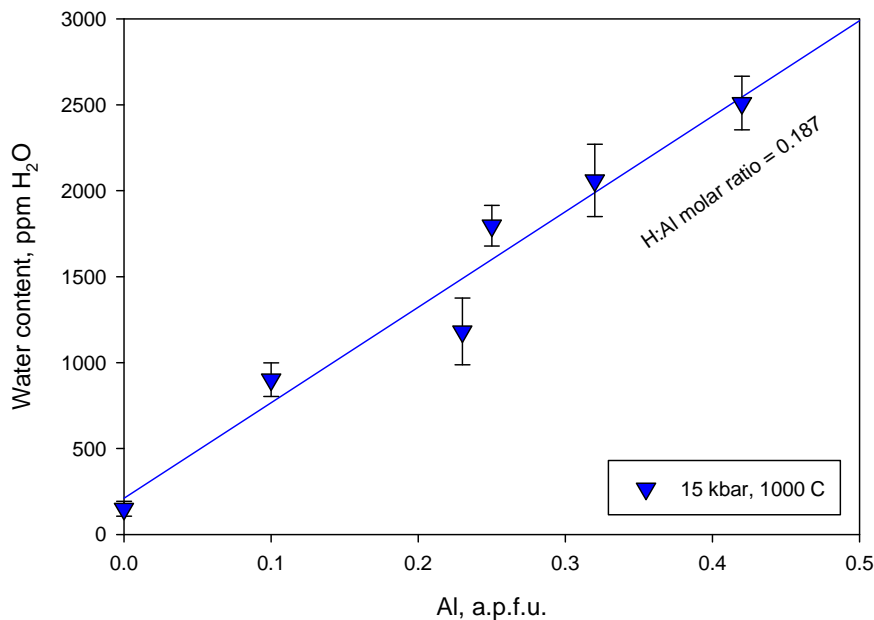
Figure 3.1-22. *Correlation between calculated water concentration and Al content for aluminous diopside synthesized at 15 kbar and 1000°C*

3.1.2.4. Hydrogen substitution mechanism

Ca-Tschermak's substitution mechanism in clinopyroxenes involves the coupled substitution of two Al^{3+} cations for Mg^{2+} and Si^{4+}, implying equal amounts of octahedral and tetrahedral Al^{3+}:

$$2Al^{2+} = Mg^{2+} + Si^{4+}$$

Under hydrous conditions two additional mechanisms are possible: $Al^{3+} + H^+ = Si^{4+}$ and $Al^{3+} + H^+ = 2Mg^{2+}$. Based on microprobe analyses the type of substitution mechanism may be established.

For the $Al^{3+} + H^+ = Si^{4+}$ substitution, the chemical composition would show a deficiency of Si in tetrahedral sites. The cation sum measured by microprobe would be > 4 (calculated for 6 oxygens).

The mechanism $Al^{3+} + H^+ = 2Mg^{2+}$ would cause a deficiency of Mg in octahedral sites. The cation sum from microprobe analyses would be < 4.

As an example, Figure 3.1-23 shows a correlation between Al concentration and deficiency of Si, Mg and Ca as well as the cation sum for aluminous diopside from the run #47 synthesized at 25 kbar and 1100°C. Solid lines correspond to Ca-Tschermak's substitution mechanism, dashed lines correspond to Al-H substituting for Si and dash-dotted lines to Al-H substituting for 2Mg. Therefore, these plots suggest a combination of Ca-Tschermak's substitution with the $Al^{3+}H^+$ substitution for Si^{4+}. This is consistent with the assignment of the 3650 cm^{-1} band to a defect involving the tetrahedral site. Deficiency of Ca in *M2* correlates with Mg concentration in *M1*. It is possible that some of Mg occupies the *M2* position as well.

The site occupancies from microprobe analyses can be directly checked for consistency with the proposed substitution mechanism. The clinopyroxenes may be described as solid solutions of the following three components:

$$CaMgSiSiO_6 \quad CaAlAlSiO_6 \quad CaMg(AlH)SiO_6$$

First, according to the water contents measured by infrared spectroscopy, the amount of H atoms (in a.p.f.u.) was calculated. From the molar ratio of Al:H the abundance of the three components $CaMgSi_2O_6$, $CaAl_2SiO_6$ and $CaMg(AlH)SiO_6$ was calculated, which directly yields the expected distribution of Al over tetrahedral and octahedral positions (see Table 3.1-7). The distribution of Al atoms among crystallographic sites was calculated independently from the microprobe analyses for all aluminous diopsides. Of the three samples in Table 3.1-7 with water

content above 2000 ppm, two show the excess of tetrahedral over octahedral Al, while in one sample Al appears to be equally distributed over tetrahedral and octahedral sites. For the samples with lower water content, the effects are possibly too small to be detected beyond analytical uncertainty.
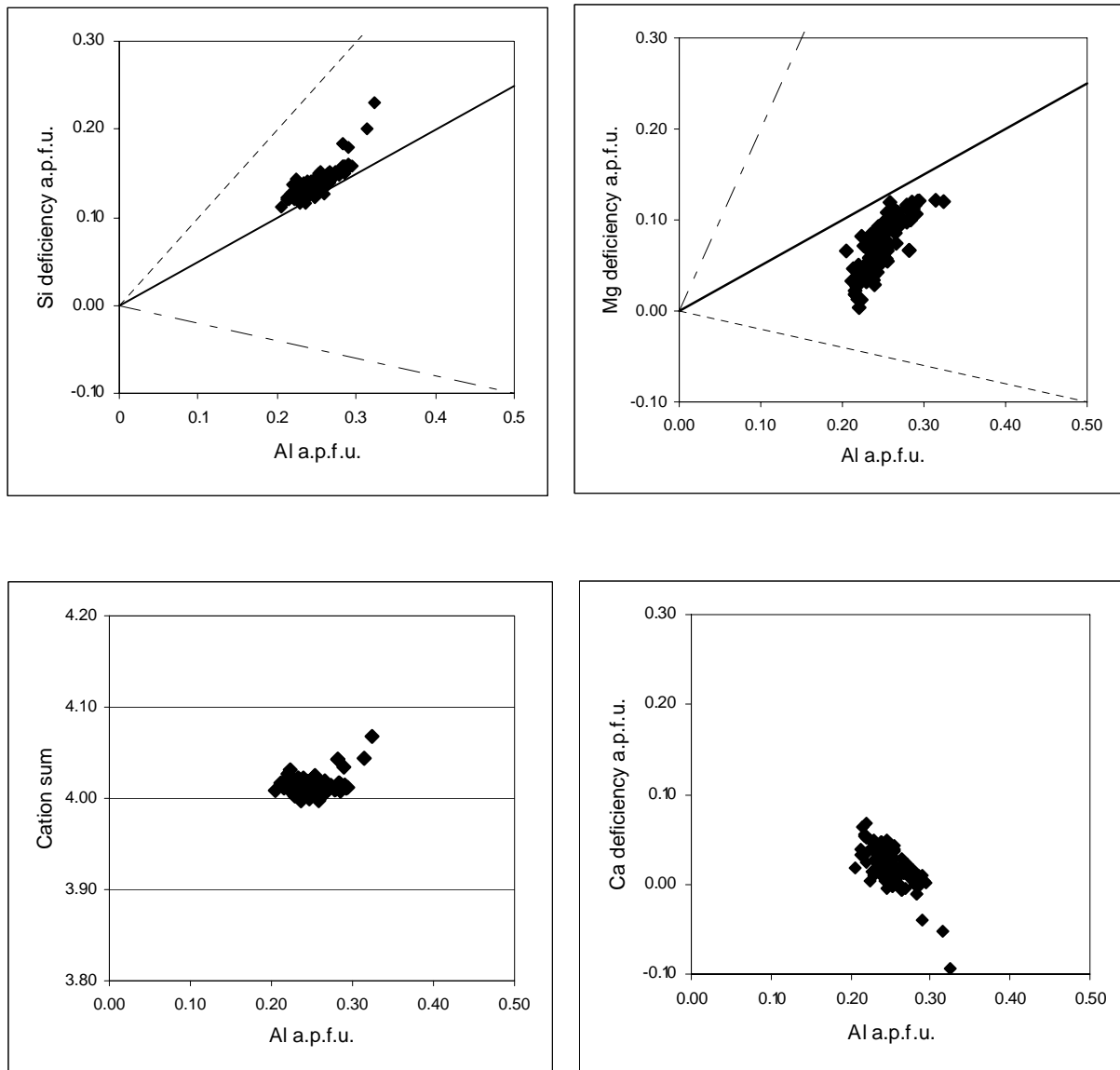
Figure 3.1-23. *Influence of substitution mechanism on microprobe analyses for aluminous diopside from experiment # 47 at 25 kbar and 1100°C. Solid lines on the two upper plots correspond to Ca-Tschermak's substitution mechanism, dashed lines correspond $Al^{3+} + H^{+} = Si^{4+}$ and dash-dotted lines to $Al^{3+} + H^{+} = 2Mg^{2+}$.*

Table 3.1-7. *Chemical analyses of aluminous diopside (in a.p.f.u). Concentrations of H atoms were calculated from infrared measurements. The distribution of Al among crystallographic positions in aluminous diopside (in a.p.f.u) was calculated with the assumption that tetrahedral sites are completely filled.*

run	T (°C)	P (kbar)	H₂O (ppm)	Si	Al	Mg	Ca	Cation sum	H	H:Al molar ratio	predicted from water measurements Al in T	predicted from water measurements Al in M1	calculated from microprobe analyses Al in T	calculated from microprobe analyses Al in M1
# 28	1000	15	901	1.97 ± 0.02	0.10 ± 0.04	1.04 ± 0.02	0.88 ± 0.04	3.99 ± 0.02	0.021	0.214	0.06	0.04	0.03	0.07
# 32	1000	15	1181	1.88 ± 0.02	0.23 ± 0.03	0.94 ± 0.03	0.96 ± 0.03	4.01 ± 0.01	0.028	0.123	0.13	0.10	0.12	0.11
# 35	1000	15	1797	1.88 ± 0.02	0.25 ± 0.03	0.92 ± 0.02	0.96 ± 0.01	4.00 ± 0.01	0.042	0.171	0.15	0.10	0.12	0.13
# 39	1000	15	2060	1.83 ± 0.04	0.32 ± 0.07	0.87 ± 0.03	1.0 ± 0.01	4.01 ± 0.01	0.050	0.155	0.18	0.14	0.17	0.15
# 36	1000	15	2510	1.79 ± 0.02	0.42 ± 0.03	0.83 ± 0.02	0.97 ± 0.01	4.00 ± 0.01	0.060	0.142	0.24	0.18	0.21	0.21
# 61	900	25	1722	1.94 ± 0.06	0.13 ± 0.02	0.98 ± 0.05	0.95 ± 0.04	4.00 ± 0.03	0.041	0.306	0.09	0.05	0.06	0.07
# 63	900	25	1995	1.92 ± 0.02	0.18 ± 0.03	0.94 ± 0.02	0.96 ± 0.01	4.00 ± 0.02	0.047	0.269	0.11	0.06	0.08	0.10
# 66	900	25	825	1.98 ± 0.01	0.07 ± 0.01	1.05 ± 0.01	0.89 ± 0.01	3.99 ± 0.01	0.020	0.296	0.04	0.02	0.02	0.05
# 38	1100	25	573	1.98 ± 0.01	0.07 ± 0.02	1.05 ± 0.02	0.89 ± 0.02	3.99 ± 0.03	0.014	0.211	0.04	0.03	0.02	0.05
# 40	1100	25	636	1.95 ± 0.02	0.12 ± 0.01	0.98 ± 0.04	0.95 ± 0.02	4.00 ± 0.02	0.015	0.130	0.06	0.05	0.05	0.07
# 44	1100	25	869	1.94 ± 0.01	0.12 ± 0.01	0.98 ± 0.02	0.95 ± 0.02	3.99 ± 0.01	0.021	0.166	0.07	0.05	0.06	0.06
# 47	1100	25	1054	1.86 ± 0.02	0.25 ± 0.04	0.93 ± 0.03	0.98 ± 0.02	4.01 ± 0.03	0.025	0.101	0.14	0.11	0.14	0.11
# 49	1100	25	2591	1.80 ± 0.06	0.36 ± 0.07	0.87 ± 0.03	0.99 ± 0.01	4.02 ± 0.05	0.062	0.175	0.21	0.15	0.20	0.16

Therefore, both infrared spectra and accurate analyses of the microprobe data of aluminous diopside suggest that the coupled substitution $Al^{3+} + H^+ = Si^{4+}$ is the major mechanism for water dissolution in aluminous diopside.

3.1.2.5. Orientation of the hydroxyl group in aluminous diopside

The procedure for determining the proton location and the direction of the O-H dipole was exactly the same as for pure diopside and is described in detail in section 3.1.1.3.

Based on polarized infrared spectra (see Figure 3.1-20 A for run #36) the O-H dipole is inclined at: 66° to the crystallographic *a*-axis, 39° to the *b*-axis and 69° to the *c*-axis. For the observed O-H stretching frequency of 3650 cm^{-1} the expected oxygen-oxygen bond length is ~3.0-3.4 Å (see Figure 3.1-7 left).

Using these angles, orientation vectors [*u,v,w*] of the O-H group were calculated. These vectors starting from the O2 oxygen and pointing to the approximate location of hydrogen atom are shown on Figure 3.1-24. According to the three types of mechanisms proposed by Bromiley et al. (2004) and two additional possibilities (see Figure 3.1-24) the angles between O-O bonds and the *a, b* and *c* axes were calculated from the crystal structure of diopside. Table 3.1-8 presents calculated angles only for three major mechanisms (Bromiley et al., 2004) because the two other ones strongly deviated from the OH dipole direction. Comparison of the angles inferred from polarized infrared spectra and the angles calculated from the crystal structure of aluminous diopside (see Table 3.1-8) shows that the most likely mechanism of hydrogen incorporation is the mechanism 1 proposed by Bromiley et al. (2004). Moreover, a second type of incorporation mechanism may be considered with the OH- dipole orientated along the shared *M1-M2* edge. However, this is unlikely, for two reasons. This mechanism would rather correspond to a Mg-vacancy in *M1* and the O-O distance is quite short for the given frequency. Even for a coupled substitution such as $2Mg^{2+} = Al^{3+} + H^+$ the proton is unlikely to be located inside the *M1* site.

Therefore, polarized infrared spectra of Al-bearing diopside suggest incorporation of hydrogen onto the O2 oxygen with the O-H dipole pointing to the O3 oxygen atom (mechanism 1) corresponding to a hydrogen bond length O2-H…O3 of 3.042 Å (see Figure 3.1-25).

Table 3.1-8. *Measured and calculated angles between possible OH dipole directions and the monoclinic lattice axes in the aluminous diopside structure*

Measured angles (obtained from polarized infrared measurements)		Calculated angles for different O-O directions		
		1. along *M2* edge **O2-O3 with 3.042 Å**	2. along *M1-M2* edge O2-O1 with 2.942 Å	3. along *M1* edge O2-O2 with 2.979 Å
ψ α 79°	*ψ a* 66°	**58°**	47°	13°
ψ β 39°	*ψ b* 39°	**48°**	61°	90°
ψ γ 53°	*ψ c* 69°	**70°**	70°	61°

Figure 3.1-24. *Fragment of the crystal structure of aluminous diopside. Possible positions of the hydrogen atom and the direction of the hydrogen bond as determined from polarized infrared spectra (green and blue vectors). Dashed O-O bonds with their lengths (in Å) show different possibilities for the location of the OH dipole direction.*
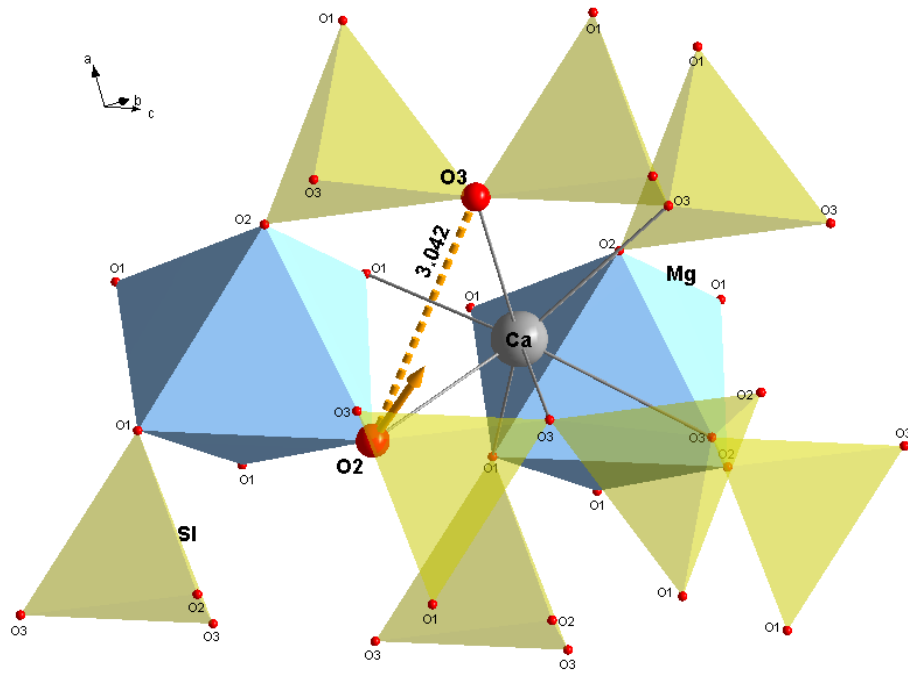
Figure 3.1-25. *Fragment of the crystal structure of aluminous diopside showing the direction of the hydrogen bond when a proton is attached to the O2 oxygen and the OH dipole points to the O3 oxygen (mechanism 1). The end of the vector originating from the O2 atom points towards the position of the proton.*

3.2. Effect of water on the equation of state of diopside

This part of the work focused on the effect of water on the elastic behavior of diopside. In order to determine the equation of state of diopsides, with different H_2O contents, high-pressure single crystal X-ray diffraction experiments have been performed.

3.2.1. Sample description

Diopside crystals containing different amounts of H_2O and Al were synthesized in the piston cylinder apparatus (cpx_1, cpx_2 and cpx_3). The synthesis procedure, capsule preparation and piston cylinder technique are described in detail in Chapter 2 (sections 2.1.2 and 2.1.3). The cpx_4 pure diopside crystal was synthesized at ambient pressure in a Pt crucible. First, the starting material was heated in a furnace to 1000^oC for one day to remove all volatiles. After this, the sample was melted at 1600^oC and then slowly cooled to 1000^oC within 24 hours. Starting materials for the crystals cpx_1, cpx_2 and cpx_4 were prepared according to the following reaction with a slight excess of silica: $Ca(OH)_2+Mg(OH)_2+2SiO_2 = CaMgSi_2O_6+2H_2O$. The starting material for the crystal cpx_3 was chosen along the join diopside ($CaMgSi_2O_6$) – Ca-Tschermak's component with composition of Di_{80}-$CaTs_{20}$. The details of synthesis for the four crystals are presented in Table 3.2-1.

Table 3.2.-1. *Experimental conditions of synthesis of diopside single crystals used for this study*

	# exp.	Starting material	P, kbar	T, ^oC	Duration, h	Run products	Presence of fluid after run	Water loss after experiment
cpx_1	# 17	Di 10% excess SiO_2	25	1100	72	diopside	yes	65%
cpx_2	# 21	Di 10% excess SiO_2	30	900	72	diopside, coesite	no	66%
cpx_3	# 36	Di80-CaTs20	15	900	72	diopside	yes	20%
cpx_4	# dd	Di 10% excess SiO_2	ambient	cooled from 1600^oC	24	diopside	no	-

Idiomorphic single crystals of diopside were selected by careful observation under an optical microscope. The crystals were further selected for high-pressure X-ray diffraction experiments by checking the reflection intensity and peak profiles using both the Xcalibur and Huber single-crystal diffractometers. The operating conditions and details for both diffractometers are presented in Chapter 2 (section 2.1.4.4 and 2.2.2).

The chemical compositions of the four diopside crystals were measured after the high-pressure X-ray single-crystal diffraction experiments, on the recovered crystals from diamond-anvil cells. A JEOL JXA-8200 electron microprobe was used. The details of measurement and standards are described in Chapter 2 (section 2.1.4.1). The measured chemical compositions are tabulated in Table 3.2-2.

Table 3.2-2. *The compositions of diopside single crystals (in wt. % oxide and cation proportion) used for the high-pressure X-ray diffraction experiments (left table). Cation proportions are calculated based on 6 oxygen atoms per formula unit. Cation occupancies (in a.p.f.u.) from microprobe analysis are listed in the right table. Water contents were calculated from the infrared measurements.*

	cpx_1	cpx_2	cpx_3	cpx_4
Al_2O_3	0.088	0.059	8.813	0.030
MgO	19.379	18.635	15.774	20.061
CaO	25.246	25.479	25.443	23.805
SiO_2	56.626	55.546	49.774	55.809
H_2O (wt.%)	0.006	0.060	0.251	0
Total	101.345	99.779	99.055	99.705
Al	0.004	0.003	0.374	0.001
Mg	1.040	1.000	0.846	1.073
Ca	0.973	0.982	0.981	0.916
Si	2.038	2.000	1.791	2.004
H^+	0.001	0.014	0.060	0
Total	4.056	3.983	3.991	3.995

		cpx_1	cpx_2	cpx_3	cpx_4
2T	Si	2.038	2.000	1.791	2.004
	Al	-	-	0.209	-
M1	Mg	1.000	1.000	0.835	1.000
	Al	-	-	0.165	-
M2	Ca	0.973	0.982	0.981	0.916
	Mg	0.040	-	0.011	0.073

The cation distribution among the structural positions (tetrahedral – *T*, octahedral – *M1*, 8-coordinated – *M2*) was calculated from the microprobe analyses (see Table 3.2-2 right). A general description of the crystal structure of diopside is given in Chapter 1 (section 1.3.1) and in more detail in the structural refinement section 3.3 of this chapter. Because of the uncertainties of the chemical analyses, the real cation distribution may slightly deviate from the calculated values. The tetrahedral position (*T*) is occupied only by Si in the cpx_1, cpx_2 and cpx_4 structures and by Si plus Al in the cpx_3 structure. The octahedra (*M1*) in cpx_1, cpx_2 and cpx_4 contain only Mg cations, but in cpx_3 diopside they contain Mg together with Al cations. For all four crystals the large *M2* position is mainly occupied by Ca, although some Mg may also be present at this site (see structural refinement section 3.3). The concentrations of protons, presented in Table 3.2-2 (left) were calculated from the infrared measurements.

The water content of the crystals was measured after they were recovered from the diamond anvil cells, i.e. after high-pressure X-ray diffraction experiments. First, the crystals were oriented parallel to the *(010)*, *(100)*, *(001)* and *(010)* crystallographic planes of the crystals cpx_1, cpx_2, cpx_3 and cpx_4 respectively. After the crystals were doubly polished, the Fourier-transform infrared spectrometer, which is described in detail in section 2.1.4.2, was used for the polarized measurements. Since the crystals could be polished parallel to only one crystallographic plane, only two from all three polarized infrared spectra could be measured (see Figure 3.2-1). In order to obtain the total water content for the diopsides the following calculation was applied. First, the complete set of polarized infrared spectra in three orientations for crystals from the same synthesis experiment were collected. The ratio of intensities of the absorption bands from the complete measurements were calculated. With the assumption that this ratio is the same for all crystals from the same experiment the total water content for each crystal was the calculated from the available polarized spectra (Table 3.2-2).
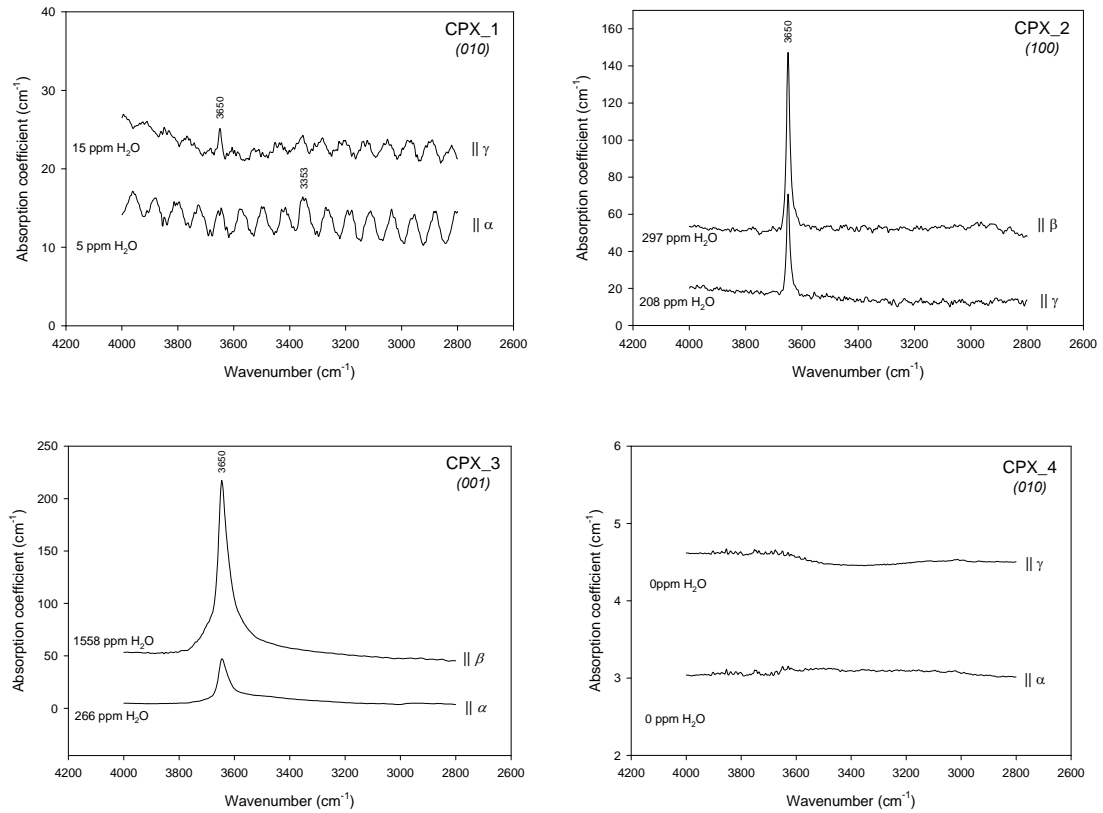
Figure 3.2-1. *Polarized infrared spectra of four diopside single crystals used in high-pressure X-ray diffraction experiments. The water contents refer to the amount of water detected in the respective polarized spectra. For total water contents see Table 3.2-2.*
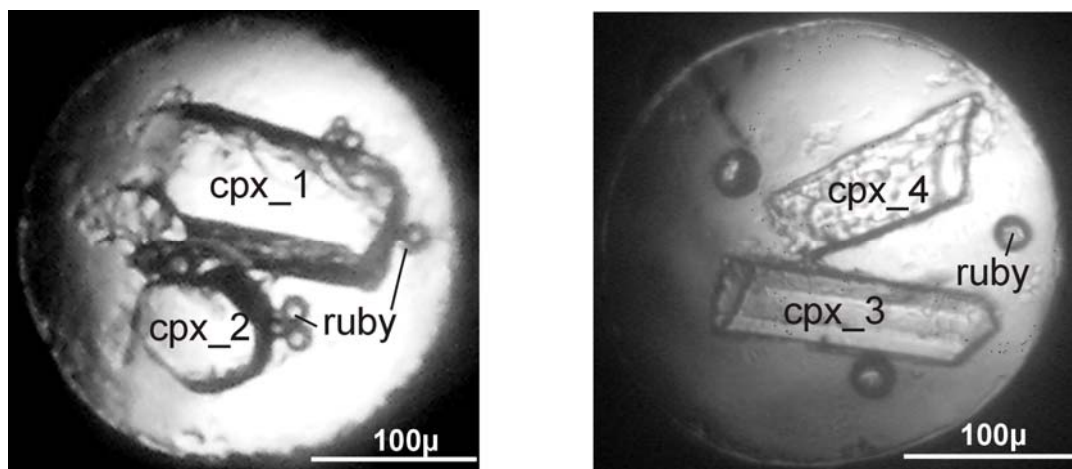
Figure 3.2-2. *The diopside single crystals loaded in diamond anvil-cell together with ruby chips*

Two separate high-pressure X-ray single-crystal diffraction experiments have been performed. For the first one, two single crystals of pure diopside with different water content (cpx_1 and cpx_2) were loaded in a diamond anvil-cell with a methanol-ethanol mixture as pressure medium together with ruby chips as internal pressure standard (Fig. 3.2-2 left). Two other crystals with different water and aluminum content (cpx_3 and cpx_4) were loaded in the second diamond anvil-cell in the same way (Fig. 3.2-2 right). The dimensions of the crystals were the following: 155 x 73 x 48μm (cpx_1); 85 x 68 x 50μm (cpx_2); 175 x 63 x 50μm (cpx_3); 154 x 70 x 50 μm (cpx_4).

3.2.2. Equation of state and compressibility

3.2.2.1. Theory of equation of state

In general, the equation of state (EoS) is a thermodynamic equation describing the state of matter under a given set of physical conditions. For example, the well-known EoS for ideal gases is the following:

$$PV = RT$$

For solids, the effect of temperature is much smaller than for gases. Therefore, the *isothermal* EoS is usually introduced. In Earth's sciences the isothermal EoS for minerals at high pressure is often measured. The theory of equations of state is further discussed in Angel (2000) and Poirier (2000).

The variations of the volume of a solid with pressure are characterized by the bulk modulus, defined as:
$$K = -\frac{V\partial P}{\partial V} = -\frac{dP}{d\ln V} = \frac{dP}{d\ln \rho}$$

Measured EoS are usually parameterized in terms of the values of the bulk modulus and its

pressure derivatives: $\qquad K' = \dfrac{\partial K}{\partial P} \qquad$ and $\qquad K'' = \dfrac{\partial^2 K}{\partial P^2}$.

The parameters K_0, K'_0 and K''_0 are these parameters at zero pressure.

Murnaghan EoS

The Murnaghan EoS can be derived from assumption that the bulk modulus varies linearly with pressure. This gives the following relationship between *P* and *V*:

$$V = V_0 \left(1 + \frac{K'P}{K_0}\right)^{-1/K'}$$

or:

$$P = \frac{K_0}{K'}\left[\left(\frac{V_0}{V}\right)^{K'} - 1\right]$$

Birch-Murnaghan EoS

Finite strain EoS are based upon the assumption that the strain energy (F) of a solid under compression can be expressed as polynomial expansion of the finite strain f.

$$F = a(T)f_E{}^2 + b(T)f_E{}^3 + c(T)f_E{}^4 + ...$$

The finite strain is defined by the change in distance between two neighboring points during deformation. There are a number of alternative definitions of f, each of which leads to a different relationship between P and V. The Birch-Murnaghan EoS is based upon the Eulerian strain:

$$f_E = \left[\left(\frac{V_0}{V}\right)^{2/3} - 1\right]/2 \qquad \text{or} \qquad \frac{V_0}{V} = (1 + 2f_E)^{3/2}$$

Strain energy F may be expanded to third order in finite strain f, then pressure is defined by the Birch-Murnaghan EoS:

$$P = 3K_0 f_E (1 + 2f_E)^{5/2}\left(1 + \frac{3}{2}(K'-4)f_E + \frac{3}{2}\left(K_0K''+(K'-4)(K'-3)+\frac{35}{9}\right)f_E{}^2\right)$$

If this equation is truncated to second order, which mean that the first pressure derivative K' is fixed to 4, the EoS yields the following expression: $P = 3K_0 f_E (1 + 2f_E)^{5/2}$.

The third-order truncation yields a three-parameter (V_o, K_o, K') EoS:

$$P = 3K_0 f_E (1 + 2f_E)^{5/2}\left(1 + \frac{3}{2}(K'-4)f_E\right)$$

3.2.2.2. High-pressure single-crystal X-ray diffraction

In order to obtain the equation of state of diopside, the unit-cell parameters were measured by X-ray diffraction at ambient temperature and at various pressures up to 9.6 GPa (for crystals cpx_1 and cpx_2) and up to 8.3 GPa (for crystals cpx_3 and cpx_4) using a four-circles Huber diffractometer (non-monochromatised MoK_α radiation). The maximum pressure of both experiments was constrained by the point where the gasket started to fail and diffraction lines appeared broadened. The variations of unit-cell parameters of the four different diopside crystals as a function of pressure are presented in Table 3.2-3 and Figure 3.2-3. The relative volume (V/V_o) plotted against pressure is the volume normalized to the ambient pressure volume. The relative parameters (a/a_o, b/b_o, c/c_o) as well as β angle (β/β_o) are these parameters normalized to the ambient pressure ones.

The volume change with increasing pressure is slightly different for the four crystals. Pure dry diopside cpx_4 is more compressible than the other samples. The pure diopsides cpx_1 and cpx_2 containing different amount of water are less compressible. However, the Al-bearing hydrous cpx_3 diopside is the stiffest one among the four diopside crystals from this study.

The axial compressibility of a/a_o, b/b_o, c/c_o of all the four crystals as a function of pressure is also shown on Figure 3.2-3. The axial compression is anisotropic with the *b*-axis being most compressible. The compressibilities of the *a*- and *c*-axes are almost identical. These results are similar to those for diopside (Tribaudino et al., 2000; Zhang et al., 1997; Levien and Prewitt, 1981) and hedenbergite (Zhang et al. 1997) and other clinopyroxenes (Nestola et al., 2005)

The angles β change slightly differently for each diopside crystal. The change in β is largest for cpx_4.

Table 3.2-3. *Unit-cell parameters of the four diopside single crystals measured at different pressures*

Cpx_1

Pressure, GPa		a_1, Å	b_1, Å	c_1, Å	β_1, °	V_1, Å^3
P0	0	9.7494(2)	8.9235(4)	5.2514(2)	105.909(2)	439.36(3)
P1	0.45	9.7364(2)	8.9089(4)	5.2442(2)	105.841(2)	437.62(3)
P2	1.53	9.7061(2)	8.8751(4)	5.2281(2)	105.694(2)	433.57(2)
P3	1.76	9.6992(2)	8.8673(5)	5.2243(2)	105.666(2)	432.63(3)
P4	2.18	9.6882(2)	8.8535(5)	5.2177(2)	105.612(3)	431.03(3)
P5	2.64	9.6781(2)	8.8421(4)	5.2124(3)	105.568(3)	429.69(3)
P6	3.20	9.6616(4)	8.8227(7)	5.2031(3)	105.495(4)	427.40(4)
P7	3.81	9.6483(2)	8.8065(4)	5.1959(2)	105.443(2)	425.55(3)
P8	4.54	9.6313(3)	8.7855(5)	5.1860(3)	105.376(3)	423.11(3)
P9	5.10	9.6186(2)	8.7705(3)	5.1792(2)	105.332(2)	421.37(2)
P10	6.02	9.6003(2)	8.7480(4)	5.1687(2)	105.259(2)	418.79(3)
P11	6.69	9.5848(7)	8.730(1)	5.1599(8)	105.211(8)	416.61(9)
P12	7.76	9.5672(2)	8.7056(3)	5.1502(2)	105.149(2)	414.05(2)
P13	8.74	9.5478(2)	8.6802(5)	5.1387(4)	105.089(3)	411.20(4)
P14	9.33	9.5395(5)	8.6705(9)	5.1343(7)	105.071(6)	410.06(7)
P15	9.58	9.5337(4)	8.6616(9)	5.1304(7)	105.042(5)	409.14(7)

Cpx_2

Pressure, GPa		a_2, Å	b_2, Å	c_2, Å	β_2, °	V_2, Å^3
P0	0	9.7534(4)	8.9249(1)	5.2548(1)	105.823(4)	440.09(3)
P1	0.45	9.7408(3)	8.9098(2)	5.2476(2)	105.769(3)	438.29(2)
P2	1.53	9.711(4)	8.8769(1)	5.2316(2)	105.632(4)	434.30(2)
P3	1.76	9.7039(6)	8.8689(2)	5.2274(3)	105.607(6)	433.29(4)
P4	2.18	9.6926(3)	8.8555(1)	5.2218(1)	105.561(3)	431.77(2)
P5	2.64	9.6833(3)	8.8444(1)	5.2167(1)	105.515(4)	430.49(2)
P6	3.20	9.6677(4)	8.8258(2)	5.2079(2)	105.459(5)	428.29(3)
P7	3.81	9.6535(3)	8.80906(9)	5.2000(1)	105.399(3)	426.33(2)
P8	4.54	9.6376(5)	8.7892(2)	5.1908(2)	105.343(5)	424.02(3)
P9	5.10	9.6258(8)	8.7732(2)	5.1835(3)	105.305(8)	422.22(5)
P10	6.02	9.6060(6)	8.7513(2)	5.1734(2)	105.242(6)	419.60(3)
P11	6.69	9.5898(6)	8.7311(2)	5.1643(2)	105.190(6)	417.30(3)
P12	7.76	9.573(2)	8.7126(7)	5.1550(7)	105.12(3)	415.1(1)
P13	8.74	9.5540(7)	8.6852(3)	5.1439(2)	105.083(7)	412.13(4)
P14	9.33	9.546(1)	8.6735(5)	5.1385(5)	105.06(2)	410.82(8)
P15	9.58	9.5402(7)	8.6653(3)	5.1350(3)	105.040(8)	409.96(4)

Cpx_3					
Pressure, GPa	$a_3,\ \text{Å}$	$b_3,\ \text{Å}$	$c_3,\ \text{Å}$	$\beta_3,\ ^\circ$	$V_3,\ \text{Å}^3$
P0 0	9.7372(2)	8.8787(3)	5.2736(2)	105.978(2)	438.30(2)
P1 0.65	9.7174(3)	8.8581(3)	5.2628(2)	105.884(3)	435.71(2)
P2 1.49	9.6961(2)	8.8343(3)	5.2511(2)	105.786(2)	432.84(2)
P3 1.53	9.6932(2)	8.8315(3)	5.2496(2)	105.774(2)	432.47(2)
P4 2.24	9.6775(2)	8.8132(2)	5.2408(2)	105.708(2)	430.29(2)
P5 2.66	9.6671(2)	8.8014(3)	5.2349(2)	105.670(2)	428.85(2)
P6 3.16	9.6542(5)	8.7912(6)	5.2292(4)	105.621(5)	427.42(4)
P7 4.01	9.6358(4)	8.7648(4)	5.2172(3)	105.549(3)	424.50(3)
P8 5.42	9.6027(4)	8.7280(5)	5.1993(3)	105.430(3)	420.06(3)
P9 6.20	9.5884(7)	8.7076(9)	5.1896(6)	105.369(6)	417.80(6)
P10 7.28	9.5667(2)	8.6838(2)	5.1784(2)	105.316(2)	414.92(2)
P11 7.96	9.5551(2)	8.6699(2)	5.1715(2)	105.279(2)	413.28(2)
P12 8.36	9.5480(3)	8.6598(3)	5.1672(2)	105.259(2)	412.19(2)

Cpx_4					
Pressure, GPa	$a_4,\ \text{Å}$	$b_4,\ \text{Å}$	$c_4,\ \text{Å}$	$\beta_4,\ ^\circ$	$V_4,\ \text{Å}^3$
P0 0	9.7450(4)	8.9236(4)	5.2500(3)	106.026(4)	438.80(3)
P1 0.65	9.7234(5)	8.9019(6)	5.2388(3)	105.910(3)	436.08(3)
P2 1.49	9.7024(4)	8.8737(4)	5.2262(3)	105.796(3)	432.96(3)
P3 1.53	9.6989(4)	8.8708(4)	5.2245(3)	105.783(3)	432.55(3)
P4 2.24	9.6826(4)	8.8509(4)	5.2153(3)	105.699(4)	430.28(3)
P5 2.66	9.6708(3)	8.8386(3)	5.2090(2)	105.641(2)	428.76(2)
P6 3.16	9.6589(3)	8.8245(4)	5.2026(2)	105.586(3)	427.13(2)
P7 4.01	9.6379(4)	8.7984(4)	5.1907(3)	105.493(3)	424.16(3)
P8 5.42	9.6047(4)	8.7581(4)	5.1718(3)	105.350(3)	419.53(3)
P9 6.20	9.5877(7)	8.7388(7)	5.1617(5)	105.277(6)	417.18(5)
P10 7.28	9.5678(3)	8.7103(3)	5.1501(2)	105.210(3)	414.16(2)
P11 7.96	9.5556(3)	8.6957(3)	5.1436(2)	105.168(3)	412.51(2)
P12 8.36	9.5475(3)	8.6852(3)	5.1386(2)	105.135(3)	411.32(2)
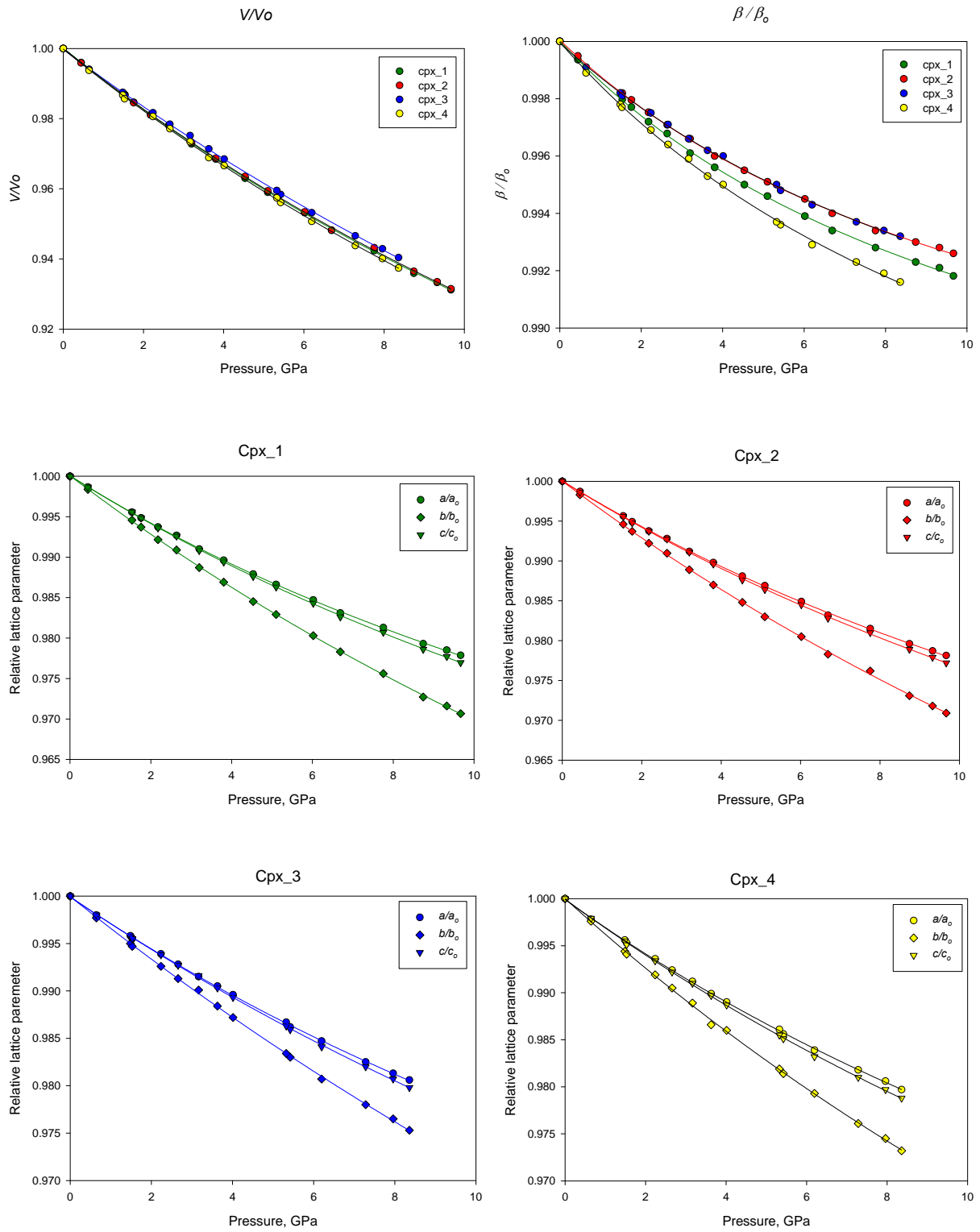
Figure 3.2-3. *Evolution of the unit-cell volumes and unit-cell parameters as a function of pressure for the diopside crystals.*

3.2.2.3. F_E-f_E plots and EoS parameters

In order to define which order of the Birch-Murnaghan EoS is required to fit the *P-V* compression data, F_E-f_E plots were used, which are shown in Figure 3.2-4. F_E is normalized stress defined as $F_E = P / [3f_E (1 + 2f_E)^{5/2}]$ and f_E is finite strain defined as $f_E = [(V_o/V)^{2/3} - 1] / 2$ (Angel, 2000).

On the F_E-f_E plots from this study the points lie on an inclined straight line, which means that the data can be described by a third order truncation of the EoS and *K' > 4*. The slope of the line is equal to $3K_o(K'-4)/2$ and the inclination of the line defines the *K'* value. The intersection of the line with the F_E axis yields the K_o value. The F_E-f_E plots have been calculated also for the individual crystal axes (see Appendix 3). The plots show a positive slope (i.e. *K'>4*) for all unit-cell parameters except the *b*-axis. The plot for the *b*-axis shows zero slope (*K'= 4*). Therefore, for the *b*-axis, the data might be fitted by a straight horizontal line. This means that *K'* may be fixed to 4 and a second-order Birch-Murnaghan EoS may be used. Equations for the weighted fit lines from the plots on Figure 3.2-4 and Appendix 3 are presented in Table 3.2-4. The first coefficient in the equation equals the value of bulk modulus (in GPa), and the second one defines the slope of the fitted line.

Table 3.2-4. *Equations for the weighted fits from the F_E-f_E plots (Figure 3.2-4 and Appendix 3) of volumes and unit-cell axes for the diopside crystals (Normalized pressure F_E is defined in GPa)*

Cpx_1	Cpx_2
volume $F_{E\,(V)} = 107(1) + 390(51)\,f_E$	volume $F_{E\,(V)} = 108(1) + 376(58)\,f_E$
a-axis $F_{E\,(a)} = 105(1) + 872(52)\,f_E$	*a*-axis $F_{E\,(a)} = 108(1) + 807(67)\,f_E$
b-axis $F_{E\,(b)} = 88(1) + 66(30)\,f_E$	*b*-axis $F_{E\,(b)} = 89(1) + 69(44)\,f_E$
c-axis $F_{E\,(c)} = 106(1) + 589(59)\,f_E$	*c*-axis $F_{E\,(c)} = 108(1) + 554(58)\,f_E$
Cpx_3	Cpx_4
volume $F_{E\,(V)} = 114(1) + 298(73)\,f_E$	volume $F_{E\,(V)} = 106(1) + 336(60)\,f_E$
a-axis $F_{E\,(a)} = 110(1) + 786(75)\,f_E$	*a*-axis $F_{E\,(a)} = 104(1) + 776(81)\,f_E$
b-axis $F_{E\,(b)} = 96(1) + 6(61)\,f_E$	*b*-axis $F_{E\,(b)} = 86(1) + 50(34)\,f_E$
c-axis $F_{E\,(c)} = 111(1) + 469(78)\,f_E$	*c*-axis $F_{E\,(c)} = 103(1) + 496(76)\,f_E$
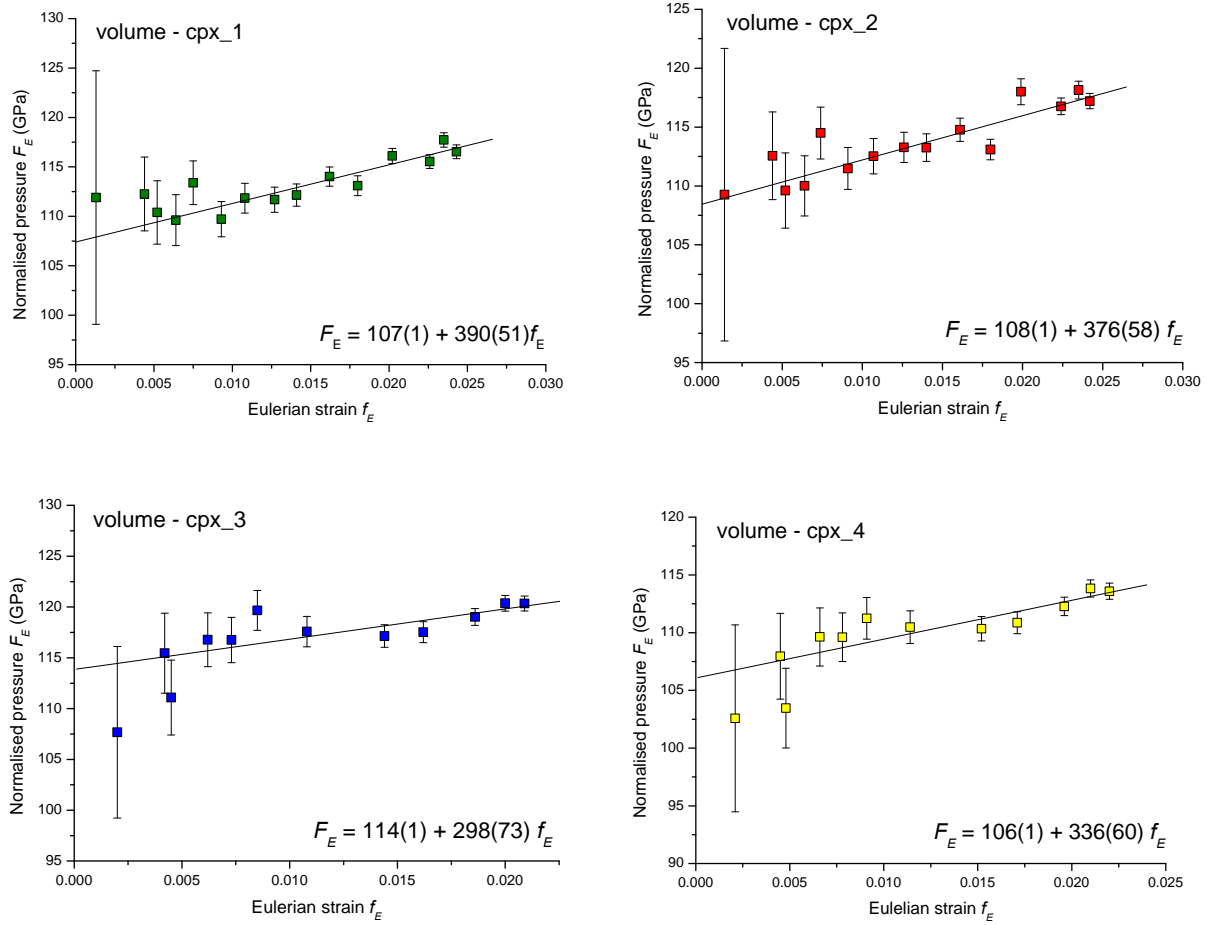
Figure 3.2-4. F_E-f_E plots based on the Birch-Murnaghan EoS for diopside single crystals.

Since the F_E-f_E plots (Figure 3.2-4 and Appendix 3) suggest that K' is larger than 4, the pressure-volume data of all four crystals have been fitted using a third-order Birch-Murnaghan equation of state, refining simultaneously the unit-cell volume at ambient pressure V_o, the bulk modulus K_o and its first pressure derivative K' using the EOSFIT 5.2 program (Angel, 2002). A linearised Birch-Murnaghan EoS in which the cube of a unit-cell axis is used instead of the volume has been used to fit the unit cell a, b and c parameters of the four diopside crystals. The refined coefficients are reported in Table 3.2-5. The fitted values are in good agreement with those obtained from the linear fits of the F_E-f_E plots.

The value of compressibility β_o was calculated as $\beta_o = -1/3\ K_o$ for unit-cell parameters and as $\beta_{o(V)} = -1/K_o$ for unit-cell volumes. The compressibility anisotropy scheme for all four diopside crystals is $\beta_{oa} \approx \beta_{oc} < \beta_{ob}$, with the *b*-axis being most compressible for all four diopside crystals.

Table 3.2-5. *Birch-Murnaghan equation of state parameters for the diopside single crystals.*

	cpx_1	cpx_2	cpx_3	cpx_4
a_o(Å)	9.7495(2)	9.7535(3)	9.7372(2)	9.7449(5)
K_{oa}(GPa)	105(1)	108(1)	110(2)	104(2)
K'	9.6(5)	9.0(5)	8.8(6)	9.1(8)
β_{oa} (GPa^{-1})	-0.00317	-0.00309	-0.00303	-0.00321
b_o(Å)	8.9236(4)	8.9249(2)	8.8787(3)	8.9236(4)
K_{ob}(GPa)	88(1)	89(1)	96(1)	86(1)
K'	4.5(3)	4.5(3)	4.0(4)	4.4(4)
β_{ob}(GPa^{-1})	-0.00379	-0.00375	-0.00347	-0.00388
c_o(Å)	5.2514(2)	5.2548(1)	5.2736(2)	5.2500(3)
K_{oc}(GPa)	105(1)	108(1)	111(2)	103(2)
K'	7.8(5)	7.5(4)	6.8(6)	7.1(6)
β_{oc}(GPa^{-1})	-0.00317	-0.00309	-0.00300	-0.00324
V_o(Å^3)	439.37(3)	440.09(2)	438.30(2)	438.80(3)
K_o(GPa)	107(1)	108(1)	113(1)	106(1)
K'	6.5(4)	6.3(4)	5.7(5)	6.1(5)
β_{oV}(GPa^{-1})	-0.00935	-0.00926	-0.00885	-0.00943

3.2.3. Discussion

As already mentioned, measured equations of state are usually parameterized in terms of the values of the bulk modulus K_o and its pressure derivative K'. The value of K_o characterizes the compressibility of a mineral and it usually depends on chemical composition. Table 3.2-6 lists values of K_o and K' measured for Ca-rich clinopyroxenes with different chemical compositions in *M1* and *T* sites. For example, Zhang et al. (1997) showed that the ratio of Fe^{2+} and Mg^{2+} influences the elasticity of Ca-rich clinopyroxenes at high pressures. According to their work, diopside ($CaMgSi_2O_6$) is more compressible than hedenbergite ($CaFeSi_2O_6$) as shown by their axial and volume compressibilities because the FeO_6 octahedron is significantly more rigid than MgO_6 at high pressures. Nestola et al. (2005), who studied $CaNiSi_2O_6$ clinopyroxene and compared its EoS with other $CaM1Si_2O_6$ pyroxenes, concluded that although the deformation mechanism of the *C2/c* pyroxene structure is mainly determined by the cation at the *M2* site, its stiffness mainly depends on the cation occupying the *M1* site and in particular on its valence electron character.

Table 3.2-6. *Values of bulk modulus for Ca-clinopyroxenes with different compositions with C2/c space group*

Clinopyroxene	Bulk modulus K_o	Pressure derivative K'	Reference
Diopside $CaMgSi_2O_6$	105.1(9) GPa	6.8(1)	Tribaudino et al., 2000
Diopside $CaMgSi_2O_6$	104.1(9) GPa	6.2(3)	Zhang et al., 1997
Diopside$_{80}$Enstatite$_{20}$	107(1) GPa	5.7(3)	Tribaudino et al., 2000
Hedenbergite $CaFeSi_2O_6$	117(1) GPa	4.3(4)	Zhang et al., 1997
Hedenbergite $CaFeSi_2O_6$	108.8(4) GPa	6.6(1)	Nestola et al., 2008
Ni-diopside $CaNiSi_2O_6$	117.6(3) GPa	6.4(1)	Nestola et al., 2005
Diopside $(Ca,Na)(Mg,Fe)(Al_{0.01}Si_{1.99})O_6$	114(4) GPa	5(2)	Levien and Prewitt, 1981
Fassaite $(Ca,Mg,Fe,Ti,Al)(Si_{1.73}Al_{0.27})_2O_6$	113(3) GPa	4.8(7)	Hazen and Finger, 1977

The values of bulk modulus K as well as its pressure derivative K' for diopside from our study (cpx_1, cpx_2, cpx_4) are quite comparable with previous works (Tribaudino et al., 2000; Zhang et al., 1997). Al-bearing hydrous diopside (cpx_3) is much stiffer than pure diopside. Unfortunately, no data are available on the influence of Al in the tetrahedral site (such as Ca-

Tschermak's pyroxene) on the compressibility of diopside. Only indirect conclusions are possible. The diopside from Levien and Prewitt (1981) contains Fe in *M1*, Na in *M2* sites and some amount of Al in the tetrahedral site. Its bulk modulus is much higher than for pure diopside and equals 114(4) GPa. Fassaite (Hazen and Finger, 1977) with much higher Al content in tetrahedral site has the same bulk modulus 113(3) GPa. Based on these two examples one may assume that only cations in the *M1* and *M2* sites influence the compressibility of clinopyroxene. This assumption is also consistent with the model of Thompson et al. (2005) who proposed that for *C*2/*c* clinopyroxenes the *M1* site controls their compressibility, which was confirmed by Nestola et al. (2005) for $CaNiSi_2O_6$ clinopyroxene. Therefore, we suggest that the Al in the tetrahedral position in cpx_3 diopside does not affect its compressibility. On the other hand, there is some amount of Al in the *M1* site in cpx_3, which may indeed increase the stiffness of diopside. Hence it is difficult to say whether the hydroxyl incorporation alone has a significant effect on the EoS of diopside or not. However, it certainly does not increase the compressibility of diopside.

3.3 Crystal structure refinement of hydrous diopside

3.3.1. Data collection and refinement

A structural refinement was performed on the four diopside crystals which were recovered from the diamond anvil-cells after the high-pressure experiment. Details of data collection and data reduction are presented in section 2.1.4.4. The crystallographic characteristics of the diopside crystals and details of data collections and structural refinement parameters are listed in Table 3.3-1.

Weighted least-squares refinements of the structures were performed using the SHELX97 program package (Sheldrick, 1977). The starting atomic coordinates were taking from Prencipe et al. (2000). Structures were refined with space group $C2/c$ based on F^2 using anisotropic displacement parameters. The atomic scattering curves were taken from the International Table for X-ray Crystallography (Ibers and Hamilton, 1974). Ionized scattering factors were used for Mg and Ca cations at the *M1* and *M2* sites, respectively. The Si at the tetrahedral site was assumed partially ionized and a Si^{2+} scattering curve was used, whereas neutral vs. ionized scattering curves were refined for the oxygen (O and O^{-2}) atoms. For the Al-bearing diopside (cpx_3) two different refinement procedures were used. First a series of refinements using the scattering curves of Mg^{2+} and Al^{3+} at the *M1* sites and of Si^{2+} and Al^{3+} at the *T* site was done. Their relative occupancies were refined constraining the total Al content to the value obtained from the microprobe analysis and with the additional constraint that the structural sites were fully occupied. However, given the negligible difference between the scattering curves of Si and Al or Mg and Al, a simple series of refinements also was done with only Mg at the *M1* site and Si at the *T* site. In this case, these two sites were not considered fully occupied, but the occupancies were free to vary because of the difference of one electron between Si-Al and Mg-Al atoms. Therefore, only the scattering curves of Mg and Si were used to refine the atomic positions and the occupancies at the *M1* and *T* sites, respectively, were considered as variables. Both sets of refinements gave virtually identical results, with mean atomic numbers (m.a.n.) at the *M1* and *T* sites of 12.114 and 13.873 for the first procedure and 12.110 and 13.875 for the second procedure. Note that in the second case no chemical constraints were used. These values are in good agreement with the chemical composition obtained from the microprobe analyses (i.e. 12.15e$^-$ and 13.9e$^-$ for *M1* and *T* respectively). The analysis of the Fourier-difference map for two diopside crystals (cpx_1 and cpx_4) gave a high residual electron density peak at about 0.6 Å from the *M2* position. This

suggested the presence of a *M2'* split position occupied by Mg^{2+} as observed in previous studies (Bruno et al., 1982; Rossi et al., 1987; Oberti and Caporuscio, 1991; Boffa Ballaran et al., 1998). Therefore, further refinements of cpx_1 and cpx_4 crystals were performed with an isotropic *M2'* position and with the following constraint on the occupancies of *M2* and *M2'* sites: Ca^{2+} (*M2*) + Mg^{2+} (*M2'*) = 1.

The values of the conventional agreement indices (*R)*, as well as the goodness of fit (*S*) are reported in Table 3.3-1. They are obtained using the following expressions:

$$wR_2 = \left[\sum w\left(F_o^2 - F_c^2\right)^2 / \sum w\left(F_o^2\right)^2\right]^{1/2}$$

$$R_1 = \sum \left\|F_o\right| - \left|F_c\right\| / \sum \left|F_o\right|$$

$$GoodF = S = \left[\sum w\left(F_o^2 - F_c^2\right)^2 / (n - p)\right]^{1/2}$$ where *n* is the number of reflections and *p* is the total number of parameters refined

Atomic positions and anisotropic temperature factors are listed in Appendix 4 for all four crystals. Tetrahedral *T*, *M1* octahedral and *M2* bond distances for the four diopside single crystals are reported in Table 3.3-2.

Table 3.3-1. *Crystallographic and refinement data from X-ray single crystal diffraction of diopside*

	Cpx_1 63 ppm H2O 0.088 wt.% Al_2O_3	Cpx_2 600 ppm H2O 0.059 wt.% Al_2O_3	Cpx_3 2510 ppm H2O 8.813 wt.% Al_2O_3	Cpx_4 No water 0.030 wt.% A_2O_3
Space group, Z	C2/c, 4	C2/c, 4	C2/c, 4	C2/c, 4
a, Å	9.7494(2)	9.7526(10)	9.7373(2)	9.7448(2)
b, Å	8.9235(4)	8.9259(8)	8.8803(1)	8.9228(1)
c, Å	5.2514(2)	5.2543(13)	5.2729(3)	5.2497(2)
β, °	105.909(2)	105.838(12)	105.970(2)	106.021(2)
V, Å^3	439.36(3)	440.08(2)	438.35(2)	438.74(2)
ρ_{calc}, g/cm^3	3.274	3.269	3.402	3.279
μ, mm^{-1}	2.07	2.06	2.12	2.07
Nr. unique reflections	1367	1366	1361	1357
Nr. reflections with $F^2>4\sigma(F^2)$	1211	1213	1222	1109
R_{int}(%)	2.62	2.93	3.04	3.96
R_1(%) for reflections with $F^2>4\sigma(F^2)$	2.69	2.64	3.50	3.74
R1(%)for all reflections	3.27	3.19	4.39	5.86
wR_2(%)	6.84	6.90	7.34	8.24
S	1.160	1.124	1.184	1.107
Refined parameters	56	53	55	56
$\Delta\rho_{max}$ / $\Delta\rho_{min}$, e/Å^3	0.78/-0.45	0.72/-0.38	0.73/-0.53	0.82/-0.66

3.3.2. Polyhedral geometry and discussion

The crystal structure of diopside consists of chains of corner-sharing tetrahedra elongated along the *c*-axis (Figure 1.3-1 in the introduction section 1.3.1) with the *M1* octahedral site lying between the apices of opposing tetrahedra and the larger *M2* sites between their bases (Figure 3.3-1). Cation substitution in one of the polyhedral site affects not only its own geometry but also that of the other sites. It is therefore difficult to compare the results obtained in this study with those for natural clinopyroxenes with complex chemical composition involving not only Al substitution into the tetrahedral sites, but Fe and different trivalent cations in the *M1* site and larger cations (Na, Mn, K) in the *M2* site.
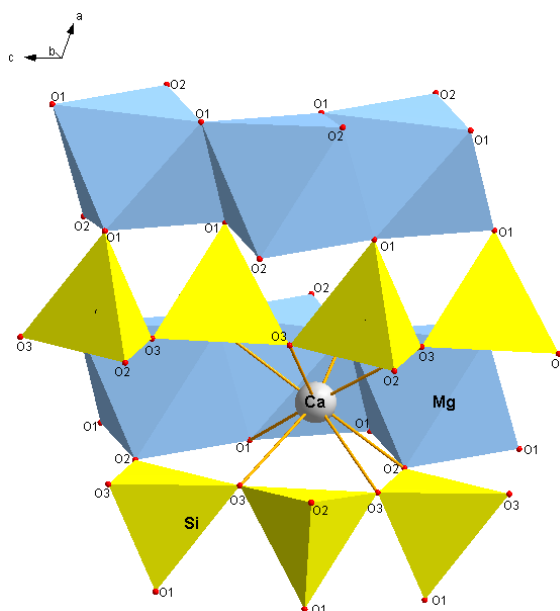
Figure 3.3-1. *Fragment of the crystal structure of diopside*
showing the coordination of Si, Mg and Ca cations

However, we can compare our results with the pure Ca-Tschermak's clinopyroxene $CaAlAlSiO_6$ (Okamura et al., 1974) to test if the several correlations between individual bond distances reported for natural pyroxenes (see for example Dal Negro et al., 1985; Dal Negro et al., 1986; Manoli and Molin, 1988) may give some qualitative indication on how water substitution

affects the polyhedral geometry. Polyhedral bond distances for the four diopside single crystals obtained in this study are reported in Table 3.3-2.

Table 3.3-2. *Cation-oxygen bond distances for the diopside crystals of this study*

		Cpx_1 *63 ppm H2O* *0.088 wt.% Al$_2$O$_3$*	*Cpx_2* *600 ppm H2O* *0.059 wt.% Al$_2$O$_3$*	*Cpx_3* *2510 ppm H2O* *8.813 wt.% Al$_2$O$_3$*	*Cpx_4* *No water* *0.030 wt.% A$_2$O$_3$*
M2 (Ca)	Ca – O2	2.3360(7) *2	2.3447(9) *2	2.3577(9) *2	2.325(1) *2
	Ca – O1	2.3617(7) *2	2.3665(7) *2	2.3702(9) *2	2.357(1) *2
	Ca – O3$_{C1}$	2.5663(7) *2	2.5638(8) *2	2.5517(9) *2	2.569(1) *2
	Ca – O3$_{C2}$	2.7220(7) *2	2.7199(7) *2	2.6944(9) *2	2.725(1) *2
	<Ca – O>	2.4965	2.4987	2.4935	2.494
M2' (Mg)	Mg – O1	1.9486(6) *2			1.910(1) *2
	Mg – O2	2.2934(7) *2			2.286(1) *2
	Mg – O3$_{C1}$	2.9988(7) *2			3.045(7) *2
	Mg – O3$_{C2}$	3.0764(7) *2			3.115(7) *2
	<Mg – O>	2.5793			2.589
M1 (Mg,Al)	Mg – O2	2.0552(7) *2	2.0553(7) *2	2.0355(10) *2	2.053(1) *2
	Mg – O1$_{A2}$	2.0616(6) *2	2.0625(8) *2	2.0447(8) *2	2.062(1) *2
	Mg – O1$_{A1}$	2.1248(7) *2	2.1206(7) *2	2.1066(10) *2	2.129(1) *2
	<Mg – O>	2.0805	2.0794	2.0627	2.0813
T (Si, Al)	Si – O2	1.5859(7)	1.5890(7)	1.6029(9)	1.586(1)
	Si – O1	1.6004(7)	1.6003(7)	1.6150(9)	1.600(1)
	Si – O3$_{A1}$	1.6681(6)	1.6706(7)	1.6735(8)	1.666(1)
	Si – O3$_{A2}$	1.6867(6)	1.6883(7)	1.6930(9)	1.686(1)
	<Si – O>	1.6338	1.6371	1.6461	1.6345
	O3-O3-O3 (^{o})	165.95(6)	166.27(6)	165.99(7)	165.60(9)

M2 polyhedron

Ca^{2+} is the only cation occupying the *M2* site in diopside, although the results of the refinements suggest the presence of a small amount of Mg at the *M2* site for two of our samples (cpx_1 and cpx_4). The *M2* cation is coordinated by 8 oxygen atoms: two O1, and two O2 non bridging oxygens and four O3 bridging oxygens (Figure 3.3-1). The *M2*-O distances range from

2.3360(7) to 2.7220(7)Å for cpx_1, from 2.3447(9) to 2.7199(7)Å for cpx_2, from 2.3577(9) to 2.6944(9)Å for cpx_3 and from 2.325(1) to 2.725(1)Å for cpx_4. The distortion and the size of the *M2* polyhedron decreases with increasing Al content.

In the diopside structure, cations smaller than Ca (i.e. Mg^{2+} and Fe^{2+}) occupy a slightly different *M2* position denoted as *M2'* split position (Rossi et al., 1987; Oberti and Caporuscio, 1991; Boffa Ballaran et al., 1998). In this study, the *M2'* split site was found for cpx_1 and cpx_4 crystals. As observed by Rossi et al. (1987), the large cation (Ca) occupies the center of the eight-coordinated *M2* site, the smaller one (in our case Mg) tends to move towards the walls of the cavity toward the *M1* site in a position similar to that of the *M2* site of high-clinoenstatite or $ZnSiO_3$ (Bruno et al., 1982). The cation at the *M2'* site is bonded to two O1 and two O2 oxygen atoms at distances of 1.9486(6) and 2.2934(7)Å, respectively for cpx_1, and at distances of 1.910(1) and 2.286(1)Å for cpx_4. These distances are smaller than the *M2*-O1 and *M2*-O2 bond length, whereas the four *M2'*-O3 bond distances are much larger i.e. 2.9988(7)Å*2 and 3.0764(7)Å*2 for cpx_1 and 3.045(7)Å*2 and 3.115(7)Å*2 for cpx_4 (Figure 3.3-2).

A   **B**
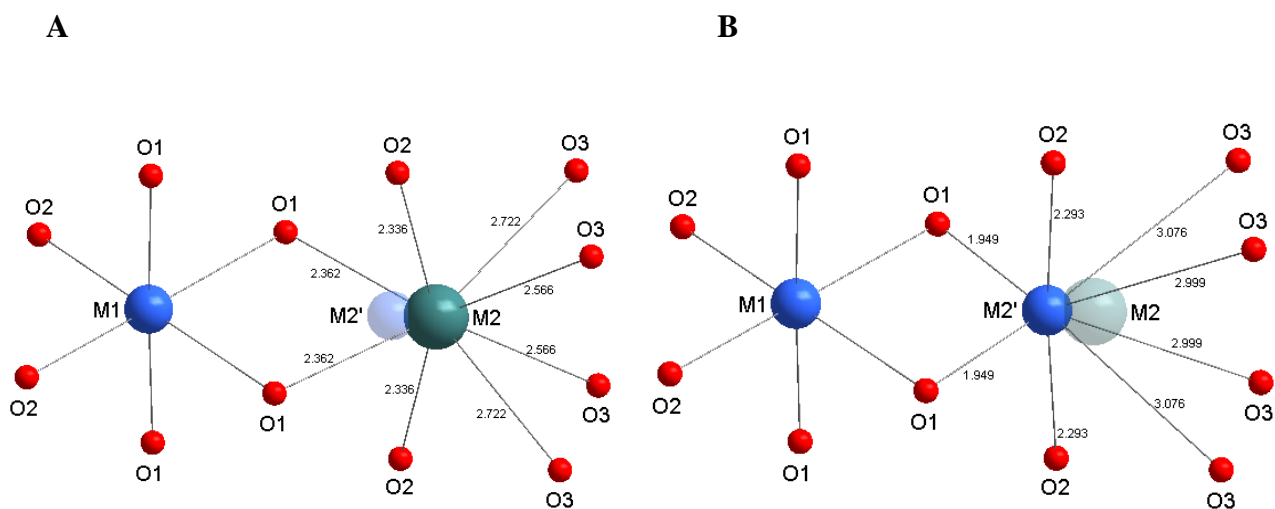
Figure 3.3-2. *The coordination around the M1, M2 and M2' sites in diopside crystal (cpx_1). Picture **A** shows the bond distances for the cation in the M2 site, picture **B** – for the M2' site.*

The longest bonds with the bridging oxygens O3 (*M2*-O3$_{C2}$) are sensitive not only to the cation occupancy at the *M2* site, which in the case of our samples is constant (i.e. practically only Ca), but also to the amount of Al substitution at the tetrahedral site (Al^{IV}). In particular, an inverse

correlation between $M2$-O3$_{C2}$ and tetrahedral bond distances involving the non bridging oxygens, T-O$_{nbr}$, was previously found (Dal Negro et al., 1985; 1986). A linear inverse correlation is indeed observed between the $M2$-O3$_{C2}$ and T-O1 bond distances (Figure 3.3-3a), whereas, a small but clear deviation from such linearity is observed for the Al-bearing diopside sample, cpx_3, when the T-O2 distance is considered instead of T-O1 (Figure 3.3-3b). Moreover, in Figure 3.3-4b, the cpx_2 sample plot at a slightly smaller $M2$-O3$_{C2}$ distance than the other two diopside samples, suggesting that a small amount of Al^{IV} may be present in this crystal, which is consistent with microprobe analyses (see Table 3.2-2 in section 3.2.1.)

a   *b*
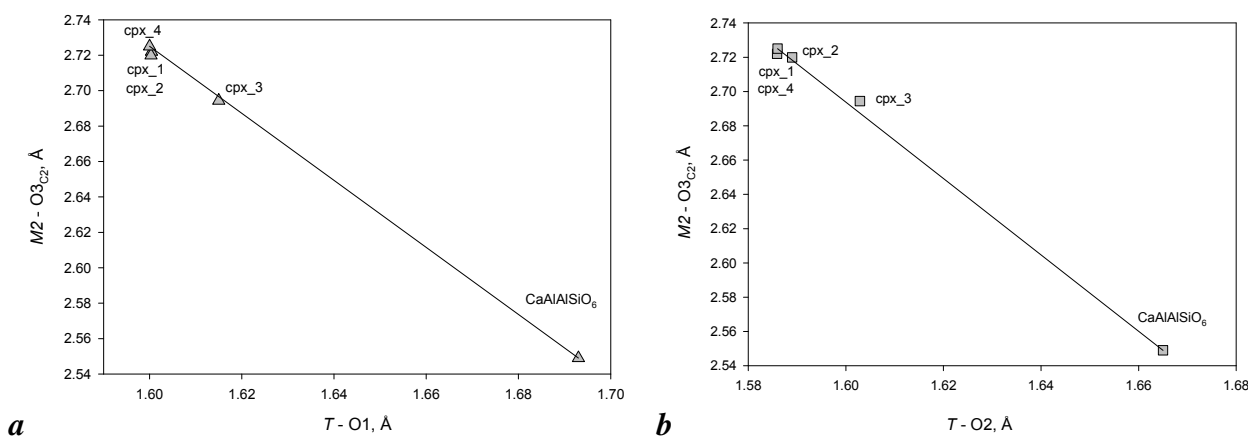
Figure 3.3-3. *Relationship between bond distances M2-O3$_{C2}$ and T-O1 (a) and T-O2(b) for the four diopside crystals from this study and for Ca-Tschermak's clinopyroxene (Okamura et al., 1974)*

M1 octahedron

The edge-sharing octahedra (*M1*) form chains parallel to the tetrahedral chains elongated along the *c*-axis. *M1* octahedra are coordinated by two O2 and four O1 oxygen atoms (Figure 3.3-1) and are occupied by Mg^{2+} cations in pure diopside (cpx_1, cpx_2, cpx_4), whereas, according to the Tschermak's substitution, they are occupied by both Mg^{2+} and Al^{3+} cations in the Al-bearing diopside (cpx_3). The *M1*-O distances range from 2.0552(7) to 2.1248(7)Å for cpx_1, from 2.0553(7) to 2.1206(7)Å for cpx_2, from 2.036(1) to 2.107(1)Å for cpx_3 and from 2.053(1) to 2.129(1)Å for cpx_4. The *M1*-O distances in Al-bearing cpx_3 are smaller than for pure diopside crystal due to the presence of the smaller Al^{3+}. A linear correlation is found between the mean *M1*-

O distances and the Al content at the *M1* site (Al^{VI}) for the four diopside crystals of this study and for Ca-Tschermak's (Okamura et al., 1974) pyroxene (Figure 3.3-4).
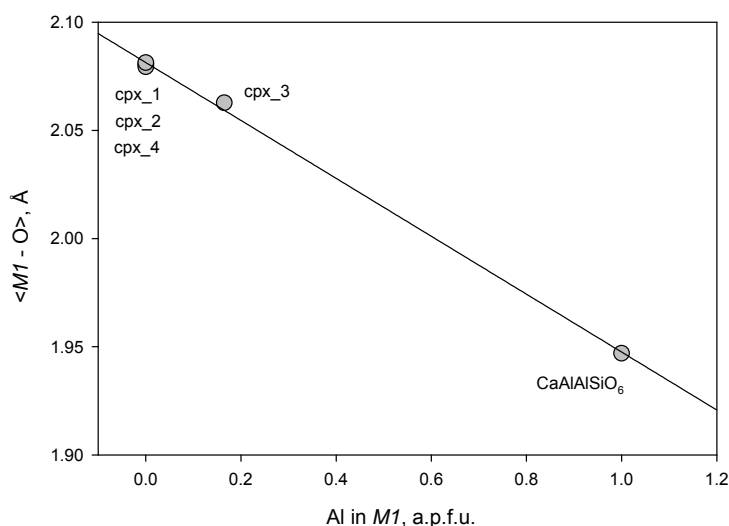
Figure 3.3-4. *Correlation between M1-O distances and Al content at the M1 site for the four diopside crystals from this study and for Ca-Tschermak's clinopyroxene (Okamura et al., 1974)*

<u>*T-tetrahedron*</u>

The tetrahedra are fully occupied by Si cations in pure diopside (cpx_1, cpx_2, cpx_4) and by Si and Al^{3+} cations in Al-bearing diopside (cpx_3). The tetrahedral cations are coordinated by O1, O2 and two O3 oxygen atoms (Figure 3.3-1). There are four unique bond distances in the distorted $Si(Al)O_4$ tetrahedra. The *T*-O distances range from 1.5859(7) to 1.6867(6)Å for cpx_1, from 1.5890(7) to 1.6883(7)Å for cpx_2, from 1.6029(9) to 1.6930(9)Å for cpx_3 and from 1.586(1) to 1.686(1)Å for cpx_4. The tetrahedral bond distances in pyroxenes depend on the Al content and on the radius of the cations present at the *M1* and *M2* sites (Rossi et al., 1983). An increase in Al^{IV} corresponds to an increase of all *T*-O bond lengths and in particular of the $T\text{-}O_{nbr}$ distances. A linear correlation exists between the mean *T*-O bond distance and Al^{IV} content (Figure 3.3-5) as it has been found for the mean *M1*-O distances and Al^{VI} (Figure 3.3-4). However, a careful analysis of the behaviour of the $T\text{-}O_{nbr}$ and $T\text{-}O_{br}$ distances separately as a function of Al^{IV} content reveals

that whereas the T-O_{nbr} bond length indeed varies practically linearly with Al^{IV} content, the T-O_{br} bond length shows a clear deviation of linearity (Figure 3-3.6). Moreover, the three pure diopside samples also show a larger scatter, with cpx_2 (i.e. the hydrous diopside) having the largest value.
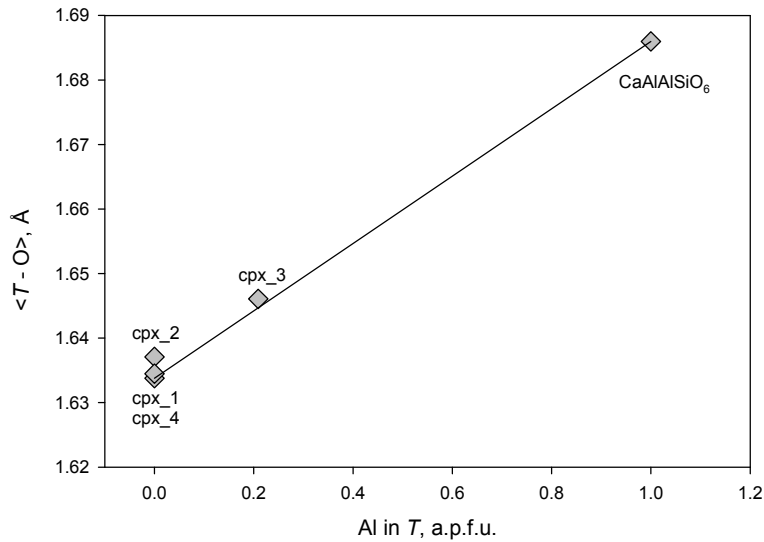
Figure 3.3-5. *Tetrahedral (T) mean bond distances versus Al^{IV} content. The value for Ca-Tschermak's pyroxene is taken from Okamura et al. (1974)*
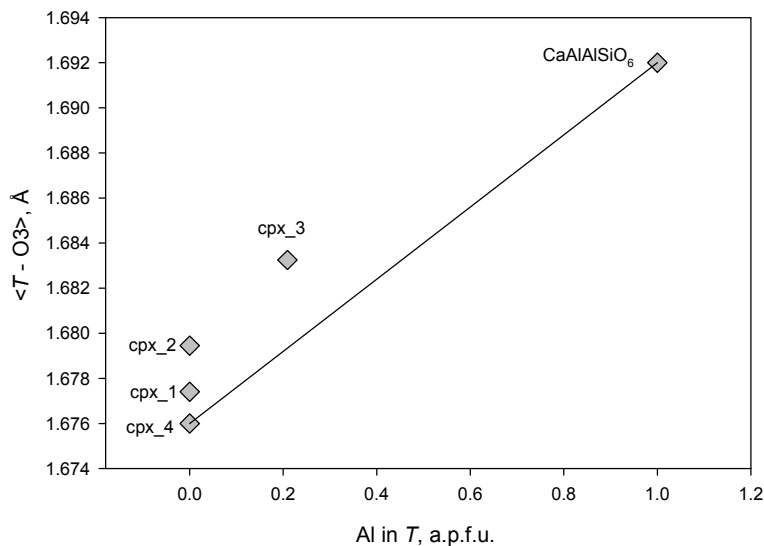
Figure 3.3-6. *Mean tetrahedral bond distance with the O3 bridging oxygens as a function of Al^{IV} content. Note the deviation from linearity of hydrous diopside and of the Al-bearing diopside*

The assumption of hydrogen incorporation onto O2 atom is discussed in section 3.1.1.3 for pure diopside and in section 3.1.2.3 for Al-bearing diopside. It was established from the polarized infrared spectra that the proton attaches to the O2 oxygen atom forming a hydrogen bond pointing towards O3. The deviation of *T*-O2 as a function of *M2*-O3 bond lengths from linearity of cpx_3 diopside on Figure 3.3-3b supports the protonation of the O2 oxygen atom when substitution of Si by Al takes place. Moreover, the deviation of *T*-O3 bond lengths as a function of Al content in the *T* site for Al-bearing cpx_3 (Figure 3.3-6) as well as for pure hydrous cpx_2 also supports the assumption of the O3 atom being involved in hydrogen incorporation.

4. GEOPHYSICAL AND GEOCHEMICAL IMPLICATIONS

4.1. The role of clinopyroxene in water storage in the upper mantle

The upper mantle mostly consists of olivine and pyroxenes (see Figure 1.1-3 in section 1.1). Their abundances are quite variable with 50-80 % of olivine, 10-50% of orthopyroxene, 1-5% of clinopyroxene and 1-20% of garnet. Maaløe and Aoki (1977) reported average abundances for the upper mantle minerals derived from the composition of lherzolites as 63% of olivine, 30% of orthopyroxene, 2% of clinopyroxene and 5% of garnet.

Figure 4.1-1 (left) shows the calculated water solubility of pure diopside as a function of pressure at constant temperature of $1100^{o}C$. These data were calculated from the thermodynamic model which was calibrated in this study. The comparison of these data with experimental results on olivine by Kohlstedt et al. (1996) and by Mosenfelder et al. (2006) (see Figure 4.1-1-right) shows that pure diopside dissolves a very small amount of water as compared to olivine, particularly in the deep upper mantle.

The water solubility in pure diopside in this study was calibrated under high silica activity. Under low silica activity in the upper mantle, the water solubility in diopside may change. However, it is unlikely to change by orders of magnitude. Under low silica activity it is possible to stabilize water in Si vacancies. However, this type of defect if known to have a large molar volume, therefore, it will probably be unimportant at high pressures. Also, the experiments with different oxide activities reported in this study yielded similar water solubilities in diopside at the same P and T, despite the differences in the IR spectra.

Figure 4.1-1. *Water solubility in pure diopside (left) and olivine (right) as a function of pressure at 1100°C and along two mantle geotherms. The data for pure diopside were calculated according to the thermodynamic model calibrated at the present study (see section 3.1.1.5). The data for olivine were taken from Kohlstedt et al. (1996) and Mosenfelder et al. (2006). Note that Mosenfelder et al. and Kohlstedt et al. use a different calibration for the extinction coefficient of water in olivine, which accounts for most of the difference between the two data sets.*

Natural clinopyroxenes always contain some aluminum. However, the calculated water solubility, shown in Figure 4.1-1 represents the situation for the Al-free system. Al solubility in clinopyroxene strongly depends on pressure and temperature. Figure 4.1-2 shows a pressure composition phase diagram for the CMAS system. The Al content decreases with pressure, because at elevated pressure most of the Al enters garnet. Since at high pressure, Al solubility in clinopyroxene is low, the Al-free system may very well approximate the situation in the deep upper mantle. I therefore conclude that clinopyroxene is not a significant host of water in the deeper part of the upper mantle, despite the fact that the modal abundance of clinopyroxene in an undepleted pyrolitic mantle is actually significant.
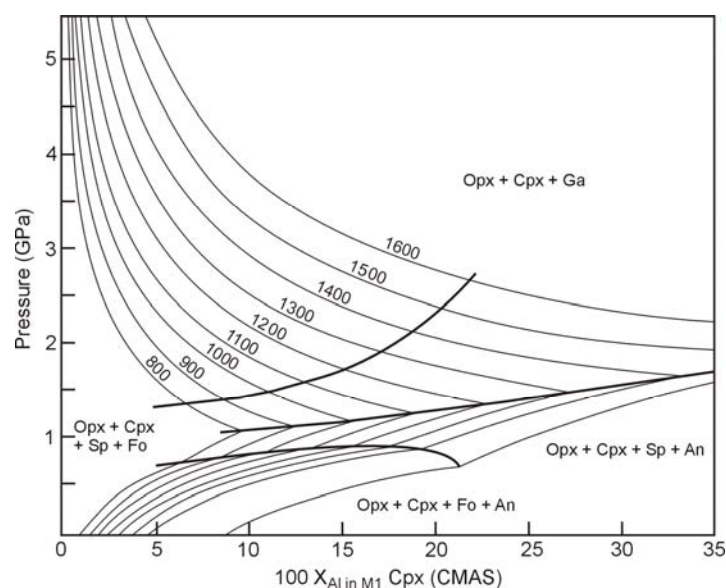
Figure 4.1-2. *Pressure-composition phase diagram for the CMAS system showing the fit of the calculated isotherms (^{o}C) to the experimentally determined Al contents of clinopyroxene. Modified after Gasparik (2003).*

On the other hand, in the shallow upper mantle Al solubility in clinopyroxene is high. Therefore the effect of Al on water solubility has to be considered. The aluminum contents in Al-bearing diopsides from this study ranged between 2.38 - 9.98 wt.% Al_2O_3 at 15 kbar and $1000^{o}C$, 1.58 - 4.20 wt.% Al_2O_3 at 25 kbar, $900^{o}C$, 1.54-8.37 wt.% Al_2O_3 at 25 kbar and $1100^{o}C$, which is much more than indicated by the equilibrium isopleths calculated by Gasparik (2003) (5.61, 1.53 and 3.06 wt.% Al_2O_3 for the three conditions respectively). One reason may be that the data obtained by Gasparik (2003) are for the CMAS system without water. With the presence of water the Al solubility may actually increase because of additional possible substitution mechanisms for Al such as $CaMgAlHSiO_6$ (see section 3.1.2.4 - Hydrogen substitution mechanism). However, since no other phases except Al-bearing diopside were obtained in the experiments from this study (only in two experiments corundum was found) it seems also possible that the unusually high Al contents in some experiments are a metastable feature related to the failure of garnet nucleation. Nevertheless, it is still possible to extract from the experimental data the composition of a water-saturated aluminous clinopyroxene in equilibrium with garnet. For this, I assume that the amount of Tschermak's substitution in equilibrium with garnet in the hydrous system is the same as in the anhydrous system. On top of this, some Al is dissolved in the clinopyroxene as a $CaMgAlHSiO_6$

component. The ratio of this component to the Tschermak's component can directly be calculated from the observed ratio of H over Al for given *P* and *T*, see Table 4.1-1.

The partition coefficient of water between two phases at water saturation is the ratio of the water solubilities in the two phases. Olivine, pyroxenes and garnet are the main minerals in the upper mantle. While water partitions slightly more into olivine at pressures above 90 kbar, at lower pressures water strongly partitions into the aluminous orthopyroxene (Mierdel et al., 2007). The work by Mierdel et al. (2007) includes a thermodynamic model of water solubility in aluminous enstatite. From this model, the water solubility in Al-saturated orthopyroxene was calculated for the same three conditions where the water solubility in aluminous diopside was measured (Table 4.1-1). From these values it is possible to calculate the partition coefficient of water between orthopyroxene and clinopyroxene at alumina saturation. For 15 kbar and 1000°C $D_{cpx/opx}$=0.66; for 25 kbar and 900°C $D_{cpx/opx}$=0.24; and for 25 kbar and 1100°C $D_{cpx/opx}$=0.54 (see Table 4.1-1). These data imply that at uppermost mantle pressures, water contents in clinopyroxene and orthopyroxene should be comparable. The partition coefficient may depend significantly on temperature, with higher temperatures favoring stronger partitioning into clinopyroxene. This would be consistent with data from Aubaud et al. (2004) who reported $D_{cpx/opx}$ = 1.4 from experiments around 1300 ˚C. It would also be consistent with observations from natural mantle xenoliths, which typically show up to twice higher water contents in clinopyroxenes as compared to orthopyroxenes (Skogby, 2006). The observed pressure and temperature dependence of water solubility in clinopyroxenes is also comparable to that of the orthopyroxenes. The experimental data presented here clearly show that water solubility in aluminous diopside decreases with increasing temperature, as for orthopyroxene (Mierdel et al. 2006). The pressure dependence is not so well constrained from the experiments in this study, but since alumina solubility in clinopyroxene generally decreases with pressure, a similar decrease of water solubility with pressure is expected for clinopyroxene as for orthopyroxene. Together with the low water solubilities in olivine and garnet at low pressures, this means that the upper water mantle budget is dominated by the pyroxenes. Due to its higher modal abundance, orthopyroxene will usually be the main host of water in the uppermost mantle, but clinopyroxene may become important in some fertile compositions.

Table 4.1-1. *Calculated water solubility in orthopyroxene and clinopyroxene at alumina saturation and obtained partition coefficients of water. Maximum Al contents in the presence of water in clinopyroxenes were calculated according to H:Al molar ration obtained in this study.*

	water solubility in Al-saturated opx (Mierdel et al., 2006) (in ppm H_2O)	max. Al content in cpx (Gasparik, 2003) (in wt.% Al_2O_3)	max. Al content in cpx in the presence of water (in wt.% Al_2O_3)	calculated water content in cpx at Al saturation (in ppm H_2O)	partition coefficient cpx/opx
25 kbar 1100°C	1779	3.06	3.53	953	0.54
25 kbar 900°C	4144	1.53	1.97	1011	0.24
15 kbar 1000°C	3315	5.61	6.66	2199	0.66

The data of this study are therefore entirely consistent with a model of bulk water solubility in the upper mantle proposed by Mierdel et al. (2007). Figure 4.1-3 shows water solubility in upper mantle minerals as a function of depth for a typical continental shield and oceanic geotherm. Water solubility in aluminum-saturated orthopyroxene decreases with depth. In contrast, according to work by Kohlstedt et al. (1996), water solubility in olivine increases with both pressure and temperature. The model assumes that mantle contains 60 % of olivine and 40% of Al-saturated enstatite. In this model bulk mantle water solubility has a pronounced minimum between 150 and 200 km depth. This corresponds to the location of the seismic low-velocity zone (LVZ) below continental shield. Mierdel et al. (2007) suggested that in the depth interval of the seismic low-velocity zone, a few hundred ppm of water are probably sufficient to trigger the formation of a hydrous melt. For the hotter oceanic geotherm the upper boundary of the zone of minimum water solubility is shifted to a depth of 60-80 km, which consistent with the position of low-velocity zone below oceans. The sharp increase in water solubility above the low-velocity zone explains why this upper boundary is usually well resolved in seismic data, while on the other hand the gradual increase in water solubility below the low-velocity zone corresponds to a diffuse nature of this seismic boundary.
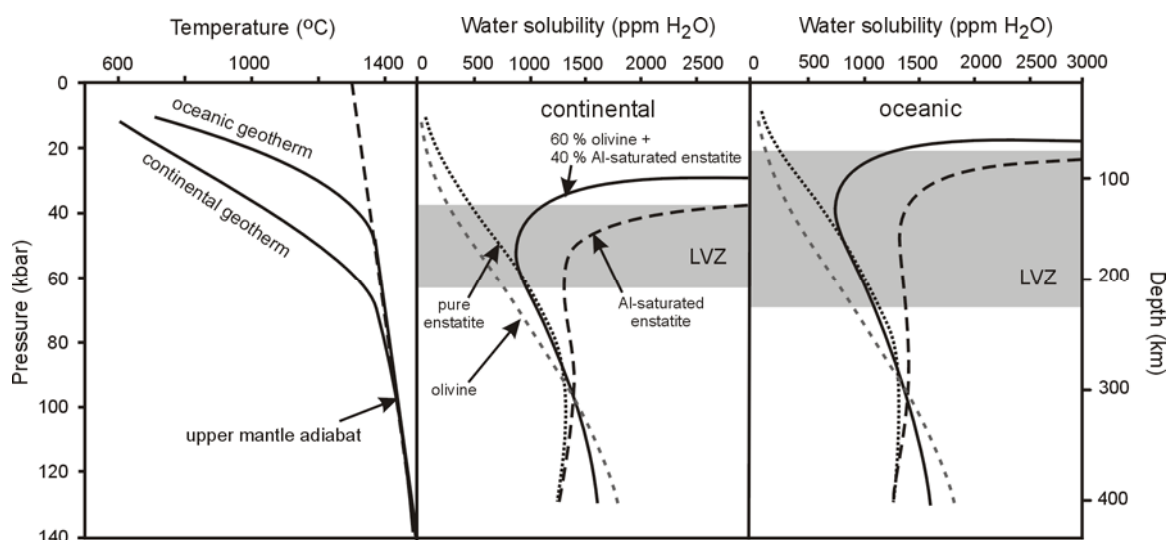
Figure 4.1-3. *Water solubility in upper mantle minerals as a function of depth for a typical continental shield and oceanic geotherm. Redrawn from Mierdel et al. (2007).*

4.2. Water in clinopyroxene and recycling of water in subduction zones

After dehydration of amphibole and other hydrous minerals, the basaltic layer of the subducted oceanic crust consists of eclogite, with the main constituent minerals pyrope-rich garnet and omphacite. According to Lu and Keppler (1997), the amount of water recycled by subducted oceanic crust may be estimated by multiplying the total length of subduction zones on Earth (42000 km) with the average speed of subduction of 5 cm/year the thickness of the oceanic crust of 6 km with a density of 3 g/cm^3 and its water content. Based on water solubility in garnet they calculated the amount of water recycled into the mantle during the last three billion years since Proterozoic eon to be between 2.0 and $4.9*10^{16}$ tons for the case of hot and cold subduction, respectively. This corresponds to 1.5 to 3.5 % of the total water reservoir of the present hydrosphere of $1.4*10^{18}$ tons.

The water solubility in clinopyroxene is much higher than in garnet. However, eclogite may contain variable amounts of garnet, up to 55% (Coleman et al., 1965). A rough estimate of the amount of water recycled by nominally anhydrous minerals in subduction zones may be obtained by assuming that after dehydration of amphibole, the eclogite contains still about 200 ppm of water

in pyrope and 2500 ppm of water in omphacite. Over one billion years this would – at present subduction rate and assuming the present length of subduction zones – recycle $4.67 \cdot 10^{17}$ tons of water into the mantle. This corresponds to 3.3 % of the total mass of the oceans. If this water loss were not balanced by outgassing, it would correspond to a reduction of sea level by 130 m. This number is quite comparable to the estimated effect of 1-2 % serpentine in the mantle below the subducted slab (Rüpke et al. 2004). It therefore demonstrates that nominally anhydrous minerals significantly contribute to the recycling of water into the mantle. In reality, their effect will be even larger, for two reasons:

    - The data in this study suggest that water solubility in aluminous clinopyroxenes very much increases with decreasing temperature. At the low temperatures inside the slab, therefore even higher water solubilities may be possible.

    - There is usually some advective flow of mantel material above the slab, which is dragged into the deeper mantle parallel to the movement of the slab. Water released from the slab during the decomposition of hydrous phases may therefore partially be dissolved in olivine of the advected peridotite, which provides an additional mechanism of water subduction. As the water solubility in olivine increases with depth, this would also be a mechanism to retain water released from hydrous omphacite, if the water solubility in the aluminous clinopyroxene decreases with increasing depth.

    Quantitative estimates of water recycling into the mantle will therefore need to take the effect of nominally anhydrous minerals, in particular of clinopyroxene and olivine into account. Precise predictions are only possible by coupling mantle convection models with models of the stability of hydrous phases and models of water solubility in nominally anhydrous minerals. The present study provides some starting point for this type of modeling. Moreover, it suggests that the importance of serpentine in recycling water into the mantle has probably been overestimated and some features of models that strongly rely on serpentine subduction may be in error. For example, the model by Rüpke et al (2004) predicts some maximum of the water stored in the oceans about 2 billion years ago, with water being transferred from the oceans into the mantle since then. This is because they assume that only 2 billion years ago the Earth has cooled sufficiently and the geotherms in subduction zones have been lowered enough to allow the subduction of serpentine. If however, nominally anhydrous minerals provide a mechanism of water subduction independent of serpentine stability, this feature would probably largely disappear. Indeed reconstructions of sea level suggest some oscillations in the phanerozoic, but not necessarily a generally decreasing trend of sea level over the last two billions of years (e.g. Hallam, 1992; Miller et al., 2005).

4.3. Remote sensing of water in the mantle

Since hydrogen incorporation in mantle minerals may change elastic properties of minerals it may change the seismic wave velocities as well (for example, Karato, 1995, 2006). The work by Jacobsen (2006) summarized the results of different authors on influence of water on bulk modulus of nominally anhydrous minerals (Figure 4.3-1). It suggests that all investigated mantle minerals such as olivine, ringwoodite and wadsleyite become more compressible with increasing hydroxyl content. According to my data, diopside behaves in the opposite way: the compressibility of diopside decrease with increasing water and Al content in the structure.

The different effect of water on the elastic properties of minerals may be explained by different OH incorporation mechanisms. For example, the main dissolution mechanism for water in olivine is a formation of vacancies on the Mg site and substitution of Mg^{2+} cations by proton pairs ($2H^+ = Mg^{2+}$) (e.g. Bai and Kohlstedt, 1993). Such protonated vacancies generally increase the compressibility. Therefore, the bulk modulus will decrease with increasing water concentration. The same mechanism is possibly responsible for the effect of water on the bulk modulus of wadsleyite and ringwoodite. On the other hand, in diopside Al cations and protons substitute for Si in tetrahedral position ($Al^{3+} + H^+ = Si^{4+}$). This means that the dissolution of water in aluminous diopside actually does not create any vacancies, and accordingly, diopside becomes stiffer in response to the coupled substitution of $Al^{3+} + H^+$ for Si^{4+}.

The present data do not allow to separate the effect of H^+ and Al^{3+} on the bulk modulus. However, high water fugacities will cause some additional dissolution of the $CaMg(AlH)SiO_6$ component in the clinopyroxene in addition to Tschermak's component. Therefore, the effect of tetrahedral Al and of H on the bulk modulus will always be coupled to each other in Earth's mantle. Whether the incorporation of water in aluminous orthopyroxene also increases bulk modulus is still unclear due to the lack of experimental data. However, if orthopyroxene and clinopyroxene behave in the same way, detecting small amounts of water in the upper mantle from measurements of seismic velocities will be nearly impossible. In particular in the upper mantle, most of the water would partition into pyroxenes. The increase of the bulk modulus of the pyroxene by the coupled substitution of Al + H for Si would possibly mostly cancel out with the softening of olivine due to the creation of protonated Mg vacancies.
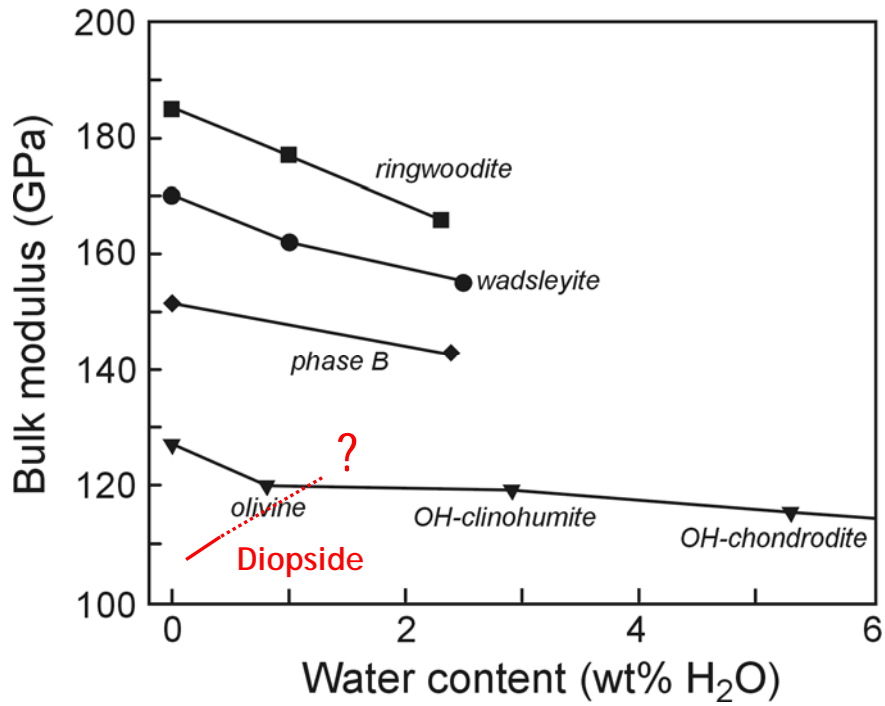
Figure 4.3-1. Plot of bulk modulus against water content for various nominally anhydrous minerals (redrawn from Jacobsen, 2006). The data of bulk modulus for hydrous both pure and Al-bearing diopside from this study are added to the plot.

5. CONCLUSIONS

The experimental results from this study suggest the following conclusions:

1. Water solubility in pure diopside varies from 63 up to 728 ppm H_2O measured from the crystals synthesized at 25 kbar and 1100^oC and 30 kbar and 1000^oC respectively. The pressure and temperature dependence of water solubility in pure diopside shows the following behavior: the water solubility at 30 kbar increases from 700 to 1000^oC and above 1000^oC it drops again; at 900^oC, water solubility first increases with pressure up to 25 kbar and then strongly decreases towards higher pressures

2. Different types of infrared spectra were observed for pure hydrous diopside. They indicate different mechanisms of hydrogen incorporation in diopside and depend on the activities of different components in the system during crystallization. The infrared spectra with one main absorption band at 3650 cm^{-1} (Type I) yield the first mechanism of hydroxyl incorporation, which involves a defect in Si on the tetrahedral site. The spectra with several absorption bands from 3480 to 3280 cm^{-1} or only one band at 3357 cm^{-1} (Type II) correspond to a second mechanism with a defect in the Mg or Ca octahedral site.

4. Water solubility strongly increases with the presence of Al in diopside up to 2591 ppm H_2O for diopside containing 8.37 wt.% of Al_2O_3 and synthesized at 25 kbar and 1100^oC.

5. The main mechanism for hydroxyl incorporation in Al-bearing diopside is the substitution of Si in the tetrahedral position by Al and protonation of one oxygen atom.

6. Water solubility in Al-bearing diopside increases with decreasing temperature.

7. High-pressure single crystal diffraction experiments on both hydrous and dry diopside crystals show that hydroxyl incorporation in diopside by the substitution $Si^{4+} = Al^{3+} + H^+$ increases the stiffness of diopside.

8. From the refinement of crystal structures of both hydrous and dry diopside it is possible to see the influence of protonation of certain oxygen atoms. For example, the comparison of the crystals

structures of four diopside samples from this study and the anhydrous Ca-Tschermak's pyroxene show deviations from the linear correlation between the bond lengths in *M1* octahedra and *T* tetrahedral sites.

9. Clinopyroxene is not a significant host of water in the deeper part of the upper mantle. However, in the upper mantle, most of the water is concentrated in the pyroxenes. Moreover, omphacite is able to transport large amounts of water into the mantle during subduction and probably influences the global sea level.

6. REFERENCES

Angel R.J. (2000) Equation of state. In: Hazen R.M., Downs R.T. (eds.) High-temperature and high-pressure crystal chemistry. Reviews in Mineralogy and Geochemistry, Vol. 41. Mineralogical Society of America and Geochemical Society, Washington, DC. 35-60.

Angel R.J. (2002) EOSFIT V5.2. Crystallography Laboratory. Department of Geosciences, Virginia Tech, USA.

Angel R.J., Downs R.T., Finger L.W. (2000) High-temperature and high-pressure diffractometry. In: Hazen R.M., Downs R.T. (eds.) High-temperature and high-pressure crystal chemistry. Reviews in Mineralogy and Geochemistry, Vol. 41. Mineralogical Society of America and Geochemical Society, Washington, DC. 559-596.

Aubaud C., Hauri E.H., Hirschmann M.M. (2004) Hydrogen partition coefficients between nominally anhydrous minerals and basaltic melts. *Geophys. Res. Lett.* **31(5)**. L20611. doi:10.1029/ 2004GL021341.

Bai Q., Kohlstedt D.L. (1993) Effect of chemical environment on the solubility and incorporation mechanism for hydrogen in olivine. *Phys. Chem. Minerals*. **19**. 460-471.

Bell D.R., Ihinger P.D, Rossman G.R. (1995) Quantitative analysis of trace OH in garnet and pyroxenes. *Amer. Miner.* **80**. 465-474.

Bell D.R., Rossman G.R. (1992) Water in the Earth's mantle: the role of nominally anhydrous minerals. *Science.* **255**. 1391-1397.

Bell D.R., Rossman G.R., Moore R.O. (2004) Abundance and partitioning of OH in a high-pressure magmatic system: megacrysts from the Monastery kimberlite, South Africa. *Journal of Petrology*. **45**. 1539-1564.

Berhorst A., Flueh E.R., McIntosh K.D., Ranero C.R., Ahmed I., Silver E.A., Barckhausen U. (2003) The crustal structure of the convergent Nicaraguan margin from a combined reflection and refraction study. *Geophys. Res. Abstr*. **5**. 09692.

Best M.G. (2003) Generation of magma. Chapter 11 – In: Igneous and metamorphic petrology – 2nd ed. 283-315.

Blanchard M., Ingrin J. (2004) Hydrogen diffusion in Dora Maira pyrope. *Phys. Chem. Minerals*. **31**. 593-605.

Boffa-Ballaran T., Carpenter M.A., Domeneghetti M.C., Tazzoli V. (1998) Structural mechanisms of solid solution and cation ordering in augite-jadeite pyroxenes: I. A macroscopic perspective. *Am. Miner*. **83**. 419-433.

Bohlen S.R., Boettcher A.L. (1982) The quartz-coesite transformation: a precise determination and the effect of other components. *Journal Geoph. Res*. **87 (B)**. 7073-7078.

Bolfan-Casanova N. (2000a) The distribution of water in the Earth's mantle: an experimental and infrared study. Ph.D. thesis, Bayerisches Geoinstitut, Universität Bayreuth.

Bolfan-Casanova N. (2005) Water in the Earth's mantle. *Mineral. Magaz*. **69 (3)**. 229-257.

Bolfan-Casanova N., Keppler H., Rubie D.C. (2000b) Water partitioning between nominally anhydrous minerals in the MgO-SiO_2-H_2O system up to 24 GPa: Implications for the distribution of water in the Earth's mantle. *Earth Planet. Sci. Lett.* **182**. 209-221.

Bolfan-Casanova N., Keppler H., Rubie D.C. (2003) Water partitioning at 660 km depth and evidence for very low water solubility in magnesium silicate perovskite. *Geophys. Res. Lett.* **30(17)**. SDE-3.

Bolfan-Casanova N., Mackwell S., Keppler H., McCammon C.A., Rubie D.C. (2002) Pressure dependence of H solubility in magnesiowustite up to 25 GPa: Implications for the storage of water in the Earth's lower mantle. *Geophys. Res. Lett.* **29(10)**. 89.

Boss A.P. (1998) Temperatures in protoplanetary disks. *Annual Reviews of Earth and Planetary Science*. **26**. 26-53.

Boyd F.R., England J.L. (1960) Apparatus for phase-equilibrium measurements at pressures up to 50 kilobars and temperatures up to 1750°C. *Journal Geoph. Res*. **65 (2)**. 741-748.

Bromiley G.D., Keppler H. (2004) An experimental investigation of hydroxyl solubility in jadeite and Na-rich clinopyroxenes. *Contrib. Mineral. Petrol.* **147**. 189-200.

Bromiley G.D., Keppler H., McCammon C., Bromiley F., Jacobsen S.D. (2004) Hydrogen solubility and speciation in natural, gem-quality chromian diopside. *Amer. Miner.* **89**. 941-949.

Bromiley G.D., Pawley A. (2002) The high-pressure stability of Mg-sursassite in a model hydrous peridotite: a possible mechanism for the deep subduction of significant volumes of H_2O. *Contrib. Mineral. Petrol.* **142**. 714-723.

Bruno E., Carbonin S., Molin G.M. (1982) Crystal structures of Ca-rich clinopyroxenes in the $CaMgSi_2O_6 - Mg_2Si_2O_6$ join. *Tschermaks Mineral. Petrogr. Mitt.* **29**. 223-240.

Cameron M., Papike J.J. (1980) Crystal chemistry of silicate pyroxenes. *Reviews in Mineralogy and Geochemistry*. Vol. 7. 5-92

Carpenter Woods S., Mackwell S., Dyar D. (2000) Hydrogen in diopside: diffusion profiles. *Amer. Miner.* **85**. 480-487.

Chopra P.N., Paterson M.S. (1984) The role of water in the deformation of dunite. *Journal Geoph. Res*. **89 (B)**. 7861-7876.

Clark J.R. and Papike J.J. (1968) Crystal chemical characterization of omphacites. *Amer. Miner.* **53**. 840-868.

Coleman R.G., Lee D.E., Beatty L.B., Brannock W.W. (1965) Eclogites and eclogites: their differences and similarities. *Geol. Soc. Amer Bull.* **76**. 483-508.

Dal Negro A., Carbonin S., Salviulo G., Piccirillo E.M., Cundari A. (1985) Crystal chemistry and site configuration of the clinopyroxene from leucite-bearing rocks and related genetic significance: the Sabatini lavas, Roman region, Italy. *Jour. Petrology*. **26**.1027-1040.

Dal Negro A., Cundari A., Piccirillo E.M., Molin G.M., Uliana D. (1986) Distinctive crystal chemistry and site configuration of the clinopyroxene from alkali basaltic rocks. *Contrib. Mineral. Petrol.* **92**. 35-43.

Demouchy S., Jacobsen S.D., Gaillard F., Stern C.R. (2006) Rapid magma ascent recorded by water diffusion profiles in mantle olivine. *Geology*. **34 (6)**. 429-432.

Drake M.J. (2005) Origin of water in the terrestrial planets. *Meteorit. Planet. Sci*. **40**. 519-527.

Eide E.A., Liou J.G. (2000) High-pressure blueschists and eclogites in Hong'an: a framework for addressing the evolution of high- and ultrahigh-pressure rocks in central China. *Lithos*. **52**. 1-22.

Eriksson P.G. (1999) Sea level changes and the continental freeboard concept: general principles and application to the Precambrian. *Precambrian Res*. **97**. 143-154.

6. References

Frese K., Trommsdorff V., Kunze K. (2003) Olivine [100] normal to foliation: lattice preferred orientation in prograde garnet peridotite formed at high H_2O activity, Cima di Gagnone (Central Alps). *Contrib. Mineral. Petrol.* **145**. 75-86.

Frost D. (2003) The structure and sharpness of $(Mg,Fe)_2SiO_4$ phase transformations in the transition zone. *Earth Planet. Sci. Lett.* **216**. 313-328.

Frost D.J., Poe B.T., Tronnes R.G. Liebske C., Duba A., Rubie D.C. (2004) A new large-volume multianvil system. *Phys. Earth Planet. Inter.* **143-144**. 507-514.

Fumagalli P., Stixrude L., Poli S., Snyder D. (2001) The 10 Å phase: a high-pressure expandable sheet silicate stable during subduction of hydrated lithosphere. *Earth Planet. Sci. Lett.* **186**. 125-141.

Gasparik T. (2003) Phase diagrams for geoscientists: an atlas of the Earth's interior. Springer – Verlag Berlin Heidelberg. 131-213.

Gatzemeier A., Wright K. (2006) Computer modeling of hydrogen defects in the clinopyroxenes diopside and jadeite. *Phys. Chem. Minerals*. **33**. 115-125.

Giacomoni F., Bomparola R.M., Ghezzo C. (2005) Petrology and geochronology of metabasites with eclogite facies relics NE Sardinia: constraints for the Palaeozoic evolution of Southern Europe. *Lithos.* **82**. 221-248.

Green D.H. (1973) Experimental melting studies on a model upper mantle composition at high pressure under water-saturated and water-undersaturated conditions. *Earth Planet. Sci. Lett.* **19**. 37-53.

Gurnis M. (1990) Ridge spreading, subduction, and sea level fluctuations. *Science*. **250**. 970-972.

Hall A. (1996) Igneous petrology. Longman group Limited. 2nd edition. 289-294.

Hallam A. (1992) Phanerozoic sea-level changes. Columbia Univ. Press. 266 pp.

Hallam A., Wignall P.B. (1999) Mass extinctions and sea-level changes. *Earth-Sci. Rew*. **48**. 217-250.

Hays J.D., Pitman III W.C. (1973) Lithospheric plate motion, sea level changes and climatic and ecological consequences. *Nature*. **246**. 18-22.

Hazen R.M., Finger L.W. (1977) Compressibility and structure of Angra dos Reis fassaite to 52 kbar. Carnegie Inst. Wash. Yrbk. 76. 512-515.

Hercule S., Ingrin J. (1999) Hydrogen in diopside: diffusion, kinetics of extraction-incorporation, and solubility. *Amer. Miner.* **84**. 1577-1587.

Hirth G., Kohlstedt D.L. (1996) Water in the oceanic upper mantle: implications for rheology melt extraction and the evolution of the lithosphere. *Earth Planet. Sci. Lett.* **144**. 93-108.

Hirose K., Kawamoto T. (1995) Hydrous partial melting of lherzolite at 1 GPa: the effect of H_2O on the genesis of basaltic magmas. *Earth Planet. Sci. Lett.* 133. 463-473.

Holland T., Powell R. (1998) An internally consistent thermodynamic dataset for phases of petrological interest. *Jour. of Metamorph. Geol*. **16**. 309.
or http://rock.esc.cam.ac.uk/astaff/holland/ds5/gases/H2O.html

Ingrin J., Latrous K., Doukhan J.-C., Doukhan N. (1989) Water in diopside: an electron microscopy and infrared spectroscopy study. *Eur. J. Minerals*. **1**. 327-341.

Ingrin J., Hercule S., Charton T. (1995) Diffusion of hydrogen in diopside: Results of dehydration experiments. *Journal Geoph. Res*. **100 (B8)**. 15489-15499.

Ingrin J., Skogby H. (2000) Hydrogen in nominally anhydrous upper-mantle minerals: concentrations levels and implications. *Eur. J. Minerals*. **12**. 543-570.

Inoue T. (1994) Effect of water on melting phase relations and melt composition in the system Mg_2SiO_4—$MgSiO_3$—H_2O up to 15 GPa. *Phys. Earth Planet. Inter*. **85**. 237-263.

Ibers J.A., Hamilton W.C., Eds. (1974) International Tables for X-ray Crystallography, IV, p. 99.101. Kynoch Press, Birmingham, U.K.

Ito E., Harris D.M., Anderson A.T. (1983) Alteration of oceanic crust and geologic cycling of chlorine and water. *Geoch. Cosmochim. Acta.* **47**. 1613-1624.

Jacobsen S.D. (2006) Effect of water on the equation of state of nominally anhydrous minerals. Reviews in Mineralogy and Geochemistry, Vol. 62. Mineralogical Society of America. 321-342.

Jung H., Karato S. (2001) Water-induced fabric transitions in olivine. *Science*. **293**. 1460-1463.

Jung H., Katayama I., Jiang Z., Hiraga T., Karato S. (2006) Effect of water and stress on the lattice-preferred orientation of olivine. *Tectonophysics*. **421**. 1-22.

Karato S. (1990) The role of hydrogen in the electrical conductivity of the upper mantle. *Nature*. **347**. 272-273.

Karato S. (1995) Effect of water on seismic wave velocities in the upper mante. *Proc. Japan Acad.* **71**. ser. B. 61-65.

Karato S. (2006) Remote sensing of hydrogen in Earth's mantle. Reviews in Mineralogy and Geochemistry, Vol. 62. Mineralogical Society of America. 343-375.

Karato S., Jung H. (1998) Water, partial melting and the origin of the seismic low velocity and high attenuation zone in the upper mantle. *Earth Planet. Sci. Lett.* **157**. 193-207.

Karato S., Paterson M.S., FitzGerald J.D. (1986) Rheology of synthetic olivine aggregates: influence of grain size and water. *Journal Geoph. Res*. **91 (B)**. 8151-8176.

Katayama I., Nakashima S., Yurimoto H. (2006) Water content in natural eclogite and implication for water transport into the deep upper mantle. *Lithos*. **86**. 245-259.

Kawai N., Endo S. (1970) The generation of ultrahigh hydrostatic pressures by split sphere apparatus. *Rev. Sci. Instrum*. **41**. 1178-1181.

Kawamoto T. (2006) Hydrous phases and water transport in the subducting slab. *In*: Reviews in Mineralogy & Geochemistry. **62**. *Water in nominally anhydrous minerals*. pp. 273-289.

Kawata S. (2002) Instrumentation for near-infrared spectroscopy. In: *Near-infrared spectroscopy principles, instruments, applications*. Ed. Siesler H.W., Ozaki Y., Kawata S., Heise H.M. Chapter 3.

King H.E., Finger L.W. (1979) Diffracted beam crystal centering and its application to high-pressure crystallography. *Journal Appl. Cryst*. **12**. 374-378.

Koch-Müller M., Matsyuk S.S., Wirth R. (2004) Hydroxyl in omphacites and omphacitic clinopyroxenes of upper mantle to lower crustal origin beneath the Siberian platform. *Amer. Miner.* **89**. 921-931.

Koch-Müller M., Matsyuk S.S., Rhede D., Wirth R., Khisina N. (2006) Hydroxyl in mantle olivine xenocrysts from the Udachnaya kimberlite pipe. *Phys. Chem. Minerals*. **33**. 276-287.

Kohlstedt D.L., Keppler H., Rubie D.C. (1996) Solubility of water in the α, β and γ phases of $(Mg,Fe)_2SiO_4$. *Contrib. Mineral. Petrol.* **123**. 345-357.

Krogh Ravna E.J., Paquin J. (2003) Thermobarometric methodologies applicable to eclogites and garnet ultrabasites. In: EMU notes in Mineralogy. Vol. 5. Chapter 8. 229-259.

6. References

Kushiro I. (1972) Effect of water on the composition of magmas formed at high pressures. *Journal of Petrology*. **13**. 311-334.

Larson A.C, Von Dreele R.B. (1994) GSAS General Structure Analysis System. Los Alamos National Laboratory, New Mexico, USA.

Levien L., Prewitt C.T. (1981) High-pressure structural study of diopside. *Amer. Miner.* **66**. 315-323.

Libowitzky E. (1999) Correlation of O-H stretching frequencies and O-H…O hydrogen bond lengths in minerals. *Monatshefte für Chemie.* **130**. 1047-1059.

Libowitzky E., Beran A. (2004) IR spectroscopic characterisation of hydrous species in minerals. In: *EMU notes in mineralogy*. Vol. 6, chapter 6. 227-279.

Libowitzky E., Rossman G.R. (1996) Principles of quantitative absorbance measurements in anisotropic crystals. *Phys. Chem. Minerals*. **23**. 319-327.

Libowitzky E., Rossman G.R. (1997) An IR absorption calibration for water on minerals. *Amer. Miner.* **82**. 1111-1115.

Long M.D., van der Hilst R.D. (2005) Upper mantle anisotropy beneath Japan from shear wave splitting. *Earth Planet. Sci. Lett.* **151**. 206-222.

Lu R., Keppler H. (1997) Water solubility in pyrope to 100 kbar. *Contrib. Mineral. Petrol.* **129**. 35-42.

Maaløe S., Aoki K. (1977) The major element composition of the upper mantle from the composition of Lherzolites. *Contrib. Mineral. Petrol.* **63**. 161-173.

Mackwell S.J., Kohlstedt D.L. (1990) Diffusion of hydrogen in olivine: Implications for water in the mantle. *Journal Geoph. Res*. **95 (B4)**. 5079-5088.

Mainprice D., Silver P.G. (1993) Interpretation of SKS-waves using samples from the subcontinental lithosphere. *Phys. Earth Planet. Inter.* **78**. 257-280.

Manoli S., Molin G.M. (1988) Crystallographic procedures in the study experimental rocks: X-ray single-crystal structure refinement of *C*2/*c* clinopyroxene from lunar 74275 high-pressure experimental basalt. *Mineral. Petrol.* **39**. 187-200.

Mao H.K., Xu J., Bell P.M. (1986) Calibration of the ruby pressure gauge to 800 kbar under quasi-hydrostatic conditions. *Journal Geoph. Res*. **91 (B)**. 4673-4676.

Marty B., Yokochi R. (2006) Water in the early Earth. Reviews in Mineralogy and Geochemistry, Vol. 62. Mineralogical Society of America. 421-450.

Matsyuk S.S., Langer K. (2004) Hydroxyl in olivines from mantle xenoliths in kimberlites of the Siberian platform. *Contrib. Mineral. Petrol.* **147**. 413-437.

Matsyuk S.S., Langer K., Hösch A. (1998) Hydroxyl defects in garnet from mantle xenoliths in kimberlites of the Siberian platform. *Contrib. Mineral. Petrol.* **132**. 163-179.

McCormick T.C., Hazen R.M., Angel R.J. (1989) Compressibility of omphacite to 60 kbar: Role of vacancies. *Am. Mineral.* **74**. 1287-1292.

Meade C., Reffner J.A., Ito E. (1994) Synchrotron infrared absorbance measurements of hydrogen in $MgSiO_3$ perovskite. *Science*. **264**. 1558-1560.

Mierdel K., Keppler H. (2004) The temperature dependence of water solubility in enstatite. *Contrib. Mineral. Petrol.* **148**. 305-311.

Mierdel K. (2006) Wasserlöslichkeit in Enstatit. Ph.D. thesis, University of Tübingen.

Mierdel K., Keppler H., Smyth J., Langenhorst F. (2007) Water solubility in aluminous orthopyroxene and the origin of Earth's asthenosphere. *Science.* **315**. 364-368.

Miletich R., Allan D.R., Kuhs W.F. (2000) High-pressure single-crystal techniques. In: Hazen R.M., Downs R.T. (eds.) High-temperature and high-pressure crystal chemistry. Reviews in Mineralogy and Geochemistry, Vol. 41. Mineralogical Society of America and Geochemical Society, Washington, DC. 445-519.

Miller K.G., Kominz M.A., Browning J.V., Wright J.D., Mountain G.S., Katz M.E., Sugarman P.J., Cramer B.S., Christie-Blick N., Pekar S.F. (2005) The Phanerozoic record of global sea-level change. *Science*. **310**. 1293-1298.

Mizukami T., Wallis S.R., Yamamoto J. (2004) Natural examples of olivine lattice preferred orientation patterns with a flow-normal *a*-axis maximum. *Nature*. **427**. 432-436.

Morimoto N. (1988) Nomenclature of pyroxenes. *Mineral. Magaz.* **52**. 535-550.

Mosenfelder J.L., Deligne N.I., Asimow P.D., Rossman G.R. (2006) Hydrogen incorporation in olivine from 2-12 GPa. *Amer. Miner.* **91**. 285-294.

Morishima H., Kato T., Suto M., Ohtani E., Urakawa S., Utsumi W., Shimomura S., Kikegawa T. (1994) The phase boundary between α and β-Mg_2SiO_4 determined by in situ X-ray observation. *Science*. **265**. 1202-1203.

Murakami M., Hirose K., Yurimoto H., Nakashima S., Takafuji N. (2002) Water in Earth's lower mantle. *Science*. **295**. 1885-1887.

Nakajima J., Hasegawa A. (2004) Shear-wave polarization anisotropy and subduction-unduced flow in the mantle wedge of northeastern Japan. *Earth Planet. Sci. Lett.* **225**. 365-377.

Nestola F., Ballaran T., Tribaudino M., Ohashi H. (2005) Compressional behavior of $CaNiSi_2O_6$ clinopyroxene: bulk modulus systematic and cation type in clinopyroxenes. *Phys. Chem. Mineral.* **32**. 222-227.

Nestola F., Boffa Ballaran T., Liebske C., Bruno M., Tribaudino M. (2006a) High-pressure behavior along the jadeite $NaAlSi_2O_6$-aegirine $NaFeSi_2O_6$ solid solution up to 10 GPa. *Phys. Chem. Minerals*. **33**. 417–425.

Nestola F., Gatta G.D., Boffa Ballaran T. (2006b) The effect of Ca substitution on the elastic and structural behavior of orthoenstatite. *Am. Miner.* **91**. 809-815.

Nestola F., Boffa Ballaran T., Liebske C., Thompson R.M., Down R.T. (2008) The effect of the hedenbergite substitution on the compressibility of jadeite. *Am. Miner.* In press.

Newell N.D. (1967) Revolutions in the history of life. *Geol.Soc.Am., Spec. Pap*. **89**. 63-91.

Nicolas A., Christensen N.I. (1987) Formation of anisotropy in upper mantle peridotites — a review, in: Fuchs K., Froidevaux C. (Eds.), Composition, Structure and Dynamics of the Lithosphere–Asthenosphere System, Am. Geophys.Union, Washington, D.C. pp. 111–123.

Nixon P.H. (1987) Mantle xenoliths. New York, John Wiley and sons press.

Nowlan E.U., Schertl H.-P., Schreyer W. (2000) Garnet-omphacite-phengite thermobarometry of eclogites from the coesite-bearing unit of the southern Dora-Maira Massif, Western Alps. *Lithos*. **52**. 197-214

Nutman A.P. (2006) Antiquity of the oceans and continents. *Elements*. **2**. 223-227.

Oberti R., Caporuscio F.A. (1991) Crystal chemistry of clinopyroxenes from mantle eclogites: a study of the key role of the M2 site population by means of crystal-structure refinement. *Am. Miner*. **76**. 1141-1152.

Okamura F.P., Ghose S., Ohashi H. (1974) Structure and crystal chemistry of calcium Tschermak's pyroxene, CaAlAlSiO$_6$. *Am. Miner.* **59**. 549-557.

Oxford Diffraction (2006). Oxford Diffraction Ltd., Xcalibur CCD system, CrysAlis Software system, Version 171.30.2

Paterson M.S. (1982) The determination of hydroxyl by infrared absorption in quartz, silicate glasses and similar materials. *Bull. Mineral.* **105**. 20-29.

Peacock S.M. (1990) Fluid process in subduction zones. *Science.* **248**. 329-337.

Peacock S.M. (1996) Thermal and petrologic structure of subduction zones. *in* Subduction: Top to Bottom, (eds.) Bebout E. *et al.*, *Geophys. Monogr. Series.* **98**. pp. 119-135. AGU, Washington DC.

Peacock S.M. (2000) Thermal structure and metamorphic evolution of subducting slabs. In: Eiler, J.M. (Ed.), Inside the Subduction Factory. Geophysical Monograph Ser. American Geophysical Union, Washington, DC, pp. 7–22.

Peslier A.H., Luhr J.F., Post J. (2002) Low water contents in pyroxenes from spinel-peridotites of oxidized, sub-arc mantle wedge. *Earth Planet. Sci. Lett.* **201**. 69-86.

Plank T., Langmuir C.H. (1998) The chemical composition of subducting sediment and its consequences for the crust and mantle. *Chem. Geology.* **145**. 325-394.

Poirier J.-P. (2000) Introduction to the physics of the Earth's interior. Chapter 4 – Equation of state. 2nd edition. Cambridge Univ. Press.

Prencipe M, Tribaudino M., Pavese A., Hoser A., Reehuis M. (2000). A single-crystal neutron-diffraction investigation of diopside at 10 K. *Canad. Miner.* **38**. 183-189.

Ragland P. C. (1989) Basic analytical petrology. Oxford university press. 51-52.

Ranero C.R., Phipps Morgan J., McIntosh K., Reichert C. (2003) Bending-related faulting and mantle serpentinization at the Middle America trench. *Nature.* **425**. 367-373.

Rauch M., Keppler H. (2002) Water solubility in orthopyroxene. *Contrib. Mineral. Petrol.* **143**. 525-536.

Reading H.G., Levell B.K. (1996) Controls on the sedimentary rock record. In: reading H.G. (Ed.), Sedimentary environments: Processes facies and stratigraphy. Blackwell, Oxford, pp. 5-36.

6. References

Rossi G., Smith D.C., Ungaretti L., Domeneghetti M.C. (1983) Crystal-chemistry and cation ordering in the system diopside-jadeite: a detailed study by crystal structure refinement. *Contrib. Miner. Petrol*. **83**. 247-258.

Rossi G., Oberti R., Dal Negro A., Molin G.M., Mellini M. (1987) Residual electron density at the *M2* site in *C2/c* clinopyroxenes: Relationships with bulk chemistry and sub-solidus evolution. *Phys. Chem. Minerals*. **14**. 514-520.

Rubie D.C. (1999) Characterising the sample environment in multianvil high-pressure experiments. *Phase Transitions*. **68**. 431-451.

Rüpke L.H., Morgan J.P., Hort M., Connoly J.A.D. (2004) Serpentine and the subduction zone water cycle. *Earth Planet. Sci. Lett.* **223**. 17-34.

Saal A.E., Hauri E.H., Langmuir C.H., Perfit M.R. (2002) Vapour undersaturation in primitive mid-ocean-ridge basalt and the volatile content of Earth's upper mantle. *Nature*. **419**. 451-455.

Sallares V., Ranero C.R. (2003) Structure of the incoming ocean plate and the erosional convergent margin off Antofagasta, northern Chile. *Geophys. Res. Abstr*. **5**. 02839.

Sheldrick G.M. (1977) SHELX97. *Program for the refinement of crystal structures*. Univ of Göttingen, Germany,

Schmerr N., Garnero E.J. (2007) Upper mantle discontinuity topography from thermal and chemical heterogeneity. *Science*. **318**. 623-626.

Schmidt M. (1993) Phase-relations and compositions in tonalite as a function of pressure – an experimental study at $650^{o}C$. *Am. Journ. Sci*. **10**. 1011-1060.

Schmidt M.W., Poli S. (1998) Experimentally based water budgets for dehydrating slab and consequences for arc magma generation. *Earth Planet. Sci. Lett.* **163**. 361-379.

Skogby H. (1994) OH incorporation in synthetic clinopyroxene. *Amer. Miner*. **79**. 240-249.

Skogby H. (2006) Water in natural mantle minerals I: Pyroxenes. Reviews in Mineralogy and Geochemistry, Vol. 62. Mineralogical Society of America. 155-167.

Skogby H., Bell D.R., Rossman G.R. (1990) Hydroxide in pyroxene: variations in the natural environment. *Amer. Miner*. **75**. 764-774.

Smith G.P., Wiens D.A., Fischer K.M., Dorman L.M., Webb S.C., Hildebrand J.A. (2001) A complex Pattern of mantle flow in the Lau backarc. *Science*. **292**. 713-716.

Smulikowski K. (1968) Differentiation of eclogites and its possible causes. *Lithos*. **1**. 89-101.

Smyth J. (1980) Cation vacancies and the crystal chemistry of breakdown reactions in kimberlitic omphacites. *Amer. Miner.* **65**. 1185-1191.

Smyth J. (1987) β-Mg$_2$SiO$_4$: A potential host for water in the mantle? *Amer. Miner.* **72**. 1051-1055.

Smyth J., Bell D., Rossman G. (1991) Incorporation of hydroxyl in upper-mantle clinopyroxenes. *Nature*. **351**. 732-735.

Smyth J., Frost D. (2002) The effect of water on the 410-km discontinuity: an experimental study. *Geophys. Res. Lett.* **29(10)**. 123.

Sobolev A.V., Chaussidon M. (1996) H$_2$O concentrations in primary melts from supra-subduction zones and mid-ocean ridges: implications for H$_2$O storage and recycling in the mantle. *Earth Planet. Sci. Lett.* **137**. 45-55.

Stalder R., Ludwig T. (2007) OH incorporation in synthetic diopside. *Eur. J. Mineral.* **19**. 373-380.

Stalder R., Skogby H. (2002) Hydrogen incorporation in enstatite. *Eur. J. Mineral.* **14**. 1139-1144.

Stoyanov E. (2006) Valence state, coordination and incorporation of Ti and Cr into lower mantle phases: new insight from electron energy-loss spectroscopy. Ph.D. thesis, University of Jena.

Suzuki A., Ohtani E., Morishima E., Kubo T., Kanbe Y., Kondo T. (2000) In situ determination of the phase boundary between wadsleyite and ringwoodite in Mg$_2$SiO$_4$. *Geophys. Res. Lett.* **27(6)**. 803-806.

Tarits P., Hautot S., Perrier F. (2004) Water in the mantle: results from electrical conductivity beneath the French Alps. *Geophys. Res. Lett.* **31**. L06612.

Thompson R.M., Downs R.T., Redhammer G.J. (2005) Model pyroxenes III: volume of *C*2/*c* pyroxenes at mantle *P*, *T*, and *x*. *Amer. Miner.* **90**. 1840-1851.

Tobi B.H. (2001) EXPGUI, a graphical user interface for GSAS. *J. Appl. Cryst.* **34**. 210-213.

Tribaudino M., Prencipe M., Bruno M., Levy D. (2000) High-pressure behavior of Ca-rich *C*2/*c* clinopyroxenes along the join diopside-enstatite. *Phys. Chem. Mineral.* **27**. 656-664.

Turcotte D.L., Schubert G. (2002) Geodynamics. Cambridge University Press, 2nd edition.

van der Meijde M., Marone F., Giardini D., van der Lee S. (2003) Seismic evidence for water deep in Earth's upper mantle. *Science.* **300**. 1556-1558.

Wallmann K. (2001) The geological water cycle and the evolution of marine $\delta^{18}O$ values. *Geoch. Cosmochim. Acta.* **65**. 2469-2485.

Wang L., Zhang Y., Essene E. (1996) Diffusion of the hydrous component in pyrope. *Amer. Miner.* **81**. 706-718.

Wang D., Mookherjee M., Xu Y., Karato S. (2006) The effect of water on the electrical conductivity of olivine. *Nature.* **443**. 977-980.

White A.J.R. (1964) Clinopyroxenes from eclogites and basic granulites. *Amer. Miner.* **49**. 883-888.

Wood B.J. (1995) The effect of H_2O on the 410-kilometer seismic discontinuity. *Science.* **268**. 74-76.

Yoshino T., Matsuzaki T., Yamashita S., Katsura T. (2006) Hydrous olivine unable to account for conductivity anomaly at the top of the asthenosphere. *Nature*. **443**. 973-976.

Young T.E., Green H.W., Hofmeister A.M., Walker D. (1993) Infrared spectroscopic investigation of hydroxyl in β-$(Mg,Fe)_2SiO_4$ and coexisting olivine: implications for mantle evolution and dynamics. *Phys. Chem. Minerals*. **19**. 409-422.

Zhang J., Li B., Utsumi W., Liebermann R.C (1996) In situ X-ray observations of the coesite-stishovite transition: reversed phase boundary and kineticts. *Phys. Chem. Minerals*. **23**. 1-10.

Zhang L., Ahsbans H., Hafner S.S., Kutoglu A. (1997) Single-crystal compression and crystal structure of clinopyroxene up to 10 GPa. *Amer. Miner.* **82**. 245-258.

Zhang R.Y., Xu Z., Xu H. (2000) Petrology of ultrahigh-pressure eclogite from ZK703 drillhole in the Donghai, east China. *Lithos*. **52**. 35-50.
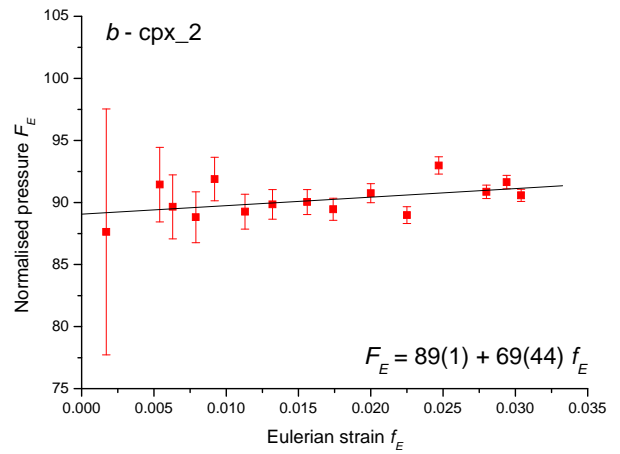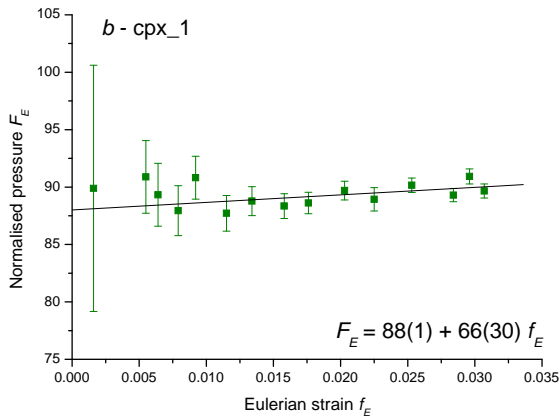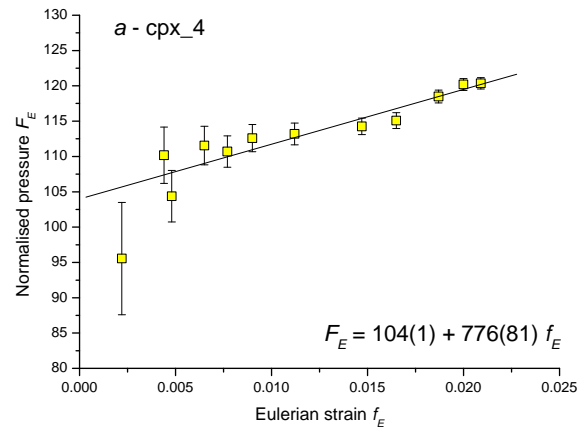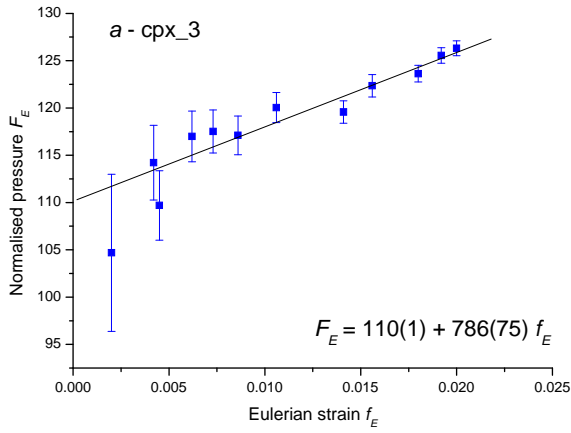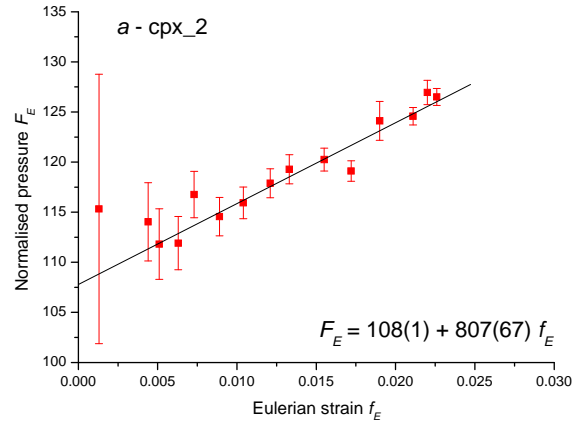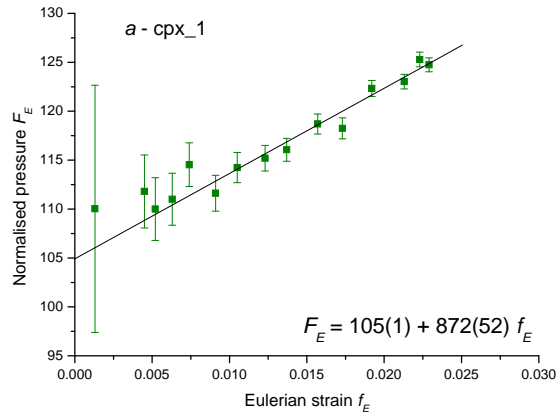
Appendix 1. *Microprobe analyses for pure diopside (in wt.% for oxides and in a.p.f.u. for cations)*

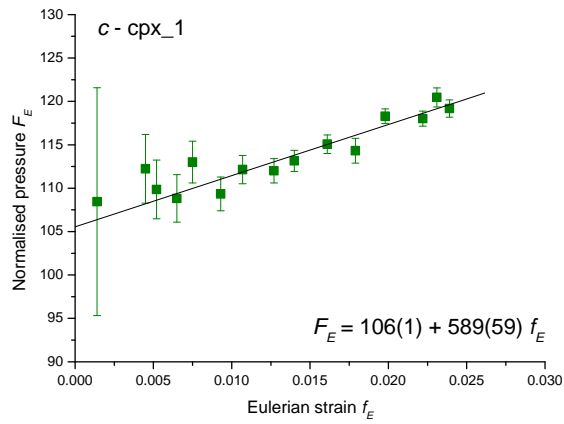| run	T (°C)	P (kbar)	H₂O (ppm)	Type of spectra	SiO₂	Al₂O₃	MgO	CaO	Sum	Si	Al	Mg	Ca	Cation sum
# MP-2	1100	100	300	I	55.87 ± 0.22	0.41 ± 0.13	18.69 ± 0.13	25.53 ± 0.12	100.50 ± 0.25	2.00 ± 0.005	0.02 ± 0.005	1.00 ± 0.007	0.98 ± 0.004	3.99 ± 0.01
# MP-1	1000	100	138	I	55.99 ± 0.37	0.05 ± 0.08	18.13 ± 0.19	27.71 ± 0.28	101.88 ± 0.69	1.99 ± 0.003	0.002 ± 0.003	0.96 ± 0.01	1.06 ± 0.01	4.01 ± 0.01
# 4	1100	30	201	II	56.08 ± 0.24	0.02 ± 0.01	20.11 ± 0.50	24.22 ± 0.53	100.42 ± 0.34	2.00 ± 0.01	0.0007 ± 0.0020	1.07 ± 0.09	0.93 ± 0.09	4.00 ± 0.01
# 24	1000	30	728	II	55.82 ± 0.52	0.25 ± 0.11	18.65 ± 0.33	25.57 ± 0.30	100.29 ± 0.82	2.00 ± 0.02	0.01 ± 0.02	1.00 ± 0.05	0.98 ± 0.05	3.99 ± 0.02
# 21	900	30	397	I	57.10 ± 0.28	0.37 ± 0.18	18.19 ± 0.11	28.00 ± 0.14	102.69 ± 0.28	1.98 ± 0.03	0.02 ± 0.03	0.96 ± 0.02	1.06 ± 0.02	4.01 ± 0.02
# 22	800	30	208	I	55.91 ± 0.42	0.25 ± 0.12	18.17 ± 0.25	27.97 ± 0.32	102.31 ± 0.37	1.98 ± 0.03	0.04 ± 0.02	0.96 ± 0.05	1.06 ± 0.06	4.01 ± 0.03
# 17	1100	25	63	I	55.04 ± 0.18	0.03 ± 0.01	18.69 ± 0.11	25.42 ± 0.17	99.17 ± 0.21	2.00 ± 0.01	0.002 ± 0.002	1.01 ± 0.02	0.99 ± 0.03	4.00 ± 0.01
# 20	1000	25	166	II	55.37 ± 0.37	0.07 ± 0.02	19.07 ± 1.16	24.72 ± 1.79	99.28 ± 0.39	2.00 ± 0.003	0.003 ± 0.001	1.03 ± 0.06	0.96 ± 0.06	3.99 ± 0.01
# 42	900	25	180	I	55.91 ± 0.42	0.25 ± 0.12	18.17 ± 0.25	27.97 ± 0.32	102.31 ± 0.37	1.98 ± 0.007	0.01 ± 0.005	0.96 ± 0.01	1.06 ± 0.01	4.01 ± 0.01
# 23	800	25	395	I	55.25 ± 1.46	0.83 ± 0.96	18.27 ± 0.43	27.77 ± 0.43	102.11 ± 0.78	1.96 ± 0.04	0.04 ± 0.04	0.97 ± 0.03	1.06 ± 0.01	4.02 ± 0.02
# 43	1100	20	153	II	55.38 ± 0.37	0.07 ± 0.003	18.71 ± 0.13	25.24 ± 0.14	99.38 ± 0.35	2.00 ± 0.005	0.027 ± 0.008	1.01 ± 0.009	0.98 ± 0.007	3.99 ± 0.01
# 19	800	20	119	II	55.20 ± 0.49	0.03 ± 0.02	19.14 ± 0.39	24.71 ± 0.39	99.07 ± 0.60	2.00 ± 0.007	0.01 ± 0.001	1.03 ± 0.02	0.96 ± 0.01	4.00 ± 0.01
# 55	900	30	293	II	56.19 ± 0.57	0.24 ± 0.06	19.50 ± 0.84	23.50 ± 1.50	99.43 ± 0.23	2.02 ± 0.05	0.01 ± 0.01	1.05 ± 0.16	0.91 ± 0.25	3.98 ± 0.05
# 56	900	30	397	I	55.51 ± 1.20	0.70 ± 0.85	18.20 ± 0.36	27.82 ± 0.34	102.23 ± 0.65	1.97 ± 0.12	0.03 ± 0.04	0.96 ± 0.10	1.06 ± 0.03	4.02 ± 0.06
# 57	900	30	308	I	55.04 ± 0.18	0.03 ± 0.01	18.69 ± 0.11	25.42 ± 0.17	99.17 ± 0.21	2.00 ± 0.01	0.002 ± 0.002	1.01 ± 0.02	0.99 ± 0.03	4.00 ± 0.01
# M5	900	100	121	II	55.62 ± 0.66	0.25 ± 0.08	19.27 ± 0.94	24.01 ± 1.27	99.15 ± 0.38	2.01 ± 0.01	0.01 ± 0.003	1.04 ± 0.05	0.93 ± 0.05	3.99 ± 0.01
# M7	900	80	170	II	55.19 ± 0.29	0.25 ± 0.02	19.09 ± 0.99	24.41 ± 0.94	99.93 ± 0.32	2.00 ± 0.006	0.01 ± 0.001	1.03 ± 0.05	0.95 ± 0.04	3.99 ± 0.01
# M9	900	60	242	II	56.19 ± 0.57	0.24 ± 0.06	19.50 ± 0.84	23.50 ± 1.51	99.43 ± 0.23	2.02 ± 0.01	0.01 ± 0.003	1.04 ± 0.04	0.91 ± 0.06	3.98 ± 0.01
# 77	900	30	402	II	55.86 ± 0.17	0.02 ± 0.01	19.69 ± 0.23	24.42 ± 0.35	99.99 ± 0.25	2.00 ± 0.003	0.009 ± 0.001	1.05 ± 0.01	0.94 ± 0.01	4.00 ± 0.01
# 78	900	20	259	II	56.71 ± 0.25	0.07 ± 0.13	19.41 ± 0.44	25.44 ± 0.62	101.64 ± 0.33	2.00 ± 0.004	0.003 ± 0.005	1.02 ± 0.02	0.97 ± 0.02	3.99 ± 0.01
# 84	1100	30	408	II	56.16 ± 0.20	0.009 ± 0.010	19.25 ± 0.23	25.04 ± 0.28	100.46 ± 0.29	2.01 ± 0.003	0.0004 ± 0.0005	1.03 ± 0.01	0.96 ± 0.01	3.99 ± 0.01
# 83	1000	30	568	II	56.16 ± 0.27	0.008 ± 0.010	19.19 ± 0.13	25.04 ± 0.14	100.40 ± 0.30	2.02 ± 0.004	0.0004 ± 0.0005	1.03 ± 0.008	0.96 ± 0.005	3.99 ± 0.001
# 81	700	30	248	II	56.09 ± 0.20	0.01 ± 0.01	20.17 ± 0.38	24.24 ± 0.44	100.50 ± 0.23	2.00 ± 0.003	0.001 ± 0.0004	1.07 ± 0.02	0.93 ± 0.02	4.00 ± 0.01

Appendix 2. *Microprobe analyses for Al-bearing diopside in wt.% for oxides and in a.p.f.u. for cations (see section 3.1.2)*

run	T (°C)	P (kbar)	H₂O(ppm)	SiO₂	Al₂O₃	MgO	CaO	Sum	Si	Al	Mg	Ca	Cation sum
# 28	1000	15	901	55.02 ± 0.27	2.38 ± 0.22	19.58 ± 0.35	22.86 ± 0.30	99.84 ± 0.45	1.97 ± 0.02	0.10 ± 0.04	1.04 ± 0.02	0.88 ± 0.04	3.98 ± 0.02
# 32	1000	15	1181	52.70 ± 0.21	5.42 ± 0.16	17.58 ± 0.11	25.18 ± 0.11	100.88 ± 0.25	1.88 ± 0.02	0.23 ± 0.03	0.94 ± 0.03	0.96 ± 0.03	4.01 ± 0.01
# 35	1000	15	1797	52.78 ± 0.28	5.94 ± 0.18	17.34 ± 0.10	25.16 ± 0.09	101.22 ± 0.64	1.88 ± 0.02	0.25 ± 0.03	0.92 ± 0.02	0.96 ± 0.01	4.00 ± 0.01
# 39	1000	15	2060	50.41 ± 1.23	7.52 ± 1.75	16.18 ± 0.64	25.68 ± 0.09	99.78 ± 0.93	1.83 ± 0.04	0.32 ± 0.07	0.87 ± 0.03	1.0 ± 0.01	4.01 ± 0.01
# 36	1000	15	2510	49.83 ± 0.44	9.98 ± 0.74	15.44 ± 0.32	25.31 ± 0.11	100.56 ± 0.40	1.79 ± 0.02	0.42 ± 0.03	0.83 ± 0.02	0.97 ± 0.01	4.00 ± 0.01
# 61	900	25	1722	54.72 ± 0.35	3.18 ± 0.37	18.50 ± 0.21	25.01 ± 0.11	101.41 ± 0.70	1.94 ± 0.06	0.13 ± 0.02	0.98 ± 0.05	0.95 ± 0.04	4.00 ± 0.03
# 63	900	25	1995	53.94 ± 0.50	4.20 ± 0.20	17.78 ± 0.33	25.21 ± 0.28	101.13 ± 0.72	1.92 ± 0.02	0.18 ± 0.03	0.94 ± 0.02	0.96 ± 0.01	4.00 ± 0.02
# 66	900	25	825	55.53 ± 0.18	1.58 ± 0.24	19.75 ± 0.15	23.22 ± 0.21	100.08 ± 0.20	1.98 ± 0.01	0.07 ± 0.01	1.05 ± 0.01	0.89 ± 0.01	3.99 ± 0.01
# 38	1100	25	573	55.54 ± 0.14	1.54 ± 0.10	19.74 ± 0.12	23.26 ± 0.15	100.07 ± 0.17	1.98 ± 0.01	0.07 ± 0.02	1.05 ± 0.02	0.89 ± 0.02	3.99 ± 0.03
# 40	1100	25	636	54.94 ± 0.23	2.77 ± 0.05	18.59 ± 0.16	25.10 ± 0.17	101.39 ± 0.60	1.95 ± 0.02	0.12 ± 0.01	0.98 ± 0.04	0.95 ± 0.02	4.00 ± 0.02
# 44	1100	25	869	54.89 ± 0.19	2.97 ± 0.07	18.60 ± 0.13	24.99 ± 0.01	101.45 ± 0.20	1.94 ± 0.01	0.12 ± 0.01	0.98 ± 0.02	0.95 ± 0.02	3.99 ± 0.01
# 47	1100	25	1054	51.74 ± 0.59	5.89 ± 0.49	17.27 ± 0.50	25.35 ± 0.52	100.24 ± 0.82	1.86 ± 0.02	0.25 ± 0.04	0.93 ± 0.03	0.98 ± 0.02	4.01 ± 0.03
# 49	1100	25	2591	50.10 ± 1.88	8.37 ± 2.12	16.28 ± 0.70	25.62 ± 0.20	100.37 ± 1.23	1.80 ± 0.06	0.36 ± 0.07	0.87 ± 0.03	0.99 ± 0.01	4.02 ± 0.05

Appendix 3. F_E-f_E plots based on the Birch-Murnaghan EoS for individual crystal axes a, b and c of the four diopside single crystals of the present study (see section 3.2). Equations for the weighted fits are presented in each plot.

a - cpx_1

$F_E = 105(1) + 872(52) \, f_E$

a - cpx_2

$F_E = 108(1) + 807(67) \, f_E$

a - cpx_3

$F_E = 110(1) + 786(75) \, f_E$

a - cpx_4

$F_E = 104(1) + 776(81) \, f_E$

b - cpx_1

$F_E = 88(1) + 66(30) \, f_E$

b - cpx_2

$F_E = 89(1) + 69(44) \, f_E$

b - cpx_3

$F_E = 96(1) + 6(61) \, f_E$

b - cpx_4

FE = 86(1) + 50(34) f_E

c - cpx_1

$F_E = 106(1) + 589(59) \, f_E$

c - cpx_2

$F_E = 108(1) + 554(58) \, f_E$

c - cpx_3

$F_E = 111(1) + 469(78) \, f_E$

c - cpx_4

$F_E = 103(1) + 496(76) \, f_E$

Normalised pressure F_E

Eulerian strain f_E

Eulerian strain f
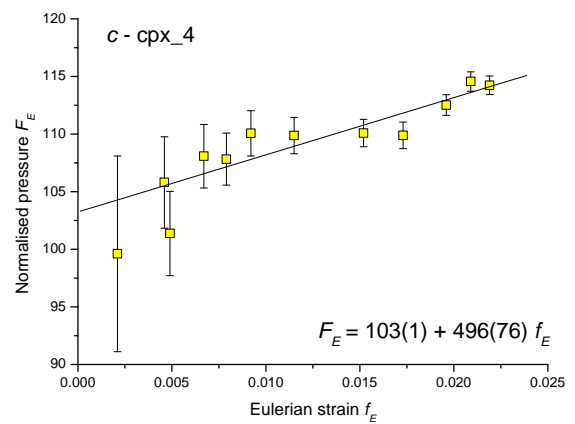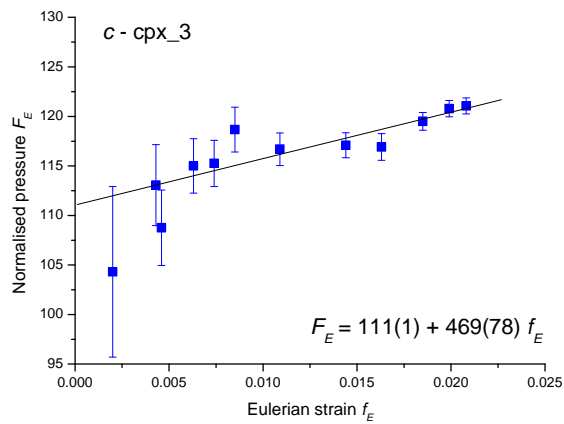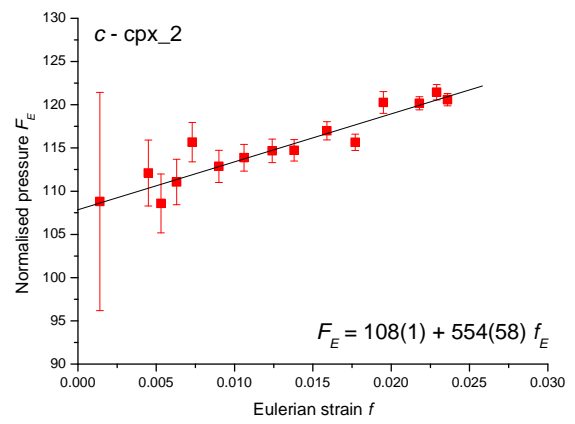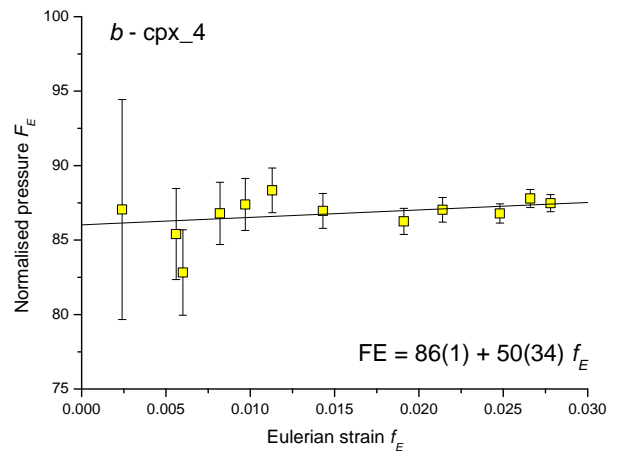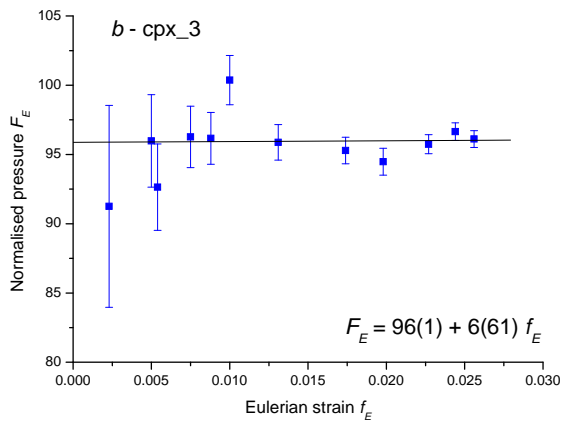
Appendix 4. *Fractional atomic coordinates and anisotropic displacement parameters from the structural refinement of the four diopside crystals (see section 3.3).*

		Cpx_1	Cpx_2	Cpx_3	Cpx_4
Ca (*M2*)	x	0.0	0.0	0.0	0.0
	y	0.30118 (3)	0.30157(3)	0.30287(4)	0.30065(5)
	z	0.25	0.25	0.25	0.25
	occupancy	0.9766	1.0	1.0	0.9553
	U_{eq}	0.00895(7)	0.00883(6)	0.01003(8)	0.0092(1)
Mg (*M2'*)	x	0.0			0.0
	y	0.24010(0)			0.23380(0)
	z	0.25			0.25
	occupancy	0.0234			0.0447
	U_{iso}	0.003(3)			0.006(3)
Mg (*M1*)	x	0.0	0.0	0.0	0.0
	y	0.90799(5)	0.90828(5)	0.90886(6)	0.90769(8)
	z	0.25	0.25	0.25	0.25
	U_{eq}	0.00636(9)	0.00648(9)	0.0065(2)	0.0063(1)
Si (*T*)	x	0.28651(3)	0.28618(3)	0.28648(3)	0.28693(4)
	y	0.09330(3)	0.09337(3)	0.09351(4)	0.09325(4)
	z	0.23015(5)	0.22908(5)	0.22624(6)	0.23109(7)
	U_{eq}	0.00529(7)	0.00533(6)	0.00619(9)	0.00528(9)
O1	x	0.11591(7)	0.11571(7)	0.11409(9)	0.1162(1)
	y	0.08761(7)	0.08732(7)	0.0869(1)	0.0878(1)
	z	0.1425(1)	0.1422(1)	0.1386(2)	0.1430(2)
	U_{eq}	0.0067(1)	0.0068(1)	0.0092(2)	0.0066(2)
O2	x	0.36159(7)	0.36139(7)	0.3613(1)	0.3620(1)
	y	0.24964(7)	0.24992(7)	0.2527(1)	0.2497(1)
	z	0.3199(1)	0.3190(1)	0.3182(2)	0.3213(2)
	U_{eq}	0.0090(1)	0.0085(1)	0.0108(2)	0.0096(2)
O3	x	0.35072(7)	0.35077(7)	0.35162(9)	0.3509(1)
	y	0.01814(8)	0.01772(8)	0.0183(1)	0.0186(1)
	z	-0.0045(1)	-0.0052(1)	-0.00767(2)	-0.0037(2)
	U_{eq}	0.0079(1)	0.0077(1)	0.0096(2)	0.0079(2)

Erklärung

Hiermit erkläre ich, dass ich die vorliegende Arbeit selbständig verfasst und keine anderen als die von mir angegebenen Quellen und Hilfsmittel benutzt habe.

Ferner erkläre ich, dass ich nicht anderweitig versucht habe, mit oder ohne Erfolg, eine Dissertation einzureichen und auch keine gleichartige Doktorprüfung an einer anderen Hochschule endgültig nicht bestanden habe.

Bayreuth, im Juni 2008

Polina Gavrilenko